

LT REPORT TR-88-1

# WIDELY TUNABLE GAS LASER FOR REMOTE SENSING

D. E. Rothe

December 1988

FINAL TECHNICAL REPORT - PHASE II

NASA SBIR CONTRACT NO. NAS7-970

Performance Period: 1 August 1986 to 31 October 1988

Sponsored by:

National Aeronautics and Space Administration  
Washington, DC

Monitored by:

NASA Resident Office - JPL  
4800 Oak Grove Drive  
Pasadena, CA 9111095500 Wilshire Avenue, NE  
Albuquerque, NM 87113

NASA-CR-190067

Unclass

02/45 0121101

NASA-CR-190067 WIDELY TUNABLE  
GAS LASER FOR REMOTE SENSING  
Final Technical Report, 1 Aug. 1986 - 31  
Oct. 1988 (Lasertechnics) 99 0

**"SBIR RIGHTS NOTICE (APR 1985)"**

This SBIR data is furnished with SBIR rights under NASA Contract No. NAS7-970. For a period of two years after acceptance of all items to be delivered under this contract the Government agrees to use this data for Government purposes only, and it shall not be disclosed outside the Government during such period without permission of the Contractor, except that, subject to the foregoing use and disclosure prohibitions, such data may be disclosed for use by support contractors. After the aforesaid two-year period the Government has a royalty-free license to use, and to authorize others use on its behalf, this data for Government purposes, but is relieved of all disclosure prohibitions and assumes no liability for unauthorized use of this data by third parties. This Notice shall be affixed to any reproductions of this data, in whole or in part.

The views and conclusions contained in this document are those of the author and should not be interpreted as necessarily representing the official policies, either expressed or implied, of the National Aeronautics and Space Administration or of the U.S. Government.

REPORT DOCUMENTATION PAGE		READ INSTRUCTIONS BEFORE COMPLETING FORM	
1. REPORT NUMBER Lasertechnics TR-88-1		2. GOVT ACCESSION NO.	
4. TITLE (and Subtitle) WIDELY TUNABLE GAS LASER FOR REMOTE SENSING OF STRATOSPHERIC CONSTITUENTS		3. RECIPIENT'S CATALOG NUMBER	
7. AUTHOR(S) D. E. Rothe		5. TYPE OF REPORT & PERIOD COVERED FINAL REPORT -PHASE II 1 AUG 1986 - 31 OCT 1988	
9. PERFORMING ORGANIZATION NAME AND ADDRESS LASERTECHNICS, INC. 5500 Wilshire Avenue, NE Albuquerque, NM 87113		6. PERFORMING ORG. REPORT NUMBER TR-88-1	
11. CONTROLLING OFFICE NAME AND ADDRESS NASA Resident Office - JPL 4800 Oak Grove Drive Pasadena, CA 91109		8. CONTRACT OR GRANT NUMBER(S) SBIR CONTRACT - NASA NAS7-970	
14. MONITORING AGENCY NAME & ADDRESS (if diff. from Controlling Office)		10. PROGRAM ELEMENT, PROJECT, TASK AREA & WORK UNIT NUMBERS	
		12. REPORT DATE December 1988	
		13. NO. OF PAGES 95	
		15. SECURITY CLASS. (of this report) UNCLASSIFIED	
		15a. DECLASSIFICATION/DOWNGRADING SCHEDULE	
16. DISTRIBUTION STATEMENT (of this report) Distribution limited to U.S. Government Agencies for Test and Evaluation only.  See: "SBIR RIGHTS NOTICE"			
17. DISTRIBUTION STATEMENT (of the abstract entered in Block 20, if different from report) Abstract and SUMMARY approved for public release; Distribution unlimited			
18. SUPPLEMENTARY NOTES			
19. KEY WORDS (Continue on reverse side if necessary and identify by block number) Electric Discharge Laser      Prepulse Technique Rare-Gas Halide Laser      Magnetic Switching Pulse Power Technology      High Efficiency Pulse Forming Line      X-Ray Preionization Remote Sensing			
20. ABSTRACT (Continue on reverse side if necessary and identify by block number) An advanced, highly efficient and reliable Rare-Gas Halide laser has been developed. It employs: (1) novel prepulse techniques and impe- dance matching for efficient energy transfer, (2) magnetic switches for high reliability, (3) X-ray preionization for discharge uniformity and beam quality, (4) an integrated gas flow loop for compactness. When operated as a XeCl laser, the unit produces 2 J per pulse with good beam uniformity. Optical pulse duration is 100 ns. Pulse repe- tition rate has been tested up to 25 Hz. Efficiency is 3 per cent.			

## 1.0 SUMMARY

This Report describes the development of an efficient and reliable multi-joule high-pressure gas laser based on new state-of-the-art excimer laser technology. Such a laser has potential applications in a space-based LIDAR system for remote sensing of the atmosphere, as a transmitter for submarine communications, and for a multitude of commercial uses.

The design of the laser incorporates a specially constructed low-impedance pulse-forming network (PFN), including several magnetic switches which permit a high-voltage prepulse to be applied to the discharge electrodes. This prepulse technique makes it possible to impedance-match the PFN to the discharge plasma for maximum energy transfer efficiency. Extremely uniform preionization of the gas mixture is achieved with 70 kV X-rays produced with a newly developed long-life X-ray generator.

When operated as an XeCl laser this device has demonstrated optical output at 2 J per pulse at 308 nm, and pulse repetition rates as high as 25 Hz. Because of its high discharge stability, long optical pulse durations of 100 ns were easily attained. Electrical single-pulse laser efficiency of 3% has been achieved. Good beam uniformity and excellent pulse energy stability have been demonstrated.

Significant new knowledge and expertise has been gained during this investigation in the construction and operation of a long-life corona plasma e-beam cathode, in the construction and control of saturable magnetic Metglas switches, and in the design of prepulse circuits which form an integral part of the discharge PFN. This work has demonstrated that the high magnetic saturation flux density of thin Metglas ribbon can be utilized to produce high-performance switches with long hold-off periods and fast turn-on action. Rates of rise of  $10^{12}$  V/s have been achieved with the present magnetic prepulse switch, eliminating the need for spark gaps. The three-electrode structure of the present laser has not been found advantageous, because the dynamic interplay between the two discharges proved difficult to understand. A new design with two solid discharge electrodes is proposed herein.

New technology developed here will be used in a commercial follow-on excimer laser, which has potential applications in semiconductor processing (annealing, planarization of metal films, selective etching of films, selective film deposition), photochemical processes, product marking (including semiconductors and metals), and micromachining. A smaller unit with less pulse energy but higher pulse frequency has potential applications in the medical field (corneal machining, laser angioplasty) and for UV lithography.

## TABLE OF CONTENTS

	<u>Page</u>
	i
	ii
1.0 SBIR Rights Notice	1
Documentation Page and Abstract	2
SUMMARY	3
Table of Contents	6
List of Figures and Tables	6
2.0 INTRODUCTION	9
2.1 Key Technical Issues	11
2.2 Project Objectives and Relevance to NASA Goals	12
2.3 Unique Features of the Discharge-Excited Multigas Laser	12
3.0 APPROACH FOR INCREASING LASER EFFICIENCY AND RELIABILITY	13
3.1 Efficiency Optimization	14
3.2 Minimum Stress Design (Reliability and Lifetime)	15
3.3 Compactness	15
4.0 EXCIMER LASER CONSTRUCTION	15
4.1 Functional System Outline	19
4.2 Discharge Parameters	20
4.3 Discharge Electrodes and Feedthroughs	24
4.4 Pulse-Forming Network	26
4.5 Pulse Charging Unit	26
4.6 X-Ray Preionizer and Pulser	36
4.7 Trigger and Delay Circuits	36
4.8 Gas Flow and Cooling	40
4.9 Optical Cavity	43
5.0 PRELIMINARY EXPERIMENTS	43
5.1 Electric Field Plotting	44
5.2 Computer Simulation of Pulse-Forming Networks	57
5.3 Testing of Sample Metglas Cores	63
6.0 DEVELOPMENT OF INTEGRATED PREPULSE GENERATING SCHEMES	63
6.1 Prepulse Circuits	75
6.2 Magnetic Switch Design	79
6.3 Core Reset Techniques	84
7.0 TEST RESULTS	90
8.0 CONCLUSIONS	90
9.0 PROPOSED FUTURE WORK	90
9.1 Proposed Changes	93
9.2 Commercial Spin-offs and Applications	94
10.0 REFERENCES	94

## LIST OF FIGURES AND TABLES

	Page
Figure 2-1. Ideal Pump Pulse.	8
Figure 2-2. Avalanche Formation Time as a Function of Overvoltage Ratio.	8
Figure 4-1. Functional Outline of System Components.	16
Figure 4-2. Cross-Section through Discharge Chamber and PFN Connections.	17
Figure 4-3. Overall View of Excimer Laser System.	18
Figure 4-4. Underside of Support Plate Showing Kynar Insulated Cathode Feedthroughs.	21
Figure 4-5. Cathode Installed on Partition Plate.	22
Figure 4-6. Cathode Fin.	22
Figure 4-7. Secondary Cathode Installed over Primary Cathode.	23
Figure 4-8. Pulse Forming Line with Magnetic Switches Installed.	25
Figure 4-9. Schematic of Pulse Charging Unit.	27
Figure 4-10. Top View of Pulse Charging Unit Showing Location of Components.	28
Figure 4-11. Schematic of X-Ray Generator and Pulser.	31
Figure 4-12. E-Gun Cathode Design.	33
Figure 4-13. E-Gun Anode Design.	34
Figure 4-14. X-Ray Generator Pulse Characteristics.	35
Figure 4-15. Blower Installed in Discharge Chamber.	38
Figure 4-16. Magnetic Coupling Design.	39
Figure 4-17. Heat Exchanger Design.	41
Figure 4-18. Vacuum Pump and Gas Mixing Station.	42
Figure 5-1. Electric Field Plot in Discharge Section for Original Geometry.	45
Figure 5-2. Electric Field Plot in Discharge Section with Modified Kynar Insulator.	45
Figure 5-3. Model of PFN. Original Version with Magnetically Switched Positive Pulse.	46
Figure 5-4. Charging Current through Thyatron (Computer Modeling).	48
Figure 5-5. Voltage at Screen during Charging Pulse (Computer Modeling).	49
Figure 5-6. Prepulse and Discharge Voltage at Screen (Computer Modeling).	50
Figure 5-7. Prepulse and Discharge Voltage at Cathode (Computer Modeling).	50

	Page
Figure 5-8. Power Dissipated in Main Discharge (Computer Modeling).	52
Figure 5-9. Computer Model of X-Ray Pulser.	54
Figure 5-10. Calculated E-Beam Anode Voltage Pulses for Two Different Diode Impedances.	56
Figure 5-11. B-H Curve for Racetrack Core Wound from 15 $\mu$ m Thick by 5 cm Wide 2605-CO Metglas Ribbon.	59
Figure 5-12. B-H Curve for Racetrack Core Wound from 25 $\mu$ m Thick by 5 cm Wide 2705-MN Metglas Ribbon.	59
Figure 5-13. Experimental Setup for Testing Metglas Cores.	60
Figure 5-14. Voltage and Current for 2705-MN Core.	61
Figure 5-15. Magnified Current Pulse for 2705-MN Core.	61
Figure 5-16. Voltage Pulse for 2605-CO Core.	61
Figure 5-17. Magnified Current Pulse for 2605-CO Core.	61
Figure 6-1. Original Prepulse Circuit; Magnetically Switched Positive Pulse Followed by PredischARGE Switched Negative Pulse.	65
Figure 6-2. Calculated Voltage Across Main Gap for $L_K = 5$ nH Distributed over PredischARGE Circuit.	66
Figure 6-3. Calculated Voltage Across Main Gap for Lumped 20 nH Cathode Impedance.	66
Figure 6-4. Measured Screen Voltage Showing Prepulse Generated by Circuit in Figure 6-1.	67
Figure 6-5. Expanded Trace of Prepulse at 50 ns/DIV Showing Prepulse to be 25 ns Wide.	67
Figure 6-6. Modified Prepulse Circuit; Magnetically Switched Negative Pulse.	68
Figure 6-7. Screen Voltage for Circuit in Figure 6-6 (Glow in Main Gap).	70
Figure 6-8. Screen Pulse at Higher Charging Voltage (Arc in Main Gap).	70
Figure 6-9. Voltage-Doubling Prepulse Circuit with Voltage Divider and Fast Switch ( $L_2$ ).	72
Figure 6-10. Calculated Cathode and Screen Voltages for $L_{2SAT} = 50$ nH.	72
Figure 6-11. Cathode and Screen Voltages for Spark-Gap Switched Prepulse.	73
Figure 6-12. Cathode and Screen Voltages for Magnetically Switched Prepulse.	73
Figure 6-13. Laser Burn Marks for Two Different Mirror Alignments (1 J Output).	74
Figure 6-14. Side-to-Side Intensity Profile of Laser Beam.	74
Figure 6-15. One of the 7-Turn Magnetic Switches Originally Used for $L_2S$ .	76
Figure 6-16. Fast Magnetic Prepulser.	77
Figure 6-17. Measured B-H Curve for New Low-Inductance Metglas Switch.	78

	Page
Figure 6-18. Prepulse Time Jitter with Insufficient Reset.	80
Figure 6-19. Magnetic Core Reset Circuit Using Auxiliary Windings on Saturable Inductors.	82
Figure 6-20. Magnetic Core Reset Circuit. Pulse Applied Directly to Laser PFN.	83
Figure 7-1. Cathode and Screen Pulse (200ns/DIV).	85
Figure 7-2. Cathode and Screen Pulse (100ns/DIV).	85
Figure 7-3. Screen Voltage and Optical Pulse (New Gas Mix).	87
Figure 7-4. Screen Voltage and Optical Pulse (Old Gas Mix).	87
Figure 7-5. Beam Imprints at 2 J Output Level for Different Resonators and Alignments.	88
Figure 7-6. Pulse Energy Stability at 1 Hz Measured with Pyroelectric Energy Meter.	89
Figure 9-1. Proposed Two-Electrode PFN and Prepulse Circuit.	92
Table 2-1. Atmospheric Species Measurable with Multigas Pulsed Laser System.	10
Table 5-1. Computer Model Parts List for Laser Discharge PFN.	47
Table 5-2. Parts List for X-Ray Pulser Model.	55



## 2.0 INTRODUCTION

In the past, pulsed gas lasers have not been seriously considered for space-based applications when other alternatives were available. The reasons for this have been two-fold: the need for switching relatively high voltages and the need for special gas handling equipment.

The work reported here addresses primarily the first issue. This publication describes the development of fast magnetic switches to replace the less reliable plasma switches, such as spark gaps. It also describes progress made in developing impedance-matched PFNs, resulting in higher laser efficiencies and in arc-free discharges. An additional benefit is derived from the latter, namely increased component life. The above advances greatly mitigate the problems traditionally encountered with handling high voltages.

The second issue, involving gas handling equipment, has to be addressed for each gas laser separately. It generally involves the use of a gas cleanup system, which continually or intermittently scrubs the gas free of contaminants and reaction products to maintain an optimally clean and correct gas mixture. In addition, provisions may have to be made to completely replace the gas after so many pulses (typically between  $10^8$  and  $10^9$  shots). With some lasers, such as HF/DF lasers, disposal of the reaction products may also present a problem. At this time it appears entirely feasible that closed-cycle rare-gas halide (RGH) and  $\text{CO}_2$  lasers, with suitable gas processing cycles, can be developed which are entirely service-free for periods of one year. Suitable gas processors (catalytic converters, getter type traps and cryogenic traps) are being developed elsewhere<sup>1-5</sup>. Because of the finite resources for the present program, the gas cleanup issue has been considered beyond the scope of this project.

### 2.1 KEY TECHNICAL ISSUES

The principal issues associated with the development of long-life RGH lasers (and  $\text{CO}_2$  lasers) are the long-term production of stable, uniform, relatively long-duration, high-power-density electric discharges in the laser gas, the long-term maintenance of laser gas composition and purity, and the avoidance of materials degradation. Additionally, high flow quality must be maintained at the laser head. For the optics and wavelength control system, stable, automated operation at the required laser frequency, and within the required frequency bandwidth, are also challenging issues.

Traditionally, the central problems affecting the performance of all high-pressure, self-sustained discharge-excited gas lasers are discharge uniformity and stability. The need for uniform-field electrodes, uniform preionization, and rapidly rising voltage and current pulses was recognized quite early in the development of these so-called TE-lasers<sup>6</sup>. Consequently, most TE-lasers have carefully profiled electrodes, some means of preionization (usually hard UV), and low-inductance pulsers for rapidly feeding power into the discharge.

Homogeneous discharges can be achieved in high-pressure RGH lasers, if certain criteria are met simultaneously. These are:

1. Uniform electric field between discharge electrodes prior and during discharge formation. Field variations should be less than 1 per cent.
2. Uniform volume preionization. In a plane perpendicular to the discharge current, the ionization level should not vary more than 10 per cent. In the direction of current flow, the ionization level should be within a factor of two.
3. Preionization density must be above a certain minimum value everywhere in the discharge volume. This minimum electron number density is typically around  $10^6 \text{ cm}^{-3}$ , but depends on the gas mixture, gas pressure and voltage rise<sup>7</sup>.
4. Voltage and current must rise sufficiently fast to drive the electron avalanche development in a uniform manner.
5. The PFN, rather than the discharge, should limit the current to inhibit ionization runaway.

With the strongly electronegative gas mixtures used in RGH lasers, stable discharges can generally be maintained only for a few hundred nanoseconds. In XeCl lasers, local depletion of vibrationally excited HCl causes the discharge to become filamentary at the end of a long pump pulse, causing premature termination of the optical pulse<sup>8,9</sup>. Vibrationally excited HCl has a large dissociative electron attachment cross-section, and normally acts as a stabilizing agent against ionization runaway.

Recent advances in excimer laser technology<sup>10,11,12</sup> have been incorporated into the present laser to improve the laser efficiency and beam uniformity. Some of these advances are:

1. X-rays are used to provide uniform preionization in the high-pressure gas.
2. A prepulse is used to initiate the discharge. This permits adding the bulk of the electric energy under impedance-matched conditions.
3. A constant-voltage, constant-current transmission line drive ensures stability and high-power excitation throughout the pump pulse.

An attachment dominated avalanche discharge acts approximately as a constant-voltage load<sup>13,14</sup>. Thus the discharge impedance decreases inversely proportional to an increase in current. It is necessary, therefore, to limit the current externally, so as not to drive the discharge into ionization and/or thermal instability for long-pulse excitation. A distributed-impedance pulse-forming line (PFL) is ideally suited for accomplishing this.

An ideal pump pulse for exciting the laser medium is shown in Figure 2-1. For the gas to break down in less than 20 ns, the initial overvoltage peak  $V_{pk}$  must be at least 4 times the steady-state discharge voltage  $V_D$ .<sup>10,14</sup> This is inconsistent with an impedance-matched transmission line, which produces an overvoltage ratio ( $V_{pk}/V_D$ ) of only two. For optimum energy efficiency, it is necessary therefore, to apply an additional high-voltage prepulse. A strong pulse of ionizing radiation, overlapping with the rising and falling parts of the prepulse, assures that the avalanche discharge develops into a uniform glow.

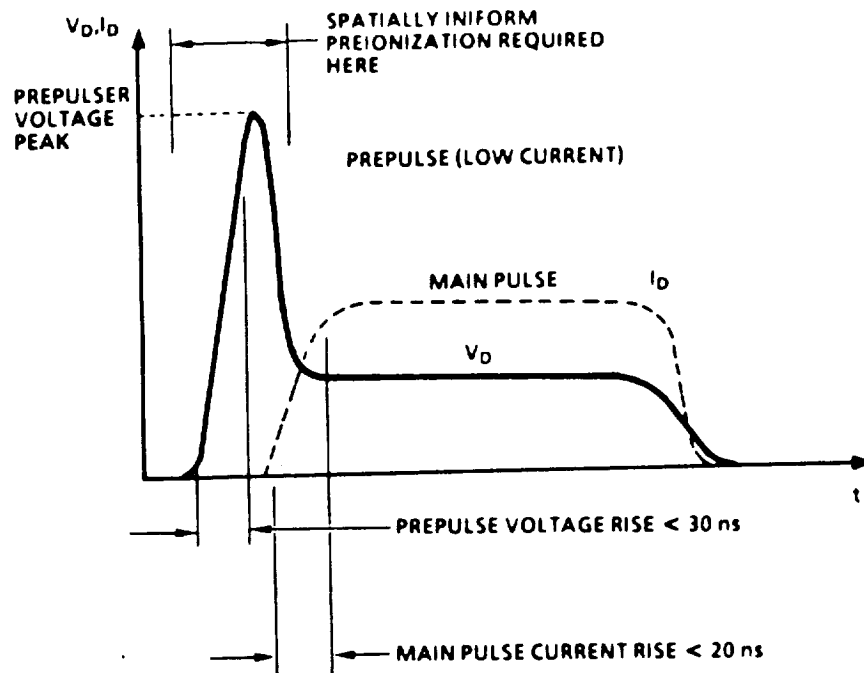


FIGURE 2-1. IDEAL PUMP PULSE

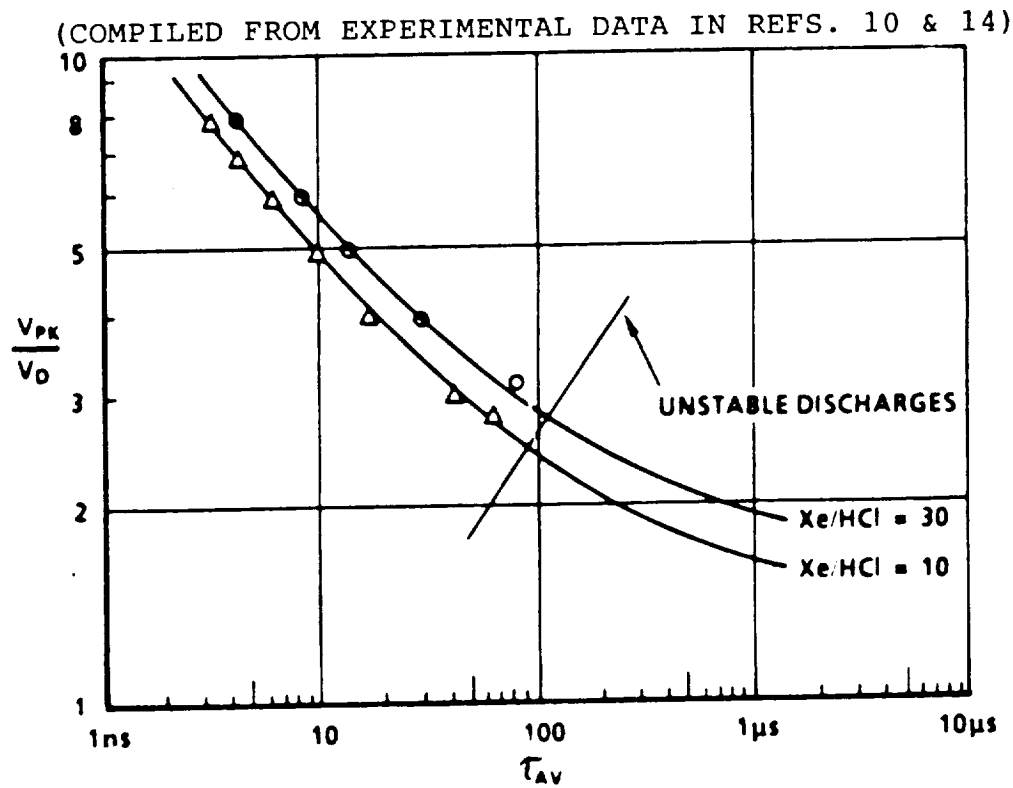


FIGURE 2-2. AVALANCHE FORMATION TIME AS A FUNCTION OF OVERVOLTAGE RATIO

For a PFL with output impedance  $Z_0$  to provide a constant-V, constant-I pump pulse, the laser head inductance  $L_{HD}$  must be low enough to make the current risetime,  $L_{HD}/Z_0$ , less than 25% of the pump pulse duration; otherwise the inductance effects dominate over the PFL characteristics, in which case the PFL might as well be replaced by a single capacitor. When this is done, however, both discharge stability (limited pulse length) and the laser efficiency will be compromised.

During the early development phases of high-energy discharge-excited RGH lasers<sup>7</sup>, it was believed necessary for good discharge stability that the voltage appearing on the electrodes must rise from zero to  $4V_D$  in 10 ns or less. More recent experiments have shown, however, that the electrode voltage can rise more slowly up to a value of  $2V_D$ , and that reasonably stable discharges can then be initiated with a fast-rising high-voltage prepulse<sup>10,11,12</sup> or with a strong pulse of ionizing radiation<sup>15</sup>. This has made it possible to eliminate the previously required fast rail gap switches in favor of combinations of thyratrons or thyristors<sup>16</sup> and magnetic switches. The present laser system is switched by a thyatron, operated in the so-called long-life radar mode, and saturable magnetic inductors are employed to generate the high-voltage prepulse.

Whereas it is permissible to have voltage appearing on the electrodes prior to the breakdown pulse, the duration and amplitude of such electric prestress must be well to the left of the curve in Figure 2-2; i.e. significantly shorter than the avalanche formation time at low overvoltages. Otherwise discharge instabilities will prevent formation of a uniform glow and will result in immediate arc formation. With smoothly contoured electrodes, corona induced streamer formation may be delayed for several microseconds at an electrode voltage between  $1.5 V_D$  and  $2 V_D$ . If the full charging voltage appears on the electrodes, the PFN should preferably be charged in less than one microsecond, however. Alternatively, a PFN should be employed which limits the electrode voltage prior to discharge initiation to less than  $1.5 V_D$ .

## 2.2 PROJECT OBJECTIVES AND RELEVANCE TO NASA GOALS

The objective of this work is the development of an advanced multi-joule TE-laser source for possible application in an orbiting LIDAR system and for industrial applications.

The design of the laser is based on the latest advances in excimer laser technology for optimizing the laser efficiency (3% in the UV) and for high reliability. The device incorporates X-ray preionization, prepulse techniques, impedance-matched pulse forming lines, magnetic switching and careful material selection. Special techniques are introduced for producing stable and uniform discharges.

TABLE 2-1

## ATMOSPHERIC SPECIES MEASURABLE WITH MULTIGAS PULSED LASER SYSTEM

RGH Version		DF Version		CO <sub>2</sub> Version	
Specie	Method	Specie	Method	Specie	Method
O <sub>3</sub>	DIAL	HCl	DIAL	O <sub>3</sub>	DIAL
SO <sub>2</sub>	DIAL	CH <sub>4</sub>	DIAL	SO <sub>2</sub>	DIAL
NO <sub>2</sub>	DIAL	N <sub>2</sub> O	DIAL	NH <sub>3</sub>	DIAL
ClO	DIAL	SO <sub>2</sub>	DIAL	N <sub>2</sub> H <sub>4</sub>	DIAL
OH	LIF	H <sub>2</sub> O	DIAL	C <sub>2</sub> H <sub>4</sub>	DIAL
NO	LIF	CO <sub>2</sub>	DIAL	HNO <sub>3</sub>	DIAL
Aerosols	MIE Scat	Aerosols	MIE Scat	CCl <sub>4</sub>	DIAL
Winds	Incoherent			CH <sub>3</sub> Cl	DIAL
	UV Doppler			COCl <sub>2</sub>	DIAL
				CFCl <sub>2</sub>	DIAL
				CF <sub>2</sub> Cl <sub>2</sub>	DIAL
				Aerosols	MIE Scat

In addition to having improved tunability, frequency stability and efficiency, the optical output pulse is expected to have the following unique characteristics:

1. Excellent beam uniformity and mode stability.
2. Optical pulse length greater than 100ns with multi-joule pulse energy in the excimer bands.

Pulse repetition rate will be 25 Hz. Component and system life is predicted to be in excess of 10<sup>9</sup> pulses.

NASA's interest in this project is primarily concerned with the potential use of this type of laser for remote sensing applications. The monitoring of atmospheric processes, as well as measuring the concentrations of chemical species and pollutants, is an important part of a well defined multi-disciplinary information gathering network for improving our understanding of the earth as a system. This global scientific program, planned by NASA for the 1990s, is known as the Earth Observing System (EOS), and includes a variety of remote sensing techniques from orbiting platforms<sup>17</sup>. Suitable, highly efficient laser sources for space-based LIDAR systems have to be developed now with established technology, in order to meet this time schedule.

Physical and chemical processes in the stratosphere are very complex and include radiative, chemical and dynamic interactions. Photochemistry in the stratosphere begins with the transport of "source molecules", such as  $\text{N}_2\text{O}$ ,  $\text{H}_2\text{O}$ ,  $\text{CH}_4$ ,  $\text{CFCl}_3$  and  $\text{CF}_2\text{Cl}_2$  from the troposphere. There they are transformed by photolysis and chemical reactions into highly reactive radicals, such as  $\text{ClO}$ ,  $\text{NO}$ ,  $\text{NO}_2$  and  $\text{OH}$ . Ozone,  $\text{O}_3$ , plays a special role in atmospheric chemistry. Because it absorbs a high percentage of the solar UV, which is harmful to biological organisms, it acts as a protecting layer and also as a major source of upper atmospheric heating. Species that are lost from the stratosphere by transport into the troposphere, such as  $\text{HCl}$ ,  $\text{SO}_2$  and  $\text{HNO}_3$ , may precipitate out as acid rain.

It is interesting to notice by comparison with Table 2-1 that essentially all these species can be measured by DIAL or LIF measurements with one or the other configuration of the type of laser developed here. For some species, such as  $\text{O}_3$  and  $\text{SO}_2$ , complementary determinations can be made in the UV and the IR for greater accuracy.

Aerosols such as  $\text{H}_2\text{SO}_4$  droplets (volcanic) and dust (volcanic and meteoritic) may be monitored at several wavelengths. Complementary Mie and Rayleigh scattering data may support each other. It is also possible to employ an  $\text{XeF}$  (350 nm) laser to measure wind fields in the lower stratosphere by incoherent Doppler detection<sup>18</sup>. A UV Doppler LIDAR may be able to monitor winds in atmospheric regions where an IR Doppler system does not encounter sufficient return signal from aerosol scattering<sup>19</sup>. Scattering coefficients in the near-UV are orders of magnitude higher than in the IR.

With a somewhat more sophisticated LIDAR setup, the line shapes of absorbing or fluorescing species may be analyzed to extract temperature and pressure data.

### 2.3 UNIQUE FEATURES OF THE DISCHARGE-EXCITED MULTIGAS LASER

The new excimer laser developed here can operate on all the RGH bands ( $\text{XeCl}$ ,  $\text{XeF}$ ,  $\text{KrF}$ ,  $\text{ArF}$ ) and has several unique features not generally found in commercially available lasers. The laser has been designed for high efficiency, long life, high reliability, long optical pulse and good beam uniformity.

Optical output specifications are 1 to 2 joules per pulse at pulse repetition frequencies up to 50 Hz. Optical pulse duration is 100 ns. Beam divergence is close to diffraction limited ( $2 \lambda/D$ ) with unstable resonator optics. System weight can be kept below 500 kg.

Some of the unique design features are:

1. X-ray preionization for more uniform discharge and less gas contamination.
2. Compact preionizer design with long-life corona plasma cathode.
3. Magnetically switched prepulse to permit impedance matching and high electrical laser efficiency (3%).

4. Constant-current, constant-voltage, voltage-matched, long-pulse PFL to energize the gain medium.
5. Extensive use of magnetic switches (saturable core reactors) to replace the less reliable plasma switches.
6. Magnetic assist and inverse current blocking to extend the life of the charging thyatron.
7. Compact gas flow system which minimizes gas required to refill the laser.
8. Careful selection of discharge chamber materials for long gas life.

### 3.0 APPROACH FOR INCREASING LASER EFFICIENCY AND RELIABILITY

Specific lines of approach taken to produce a laser which is efficient, reliable and compact are discussed in more detail in this section.

#### 3.1 EFFICIENCY OPTIMIZATION

The author has shown<sup>10,14</sup> in 1981 that efficient energy transfer to the electric discharge is not possible with a single-pulse excitation network. Because of the constant-voltage load characteristics of the discharge, impedance matching is essentially achieved by voltage matching; i.e. the open-circuit output voltage from the pulser has to be twice the steady-state discharge voltage,  $V_D$ . Unfortunately, at such an overvoltage ratio of two, it takes microseconds for the discharge to develop, ample time for instabilities to grow to a dominating magnitude. Avalanche formation times as a function of overvoltage ratio have been plotted in Figure 2-2.

The traditional solution has been to charge the PFN to a higher voltage, so as to obtain an overvoltage ratio of 3 or 4, which reduces the discharge formation time to less than 100 ns. Under these mismatched conditions, however, the power transfer is less than 50% efficient. This is the reason for the relatively low overall efficiency (approximately 1%) of most XeCl and KrF lasers.

Operating a laser under mismatched conditions has a further disadvantage. The energy, which is not dissipated in the discharge during the pump pulse, will ring back (unless "crowbarred" into a resistive 1 ohm load) and produce "post-discharge arcing" in the laser. Needless to say, the life of the electrodes, the capacitors and the thyatron switch, as well as the gas purity, will all be compromised by such arcing.

By applying a high-voltage prepulse (of approximately 4  $V_D$  amplitude) to the electrodes to establish the avalanche discharge in less than 20 ns, it is possible to feed in the bulk of the excitation energy under matched conditions from a PFL charged to  $2V_D$ . Well executed prepulse schemes,<sup>10,11</sup> applied to an XeCl laser, have demonstrated that 4% efficiency can be reached.

In order to pulse one of the discharge electrodes to 4  $V_D$ , the electrode must be temporarily isolated from the low-impedance PFN by an isolation switch. In early prepulse work,<sup>9,10,20</sup> the prepulser was a separate pulse generator which

needed additional timing and trigger pulses. In the work reported here, the prepulser has been integrated into the discharge PFN and needs no separate timing. Electrode isolation has been effected in the past by multichannel spark gaps<sup>10</sup>, glow discharges<sup>12</sup>, saturable pulse transformers<sup>9</sup>, and saturable magnetic inductors<sup>20</sup>. Whereas a magnetic switch is the ideal isolation device, it was not clear at the onset of this work that a high-frequency, fast magnetic switch with a high  $V \cdot t$  product and a very low saturated inductance could be constructed to suit this demanding application. It was for this reason that we chose to eliminate the need for the isolation switch by adopting a three-electrode structure as proposed in the Phase I Final Report<sup>21</sup>. Having to deal with two tandem discharges brought with it an extra level of complication, however; a subject which is discussed in more detail in Section 6.

### 3.2 MINIMUM STRESS DESIGN (RELIABILITY AND LIFETIME)

Early component failure in an electrical device is generally caused by excessive electric stress; i.e. the components are operated too close to their design limitations. Every effort has been made in the design of the present laser to reduce such stresses to a more comfortable level. The elimination of post-discharge arcing, by methods discussed above, has been a major factor in extending the potential life of the system.

A saturable magnetic core, the heart of a magnetic switch, has practically no failure mode and, therefore, has a potentially very long life. Wherever possible, magnetic switches have been employed for initiating or generating fast changes in voltage or current. Conversely, they have also been utilized for blocking voltage surges, which might damage susceptible components. The only plasma switches in the system are rugged high-voltage ceramic thyratrons which are operated in the "long-pulse Radar mode". Peak currents and rate of current rise ( $dI/dt$ ) have been kept well below the design specifications of the thyatron tubes. In the pulse charging circuit, a saturable magnetic inductor has been added to delay the thyatron from experiencing high values of  $dI/dt$  until the thyatron has safely passed through its resistive turn-on phase. This inductor also acts as a diode and isolates the thyatron from inverse voltages generated by the laser discharge PFN.

To avoid early capacitor failure, the ceramic capacitors in the PFL are stressed to only half their voltage rating. The discharge electrodes and high-voltage feedthroughs have been shaped so as to reduce corona formation at the "triple points", where conductors, insulators and the laser gas come together. A semi-empirical study of the electric field distribution in the discharge region (Section 5.1) has been of significant help in eliminating high field areas on the insulator which separates the high-voltage cathode from ground.

Preionizing the gas with X-rays instead of UV sparks eliminates the erosion of spark electrodes and the accompanying contamination of the laser gas. Since X-rays can ionize the discharge volume more uniformly, resulting in a more uniform discharge, the erosion of the main discharge electrodes is also reduced.



A similar low stress approach has been applied to the mechanical and optical components of the system. For example, the pressure vessel has been designed to safely withstand a pressure of 6 atmospheres with a safety factor of 4. Similarly, the cross section of the optical gain volume (3.5 cm X 3.5 cm) has been chosen large enough to keep the power density and energy density on the laser optics well below recognized damage thresholds.

Serious consideration has been given to the corrosive environment (laser gas may contain 0.1% HCl or F<sub>2</sub>) that the laser chamber materials are exposed to. To keep chemical deterioration to a minimum, only stainless steel, nickel and Kynar have been used in the construction of the discharge chamber, the electrodes, the insulators, the heat exchangers and the gas blower. Pressure and vacuum seals have been made with Viton O-rings to keep the cost of the laser down. However, these can easily be replaced with superior Kalrez (Dupont TM) O-rings if necessary.

### 3.3 COMPACTNESS

A cylindrical shape has been chosen for the discharge chamber for compactness and for strength. The gas is recirculated within this circular chamber by a tangential blower. A small cylindrical X-ray preionizer has been fitted into the core of the chamber. By choosing this shape for the pressure vessel, the discharge chamber weight could be kept to a minimum. A relatively thin shell of stainless steel can easily support 5 to 6 atmospheres of pressure, as well as full vacuum loading. The chamber is 0.4 m in diameter and 0.8 m long. Refer to Figure 4-3 for an overall view of the system.

The PFN is contained in an oil-filled aluminum tank situated below the discharge chamber. Overall system height is approximately 1 m, and total weight approximately 500 kg. Separate oil-filled boxes have been used for the pulse charging unit and for the X-ray pulser. An improved version of this laser will have the pulse charging circuit designed into the PFN tank. Whereas transformer oil has been used here as the insulating liquid for economical reasons, a space qualified system would use "Fluorinert C-40" fluorocarbon liquid instead.

We anticipate that with some redesign the output performance of the laser (at 308 nm) can be scaled up to 4 J per pulse and 50 Hz pulse repetition frequency (PRF) without an increase in size (see Section 9.1).

## 4.0 EXCIMER LASER CONSTRUCTION

As form follows function, we will first discuss the functional relationships and design parameters, and then present the details of the electrical, mechanical and optical construction of the laser subsystems.

### 4.1 FUNCTIONAL SYSTEM OUTLINE

A fully operational excimer laser is itself a rather complex piece of apparatus, consisting of many functionally interrelated components (Figure 4-1). The heart of the laser is the electric discharge passing transversely through the gain volume, which is the source of the stimulated optical emission. The latter is converted into the laser output beam by the optical resonator.

Electric power is taken from the supply network (240 V - 3 Phase) and is converted into a series of excitation pulses of a desired shape (Figure 2-1) in three stages. The electric energy flow is as follows: A gateable switched charging supply, operating at 16 kHz, charges upon command a long-life high-voltage capacitor (Maxwell, oil-filled aluminum foil capacitor) to a voltage which is adjustable between 10 kV and 40 kV. Normal operating voltage for the laser is 35 kV. A triggered thyatron then transfers this energy to the PFL in a time period between 1 and 2 microseconds. A saturable core reactor, L1S, acts as a thyatron assist and as an inverse blocking diode to protect the thyatron. A second (and in some cases a third) magnetic switch generates the high-voltage prepulse which initiates the electric discharge. The duration of the excitation pulse is controlled by the "electrical length" of the PFL, here approximately 140 ns.

Before and during application of the electric prepulse the laser gas is preconditioned by an intense ionizing X-ray pulse. A separate thyatron switched pulse generator, energized from a 30 kV DC supply, powers the e-gun which generates the X-rays. A variable delay and trigger unit controls the sequence of events. At  $t_0$  the switched charging supply is activated and allows charging of the Maxwell capacitor. Forty milliseconds later the discharge sequence is initiated by triggering the thyatron in the pulse charging unit with trigger pulse  $t_1$ . The energy transfer to the PFL is then controlled by magnetic switch L1S. After a predetermined time, magnetic switch L2S saturates and generates the high-voltage spike which starts the discharge. A second trigger pulse,  $t_2$ , which triggers the X-ray pulser, has to be timed precisely relative to  $t_1$ , in order for the X-ray pulse to coincide with the prepulse.

The gas between the discharge electrodes has to be cleared out and replaced with fresh gas between pulses to remove temperature non-uniformities which can lead to arcing. A tangential fan blows the gas through the discharge gap in a transverse direction and passes it through a gas-to-water heat exchanger, where the heat added to the gas by the discharge is removed. The blower is driven by an external electric motor via a magnetic coupling, which makes a hermetic seal with the chamber. Figures 4-2 and 4-3 show the physical location of components.

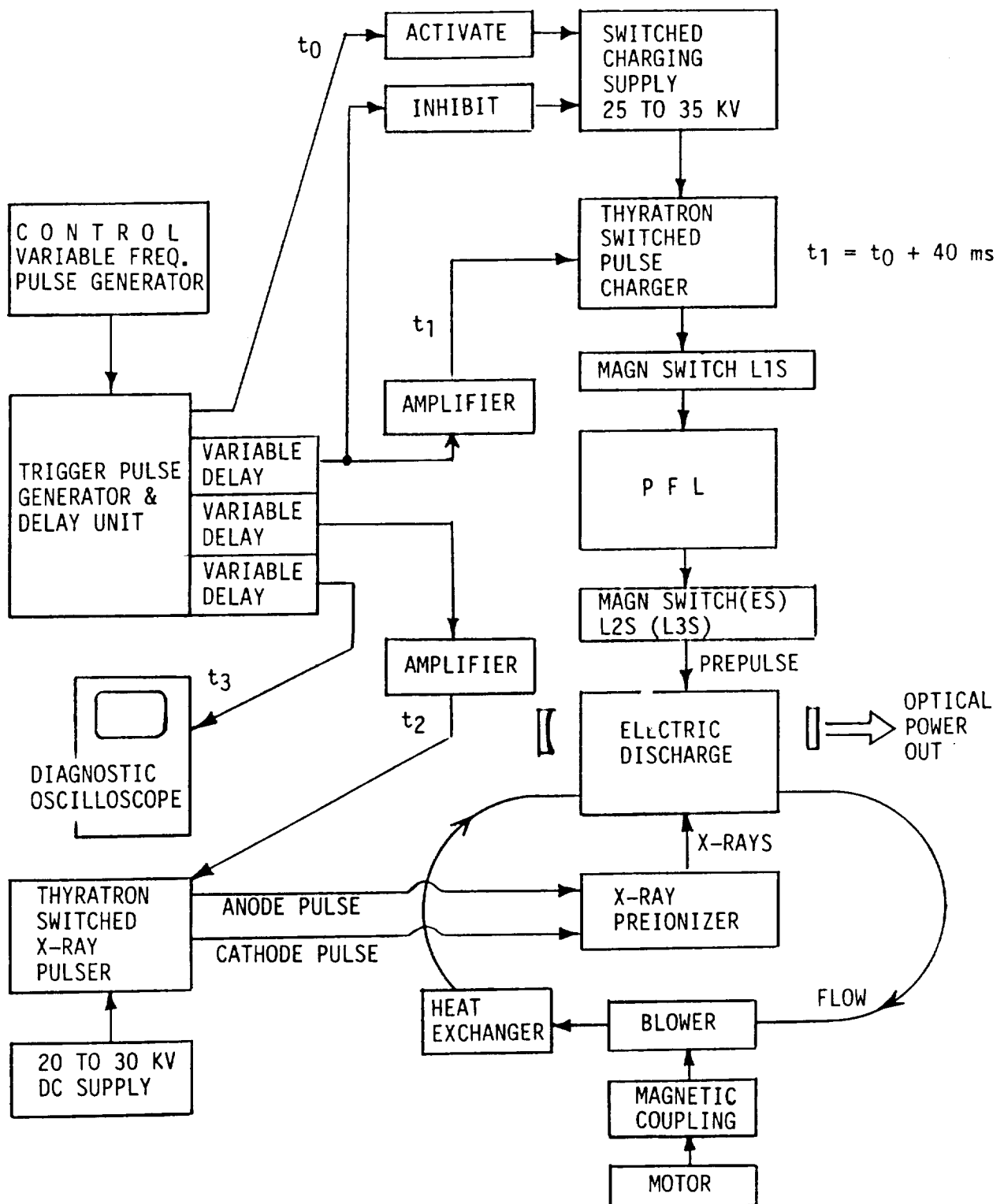


FIGURE 4-1. FUNCTIONAL OUTLINE OF SYSTEM COMPONENTS

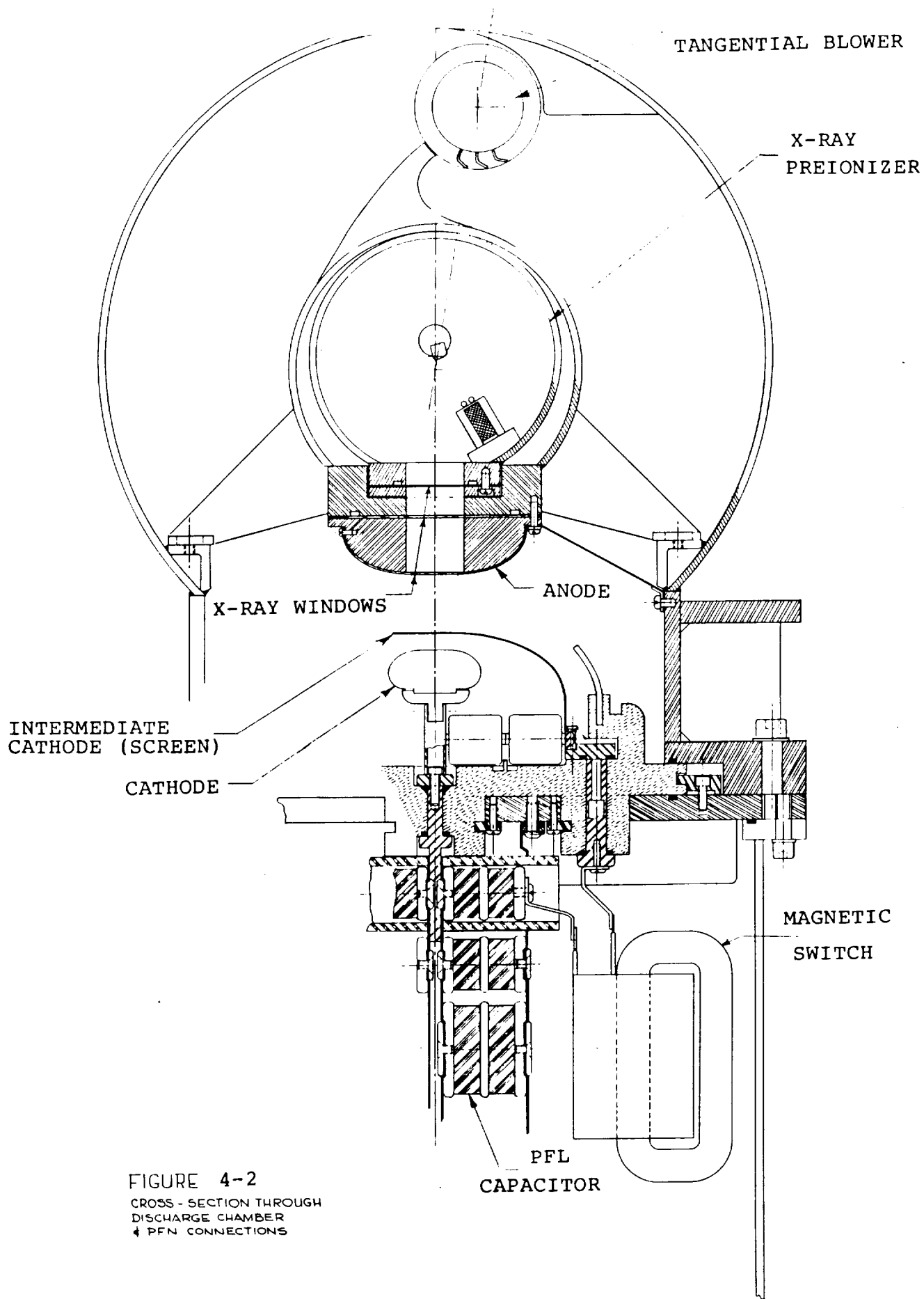


FIGURE 4-2  
CROSS - SECTION THROUGH  
DISCHARGE CHAMBER  
+ PFN CONNECTIONS

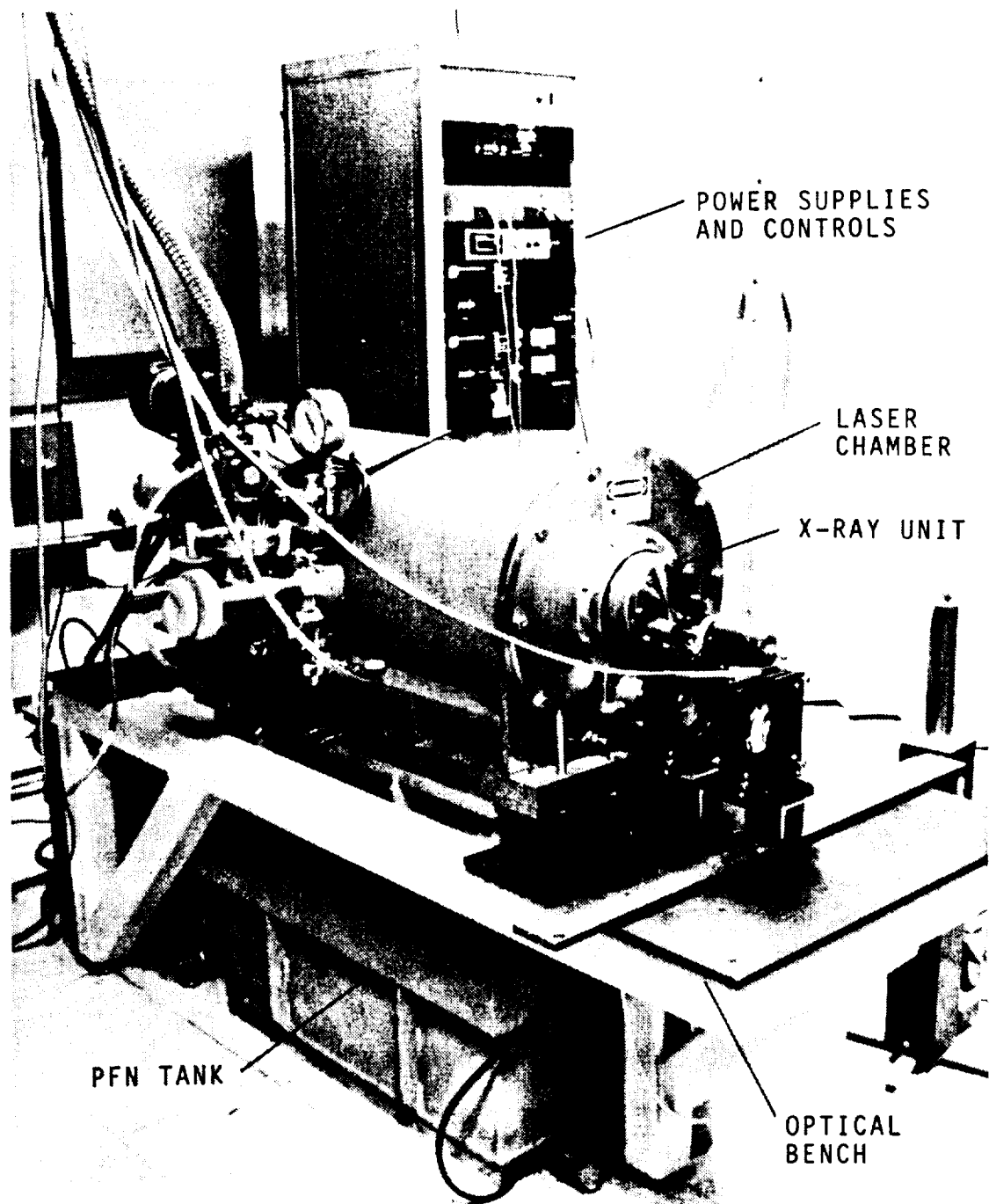


FIGURE 4-3. OVERALL VIEW OF EXCIMER LASER SYSTEM

## 4.2 DISCHARGE PARAMETERS

A typical XeCl laser mixture contains between 0.5 and 1% of xenon and 1/10 of that amount of HCl in a diluent of neon. The measured steady-state discharge field, normalized by the gas pressure, for such a gas mixture is approximately given<sup>10</sup> by  $E/p = 0.8 \text{ kV/cm-atm}$ . The design of the discharge electrodes and the choice of discharge parameters is strongly influenced by this  $E/p$ -value and by the requirement that the electric pump power density should be close to  $1 \text{ MW/cm}^3$ . The gas mixture and pump power density quoted are near optimum values, based on electron kinetic and chemical kinetic studies. Under optimum conditions approximately 14% of the applied pump power goes into the production of XeCl\* upper-lasing-state species. The gain length is determined by considerations of optical extraction efficiency, and frequency and mode control. Following is a list of design parameters for the present laser:

Total System Input Power	= 2.5 kW
Energy Stored in PFN & Switched into Discharge	U = 80 J
Pulse Repetition Frequency (PRF)	f = 10 to 25 Hz
Pump Pulse Duration	$t_E = 140 \text{ ns}$
Charging Voltage	$V_{CH} = 35 \text{ kV}$
Steady-State Discharge Voltage	$V_D = 16 \text{ kV}$
PFL Capacitance	C = 140 nF
Pump Power	P = 570 MW
Discharge Impedance & PFL Output Impedance	$R_D = 0.5 \text{ ohm} = V_D^2/P$
Main Discharge Gap	d = 3.5 cm
Pre-Discharge Gap	d' = 1.2 cm
Discharge Width	w = 3.5 cm
Gain Length	l = 60 cm
Discharge Volume (1.0 l incl. pre-discharge gap)	$V' = 0.74 \text{ l}$
Energy Density	$U/V' = 100 \text{ J/l}$
Power Density	$P/V' = 0.8 \text{ MW/cm}^3$
Gas Pressure	p = 5.5 atm
Typical Gas Mixture	Ne:Xe:HCl:H <sub>2</sub> = 99.5:0.5:0.05:0.02
Steady-State Discharge Field	$E/p = 0.75 \text{ kV/cm-atm}$

### 4.3 DISCHARGE ELECTRODES AND FEEDTHROUGHS

For reasons outlined before, a three electrode geometry was chosen to make it easier to apply a high-voltage prepulse. The electrodes consist of a primary cathode, an intermediate cathode (screen) and the anode. The predischage gap between cathode and screen is approximately one third of the main discharge gap between the screen and the anode. A cross-section through the electrode structure, including the PFN feedthroughs, is given in Figure 4-2. The cathode and the screen are supported from a flat partition plate, consisting of a structural stainless steel plate, with ribs to support the chamber pressure, and a Kynar insulator. The Kynar insulator has been machined out of a solid 10 cm X 30 cm X 120 cm block. The cathode is connected to the center plate of a double transmission line via four oval stainless steel feedthroughs. Access to the screen is provided by eight similar feedthroughs, four on each side. A view of the underside of the partition plate, showing the twelve Kynar insulated feedthroughs, is presented in Figure 4-4.

The contours of all electrodes are constructed from flat sections and elliptical curves and closely approximate compacted Chang<sup>22</sup> profiles. The cathode is an inductively ballasted electrode, consisting of a stack of several hundred thin stainless steel fins, held together by two stainless steel rods, running end to end (Figure 4-5). The fins (Figure 4-6) have been chemically etched out of 0.13 mm thick sheet. The screen electrode (intermediate cathode) has been formed from 0.6 mm thick stainless steel sheet (Figures 4-2 and 4-7). It has a fine hole pattern chemically machined along its center, in the discharge region, to allow UV radiation to pass from the pre-discharge gap to the main gap and vice versa. A coarse hole pattern has been etched into the sides of this electrode (Figure 4-7) to permit the gas flow to pass between cathode and screen.

The anode is supported from the central support structure of the discharge chamber which holds the X-ray generator (Figure 4-2). It has been machined out of solid stainless steel and has a window along its center, so that X-rays can pass into the discharge region to preionize the gas. The anode is covered with a thin nickel plated aluminum sheet, 0.8 mm thick. The X-rays have to pass through this sheet, as well as through two similar aluminum windows. The additional X-ray windows are used to support the pressure differences between the laser gas (5 atm) and the ambient atmosphere, and between the atmosphere and the vacuum of the X-ray chamber. There is no pressure load on the anode skin. The combined thickness of the X-ray windows is less than 3 mm, and it is estimated that less than 35% of the X-ray flux is absorbed in these windows. Since there exists a concern about the lifetime of the 50 micron thin nickel coating on the anode skin, this skin is easily replaceable with other experimental window materials, e.g. an uncoated 0.6 mm thick titanium sheet. The anode remains at electrical ground potential. Fine-mesh nickel wire screens, connecting the anode to the discharge chamber on both sides, act as current return connections and as gas flow conditioners.

In operation, with the original prepulse scheme, the small gap between cathode and screen would break down first, generating a voltage pulse on the main gap with the aid of the closely coupled prepulse capacitors (Figure 4-5). Once

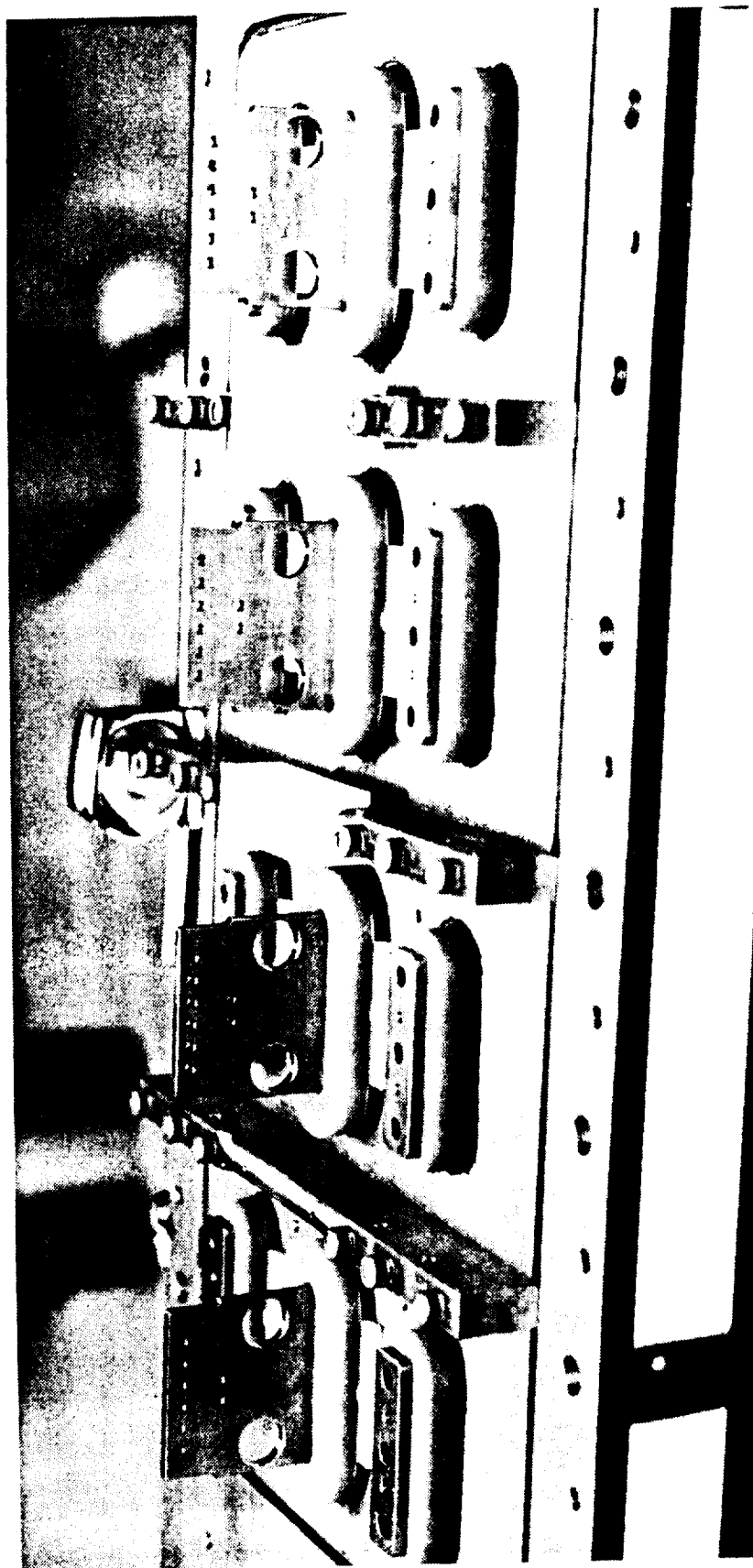


FIGURE 4-4. UNDERSIDE OF SUPPORT PLATE (PARTITION PLATE) SHOWING  
KYNAR INSULATED CATHODE FEEDTHROUGHS



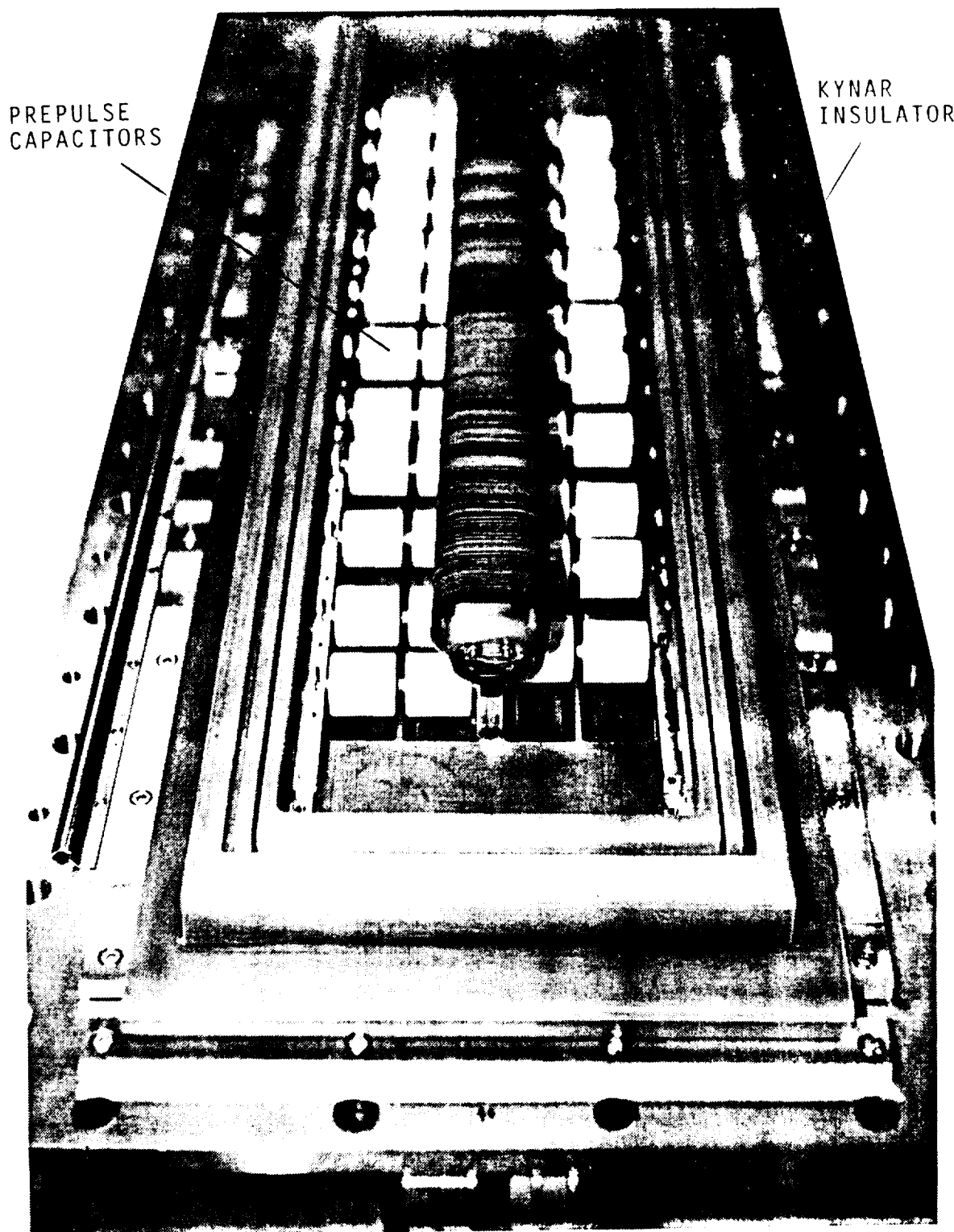


FIGURE 4-5.  
CATHODE INSTALLED ON PARTITION PLATE  
(ST. STL. SUPPORT PLATE AND KYNAR  
INSULATOR)



FIGURE 4-6. CATHODE FIN (ACTUAL SIZE)

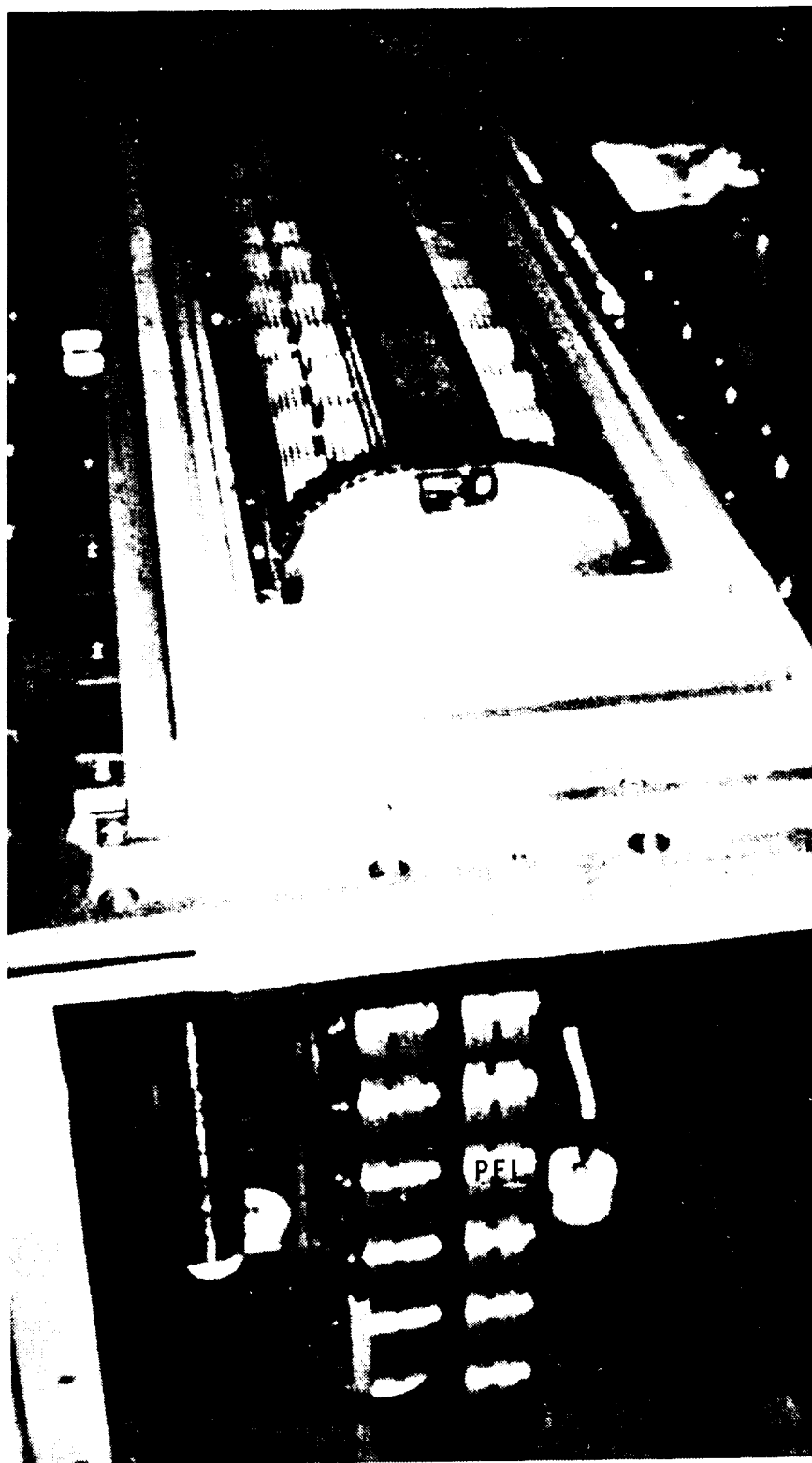


FIGURE 4-7. SECONDARY CATHODE (SCREEN) INSTALLED OVER  
PRIMARY CATHODE

the main gap ignites, the discharge current has to pass through both gaps in series. During this phase, the power density deposited in the pre-discharge gap is very high. The inductive ballasting built into the primary cathode was intended as an aid to keep the discharge in the small gap evenly distributed along its length. Intense UV radiation from the "pre-discharge" was then meant to help sustain the main discharge for extended pump periods. Furthermore, the early phase of the predischage was to be utilized as a possible gain medium for a master oscillator for injection locking the power oscillator built around the main discharge. As will be discussed in Section 6.1 this scheme has been abandoned for the time being in favor of a direct excitation of the main gap.

#### 4.4 PULSE FORMING NETWORK

The attainment of a smooth, stable, steady-state discharge voltage,  $V_D$ , for the duration of the power pulse is extremely important for achieving high frequency stability and optical mode stability. The required constant-voltage excitation pulse can best be generated with a distributed-impedance pulse forming line (PFL). Some of the best results have in the past been obtained with water transmission lines.<sup>7,10,11</sup> Such lines would have disadvantages for space and airborne applications, however. For a 120 ns pulse, the PFL would have to be 2 m long, so that it could not easily be incorporated into a compact system. Also, special precautions would have to be taken to keep the water from freezing. We have, therefore, chosen to work with a double transmission line PFL constructed from barium titanate ceramic capacitors. The physical construction of the PFL is discussed hereunder, the electrical configurations of the PFL and prepulse circuits are discussed in more detail in Sections 5 and 6.

The ceramic disc capacitors were purchased unencapsulated, but polarized and metallized, from the Ceramite corporation. Rounded brass corona discs were then attached by oven-soldering with a eutectic tin-bismuth alloy (melting point 130° C) for reasons outlined in the Phase I Report<sup>21</sup>. Each unit was constructed by soldering two 2.2 nF, 30 kV discs in series, with a corona disc on each end and one in the center (Figure 4-8). These capacitor units were then assembled into eight parallel-plate transmission lines, each two capacitors wide and eight capacitors long. The capacitors were sandwiched between 0.5 mm thin soft copper sheets. Low-impedance connections were made by drawing the copper "foil" into the capacitor end caps with brass clamping discs (Figure 4-2). The edges of the copper sheets were electrically "graded" by encasing the sharp edges in resistive (approximately 100 ohm-cm) silicon-rubber tubing. The extruded tubing was slit along its length and cemented around the copper edge with conductive epoxy. The eight ceramic PFL sections were arranged in a double-transmission line configuration with an output impedance of 0.5 ohm. The center plates were attached to the cathode feedthroughs and the outside plates to the stainless-steel partition plate (electrically connected to the anode). The prepulse circuits, containing several magnetic switches were attached to the screen cathode (Figure 4-8).

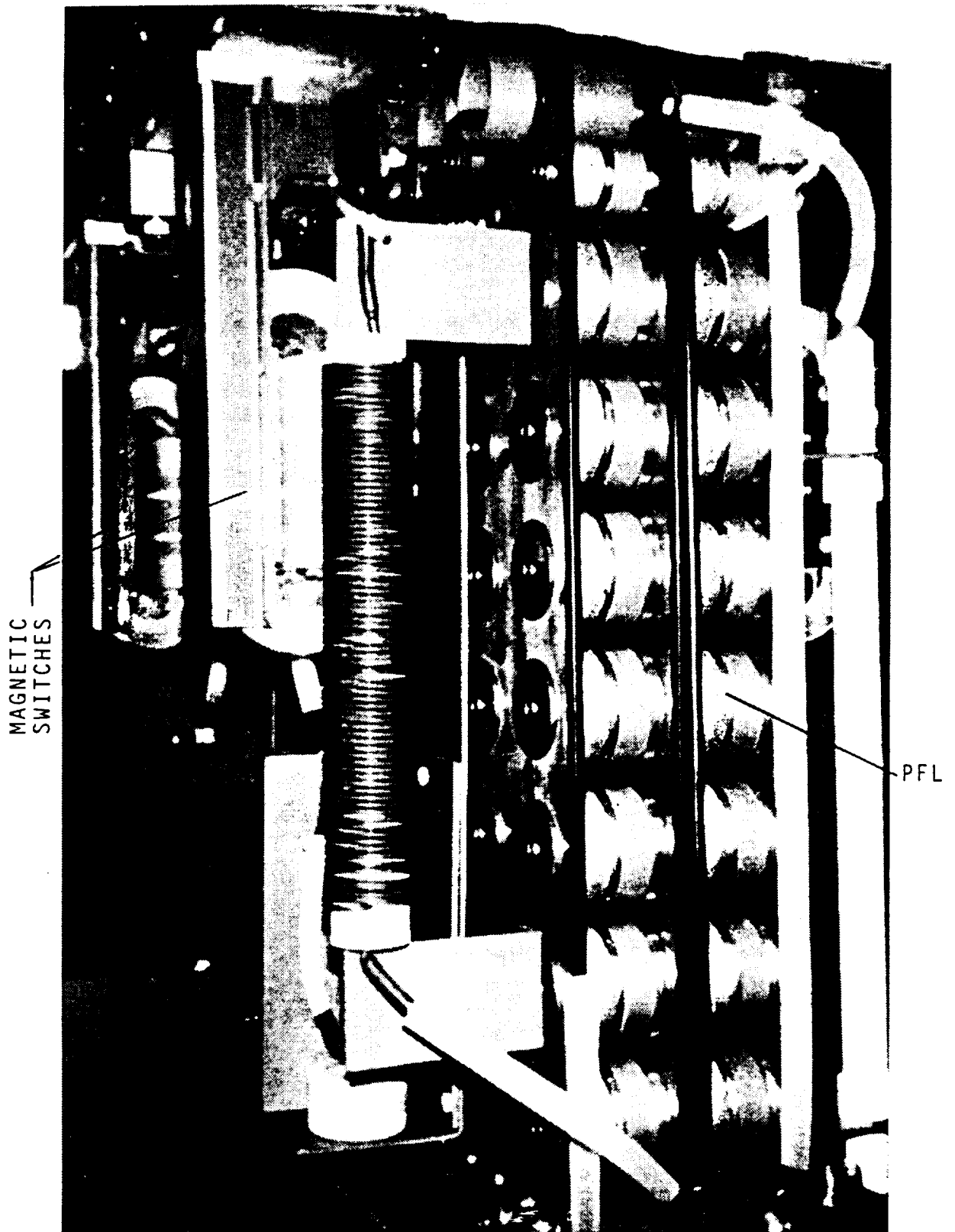


FIGURE 4-8. PULSE FORMING LINE WITH MAGNETIC SWITCHES  
INSTALLED

The entire PFN has been immersed in electrical-grade insulating oil, which is contained in a rectangular reinforced aluminum tank (Figure 4-3). The tank, which is sealed to the bottom of the discharge chamber, is filled by first evacuating the tank of all air, then backfilling with oil which has been thoroughly outgassed under vacuum.

#### 4.5 PULSE CHARGING UNIT

The pulse charging unit has been contained in a separate electrically shielded aluminum tank, which is also filled with transformer oil. It contains a high-voltage EG&G LS-4011 thyatron, a long-life, high-PRF 160 nF Maxwell capacitor, and a saturable magnetic inductor, which acts as a thyatron assist and protective diode (Figure 4-9). The thyatron is a 40 kV, 10 kA, double-grid ceramic tube, one of a new series of ruggedized thyatrons made especially for high energy laser excitation. The saturable inductor has three electrical turns (originally 5 turns), wound on a 2605-CO Metglas core with a  $V \cdot t$ -product of approximately 8 mV-s. Also contained in the pulse charging tank are an RC snubber circuit to help in the commutation of the thyatron, a 1 megohm bleeder resistor, two 100 ohm supply ballasts, a high-voltage diode to isolate the core reset circuit, the thyatron grid drive circuit and the transformers and regulators to supply the heater and reservoir voltages (6 V AC). A co-axial high-voltage feedthrough connects the pulse charging unit to the PFN. This feedthrough, and connector, has been constructed such that the charging tank and the PFN tank can be disconnected and physically moved apart without draining the oil out of either tank.

In operation, the 160 nF capacitor is command-charged from an A.L.E. 302L high-voltage, 3 kW switching supply and an A.L.E. 302S, 3 kW slave unit, connected in parallel, in approximately 30 ms. After being fully charged, the energy stored in the capacitor (Maxwell) is transferred to the PFL by triggering the thyatron. The trigger pulse is derived from a Stanford DG-535 pulse/delay generator and is amplified to 1 kV before being applied to the thyatron grids. Several metal-oxide varistors (MOVs) protect the pulse and delay generator from high-voltage transients. The saturated inductance of the Metglas inductor (with three turns) is 800 nH and permits the energy to be transferred to the PFN in approximately 1.1 microsecond. Before triggering the thyatron, the core of the saturable inductor is reset by a pulse from a core reset circuit described in Section 6.3. The arrangement of components in the pulse charging tank is illustrated in Figure 4-10.

#### 4.6 X-RAY PREIONIZER AND PULSER

A novel long-life, large-area X-ray generator has been developed here to provide an intense pulse of non-contaminating ionizing radiation for preconditioning the laser gas. The high-current-density (space-charge limited) e-gun has been designed around a set of rugged, reliable and long-life electrodes. The electron source at the cathode is a corona plasma formed at the interface between a conductor and a high-permittivity dielectric. The

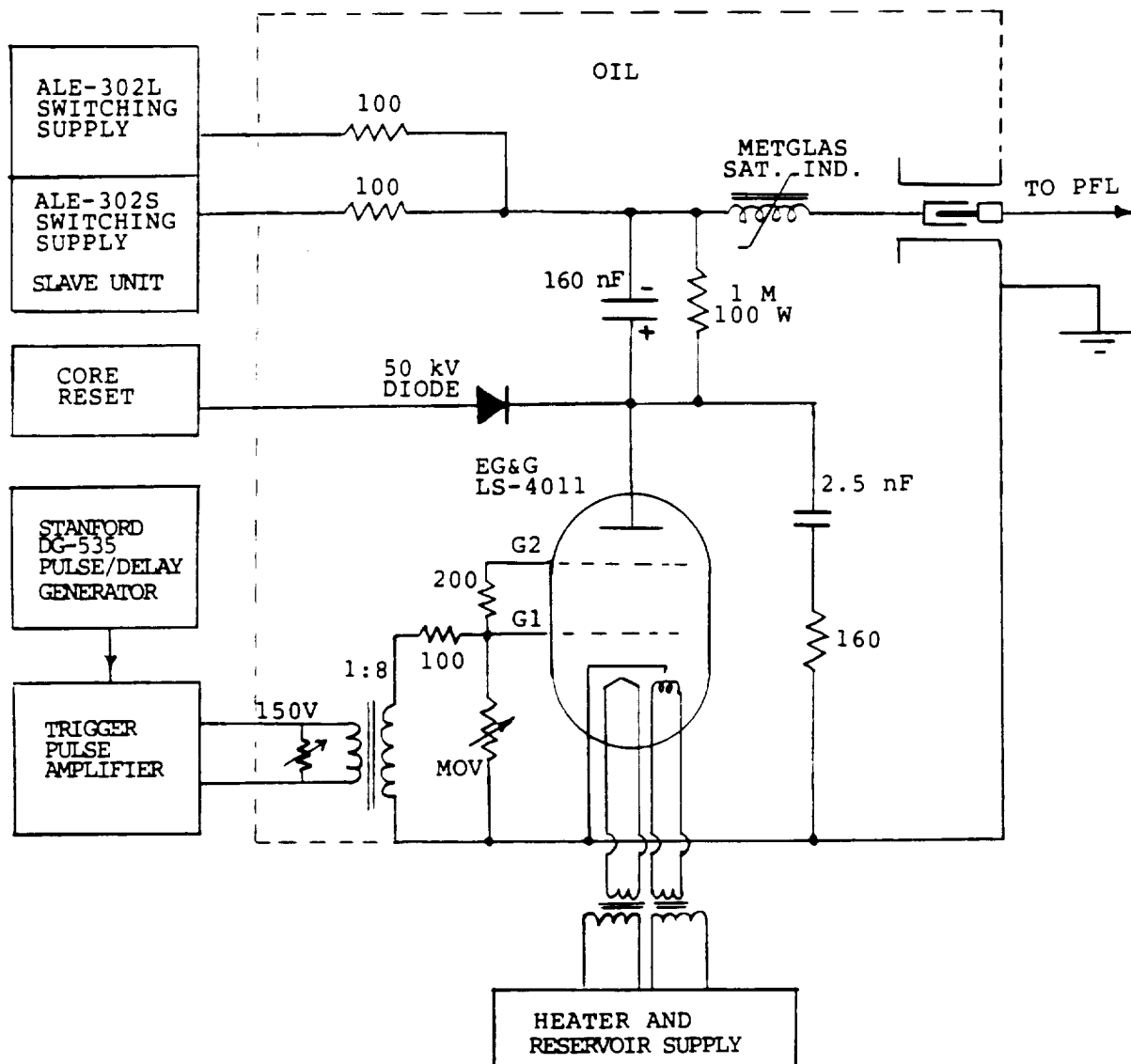


FIGURE 4-9. SCHEMATIC OF PULSE CHARGING UNIT

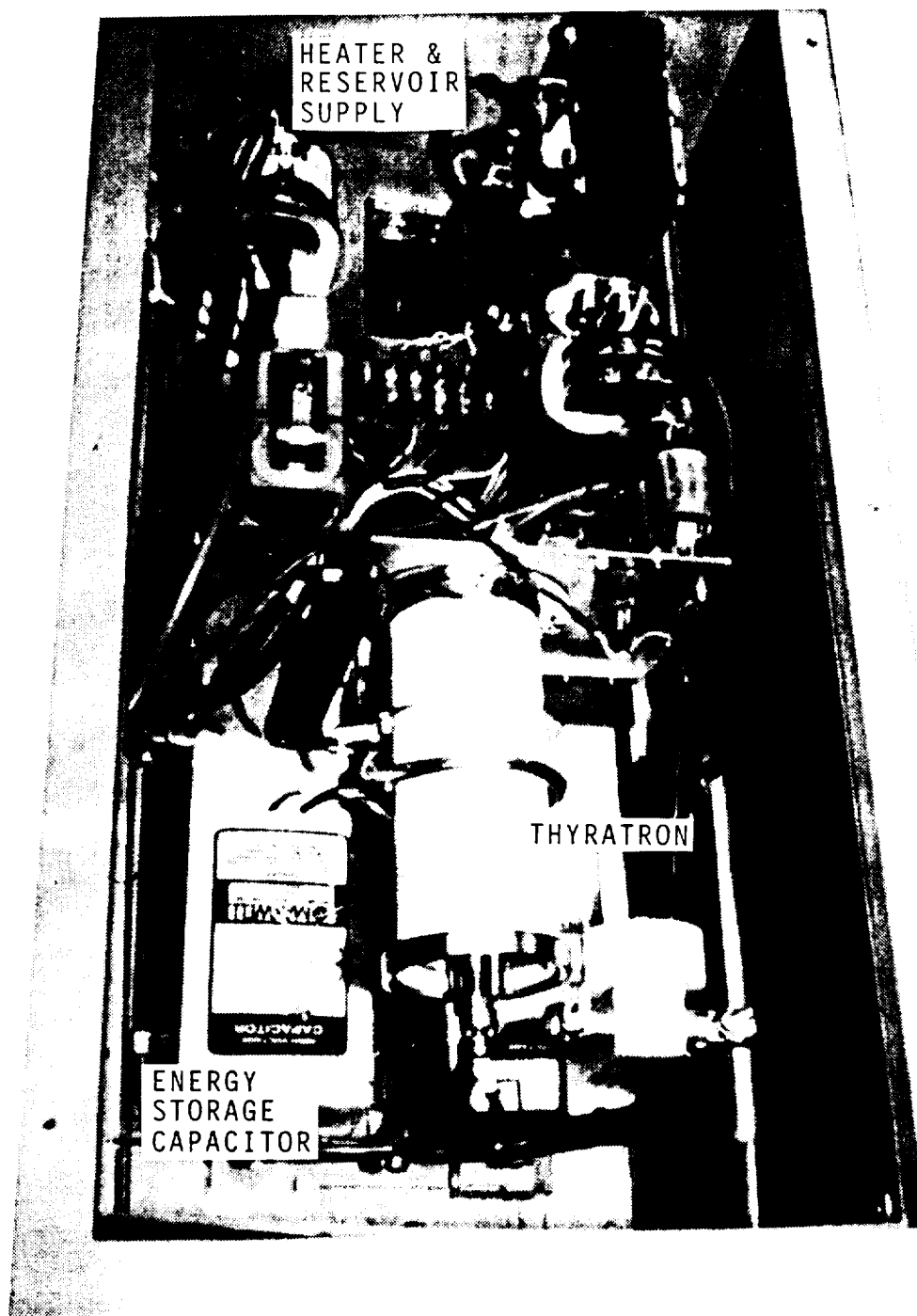


FIGURE 4-10. TOP VIEW OF PULSE CHARGING UNIT  
SHOWING LOCATION OF COMPONENTS

anode and e-beam target is liquid-cooled, emits in the more efficient backward direction and is shaped to concentrate the X-ray flux toward the X-ray window.

Efficient, large-area X-ray preionization of high-energy lasers requires electron guns with space-charge limited e-beam current densities in the range of 1 to 10 A/cm<sup>2</sup> and short pulses of less than 1 microsecond duration. A number of cold-cathode guns have been developed to fill this need. However, most of these devices suffer from limited cathode life (10<sup>3</sup> to 10<sup>7</sup> pulses).

Electrically pulsed, self-sustained discharge excited, high energy gas lasers (e.g. XeCl, KrF, XeF, CO<sub>2</sub>, HgBr lasers) need uniform preionization of the high-pressure gas mixture for discharge uniformity and stability. For optimal laser efficiency and laser beam uniformity, the preionization level should be between 10<sup>8</sup> and 10<sup>9</sup> electrons per cm<sup>3</sup>. Preionization uniformity should be within  $\pm 20\%$  throughout the discharge volume; hence, X-ray uniformity should also be within 20 per cent.

Available e-guns differ primarily in the manner in which electrons are liberated in sufficient quantity at the cathode. Hot cathodes (e.g. thoriated tungsten) require hard vacuum, large heater power, and for thermionically limited emitters, have insufficient current density (less than 100 mA/cm<sup>2</sup>). Cold field-emission cathodes (sharp blades, needles, carbon felt) are simple and rugged, but exhibit very non-uniform emission characteristics after 10<sup>6</sup> pulses (sometimes after 10<sup>3</sup> pulses). A carbon felt cathode design with a control grid has recently been patented<sup>23</sup>. Such a cathode, however, is not suitable for pulse repetition rates above a few hertz<sup>24</sup>.

Only so-called plasma cathode guns have demonstrated lifetimes in excess of 10<sup>8</sup> pulses, when operated in the short pulse (less than one microsecond) and high current density (greater than 1 A/cm<sup>2</sup>) regime. With proper anode cooling, plasma cathode guns can also be run at high PRF (above 100 Hz).

In 1982 a corona plasma cathode was developed by Helionetics<sup>25</sup> (HLX Laser, Inc.), which had a cathode consisting of a tungsten wire coil wound around a glass tube. The anode was a "forward emitting" gold foil target at ground potential. When a high negative voltage pulse (-100 kV accelerating potential) was applied to the wire coil on the cathode, the electric field between it and a grounded conductor inside the glass tube initiated a surface glow on the outside of the dielectric tube. This corona plasma served as the electron source. Because no high DC voltages had to be sustained by the system, this type of gun could be made quite compact. This corona cathode has a more uniform emission<sup>24</sup> than a carbon felt cathode<sup>23</sup> and has a potential life of more than 10<sup>8</sup> pulses<sup>25</sup>. Pulse rates as high as 200 Hz are possible with this type of gun, although cooling becomes a problem. Whereas the HLX gun represents a significant advance over the then existing state of the art, it suffers from several serious drawbacks:

1. The cathode is subject to catastrophic failure due to cracking or electric breakthrough of the highly stressed pyrex tube.
2. Non-uniform erosion of the dielectric tube and the thin fragile tungsten wire tends to make the electron emission less uniform as the tube ages.



3. The device relies on the less efficient X-ray emission in the forward direction from a high-Z foil (anode).
4. Anode cooling becomes a problem at high PRF.

The X-ray preionizer developed here has a more rugged corona plasma cathode and has all the advantages of the HLX gun, but none of the above limitations. The salient features of the Lasertechnics gun are:

1. Compact design. The gun is contained in a 14 cm diameter cylinder.
2. Rugged cathode design. The corona plasma is produced at the interface between a high-permittivity dielectric and a thick nickel structure.
3. The cathode is not subject to catastrophic failure. The dielectric is not used as an insulator to support high voltages.
4. The cathode structure has enough bulk for ablation to permit the generation of  $10^{10}$  corona plasmas. The life of the cathode is not limited by the material in the cathode.
5. A central liquid-cooled anode, suitable for high PRF, acts as the electron target, the X-rays being emitted in the more efficient "back direction".
6. The X-ray emitter is a thick, high-Z metal coating (e.g. 100 microns of gold), which makes good thermal contact with the cooled anode body.
7. The emitter surface is shaped so as to preferentially direct ("focus") the X-rays toward the X-ray window.
8. The gun chamber does not require high vacuum levels. Background pressure may be as high as  $5 \times 10^{-4}$  torr.
9. No high DC voltages are employed. The anode is driven to 90 kV in a 250 ns pulse, while a 10 kV pulse is applied to the cathode to generate the corona plasma.
10. The anode and cathode pulser circuits are switched by the same thyatron, requiring only one timed trigger pulse.

Figure 4-11 shows a schematic of the X-ray generator and pulser. The e-gun electrodes are enclosed in a cylindrical vacuum chamber, with the high-voltage anode running along its center. The chamber walls are made of relatively heavy (6 mm thk.) stainless steel and help to shield operating personnel from stray X-rays. The anode pulse, used to accelerate the electrons, and the cathode pulse, used to create the corona plasma, are generated simultaneously by the pulser shown schematically in Figure 4-11. Approximately 5 J of electric energy are stored in the PFN, when it is charged to 25 kV from a DC power supply. The PFN consists of a series of capacitors and inductors configured to produce a 250 ns (FWHM) near-rectangular pulse, when the thyatron switches one side of the PFN to ground. A 1:4 pulse transformer serves to step up the voltage from 25 kV to 100 kV, which is then applied to the anode via the high-voltage feedthrough at one end of the vacuum chamber. The pulse transformer has been wound on a set of 32 Ferroxcube 3C8 toroidal ferrite cores with a multifilar winding to keep the leakage inductance to a minimum. The large number of cores were necessary to eliminate core saturation effects, since only three primary turns and twelve secondary turns of high-voltage cable could be fitted through the cores (3.7 cm ID). The cathode pulse is produced simultaneously with the anode pulse by switching a small capacitor, containing less than one joule of energy, to ground by means of the same thyatron. A second 1:1 pulse transformer inverts the polarity of

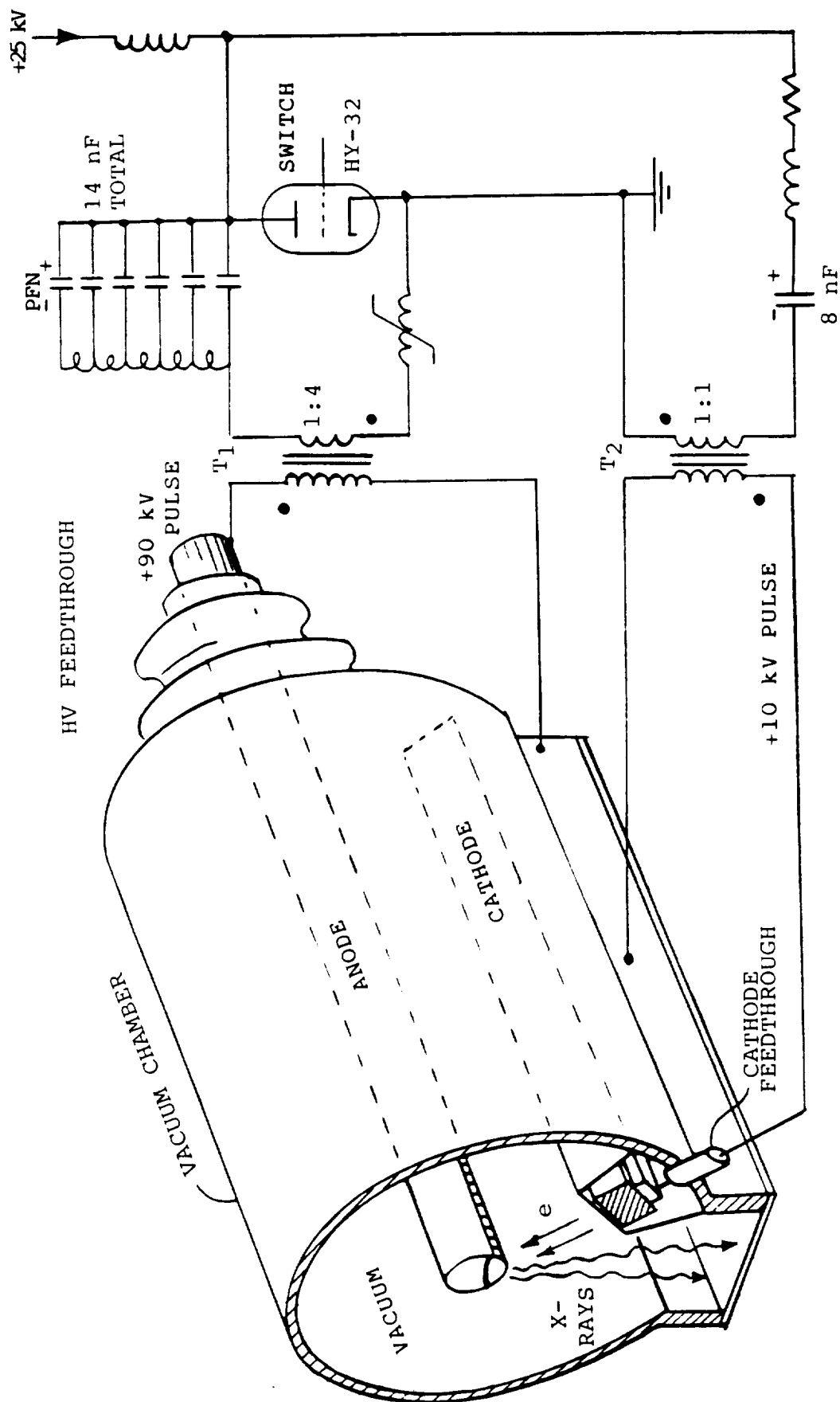


FIGURE 4-11. SCHEMATIC OF X-RAY GENERATOR AND PULSER

the cathode pulse from minus to plus. The duration and shape of this pulse is modified by an LR circuit in such a way as to provide a high  $dV/dt$  across the cathode dielectric at the same time when the anode voltage is at a maximum.

The cathode (Figure 4-12) consists of a series of bare barium-titanate discs sandwiched between a conductive bar and a 0.5 mm thick perforated nickel sheet. The nickel screen is in intimate contact with one surface of the high-permittivity dielectric. The edge of the screen is protected by a field grading metal bead. The assembly has been potted in epoxy, except for the top surface of the dielectric and the nickel screen, which remain exposed. The metal screen is electrically grounded. When the cathode pulse of +10 kV to +15 kV is applied to the backstrap, a high electric field is created between the dielectric surface and the screen. This field is highest at the "triple junctions" where metal, ceramic and vacuum meet, i.e. around the edge of the perforations in the nickel sheet. As a consequence, a corona plasma forms in these areas.

Whereas the corona plasma may be initiated by field emission, the surface glow is maintained by a number of electron emission processes. Positive ion bombardment and photoelectric emission certainly play an important part. The corona plasma, created from material desorbed and ablated from the dielectric surface, rapidly spreads over the nickel screen and provides a source of positive ions, which are pulled into the nickel surface to generate sufficient secondary electrons to maintain a space-charge limited electron beam. No corona is formed between the backstrap and the dielectric, because the back surfaces of the barium-titanate discs are metalized, and the backstrap is solidly connected to these metal films.

The anode consists of a brass rod, having high thermal conductivity. It is located near the center of the gun chamber, so that the electric field focuses the electrons onto the anode (Figure 4-13). Copper cooling tubes have been provided for removing heat from the anode by means of a suitable cooling liquid (deionized water, oil, freon). The electron target area has been plated with a 50 micron thick gold film for efficient X-ray production. X-rays are emitted in a flat cosine distribution, resulting in a widely diverging X-ray flux, if the target area was flat. A fair degree of collimation has been achieved by making the target area concave, as shown in Figure 4-13. In order that the accelerating field not be disturbed by the concave target surface, a thin wire screen with more than 80% transmission has been wrapped around the cylindrical anode.

Measured X-ray generator pulse shapes are reproduced in Figure 4-14. Electrode length is 75 cm and the anode-cathode spacing is 5 cm. The anode voltage pulse (FWHM = 250 ns) reaches a peak voltage of 90 kV. The e-beam current has a pulse width of approximately 250 ns and reaches 300 A at the peak. Peak power of the X-ray flux is approximately 150 kW. Values of measured currents and voltages indicate that the e-gun is operating close to the space-charge limited regime.

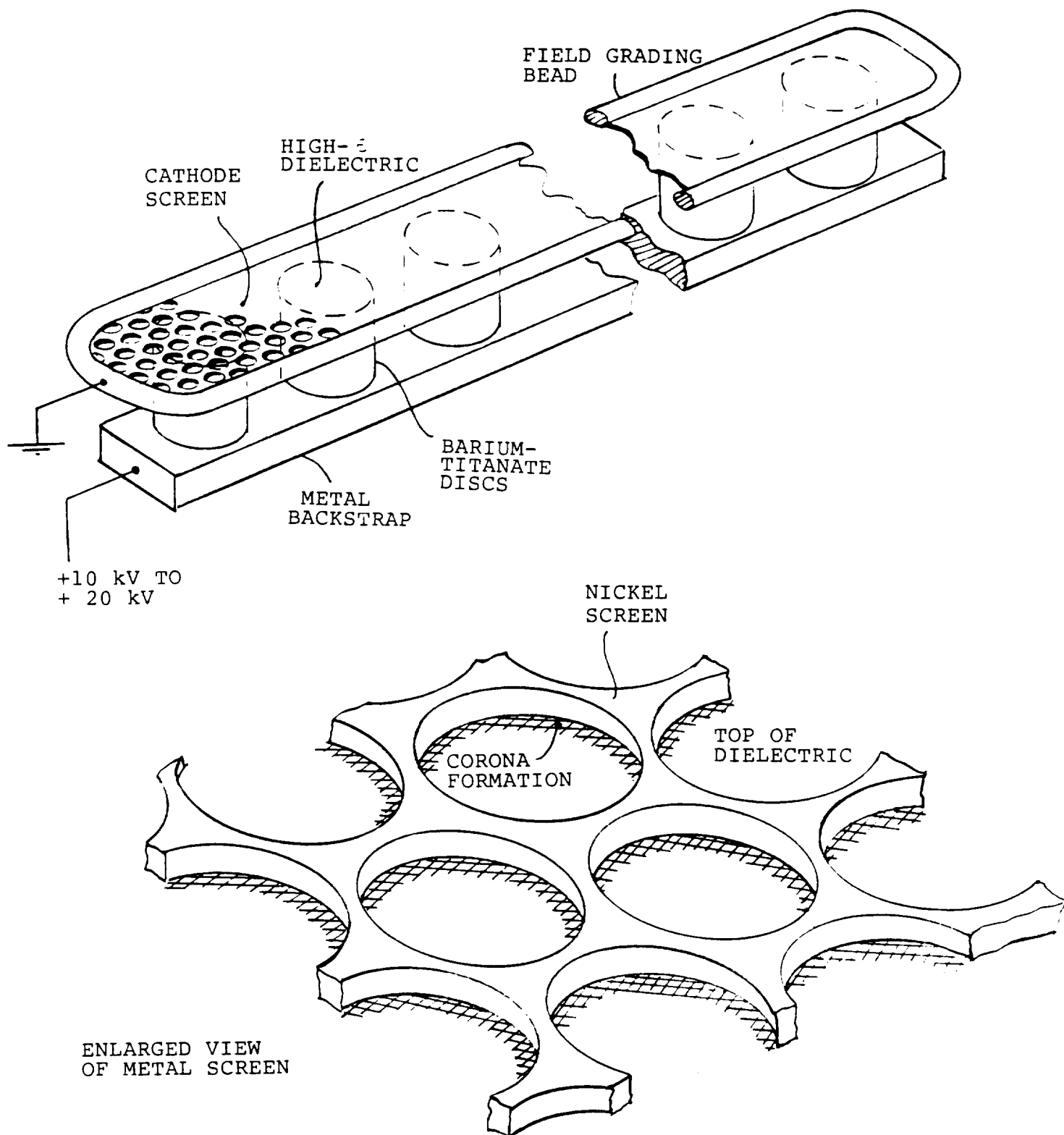


FIGURE 4-12. E-BEAM CATHODE DESIGN

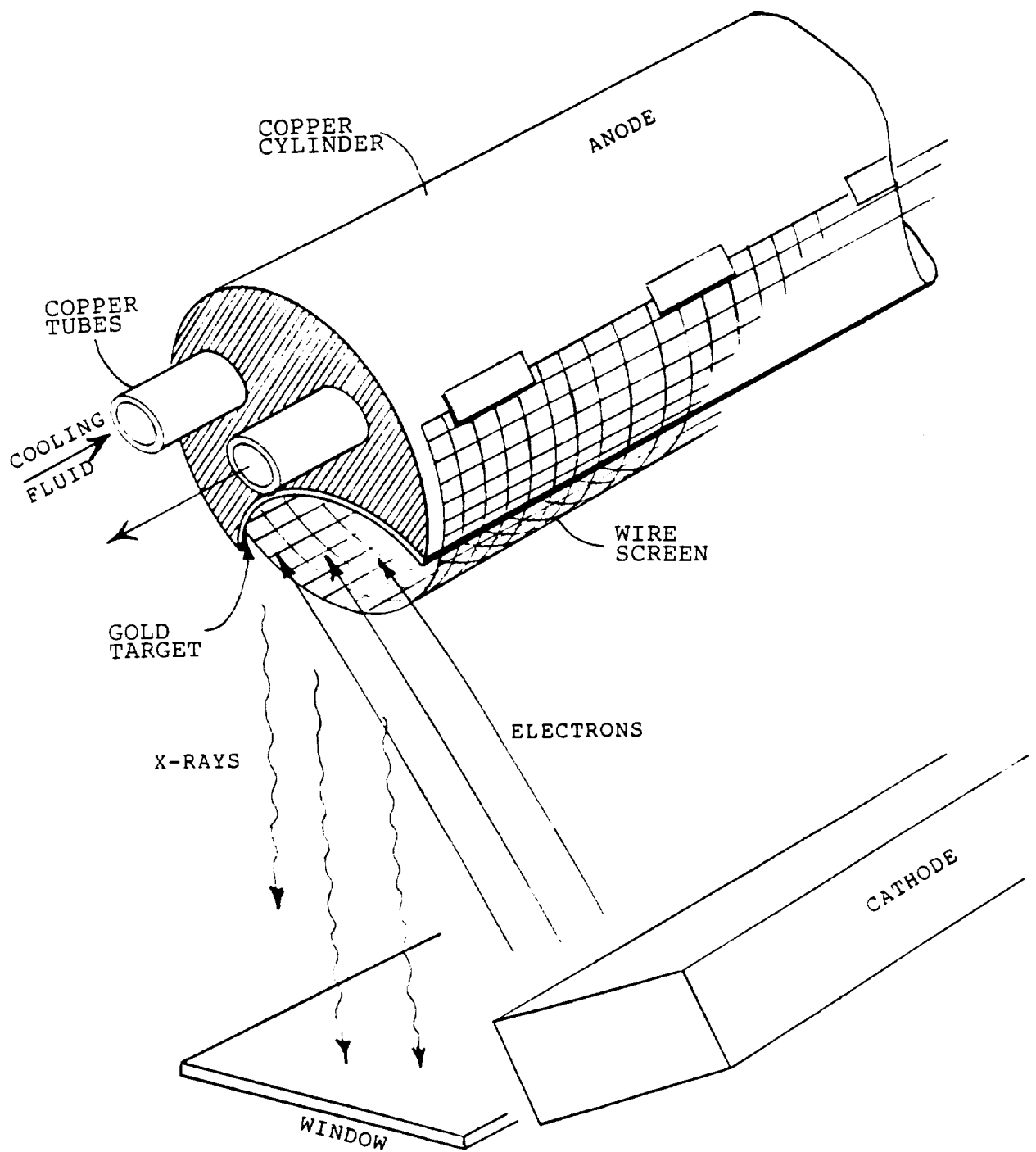


FIGURE 4-13. E-GUN ANODE DESIGN

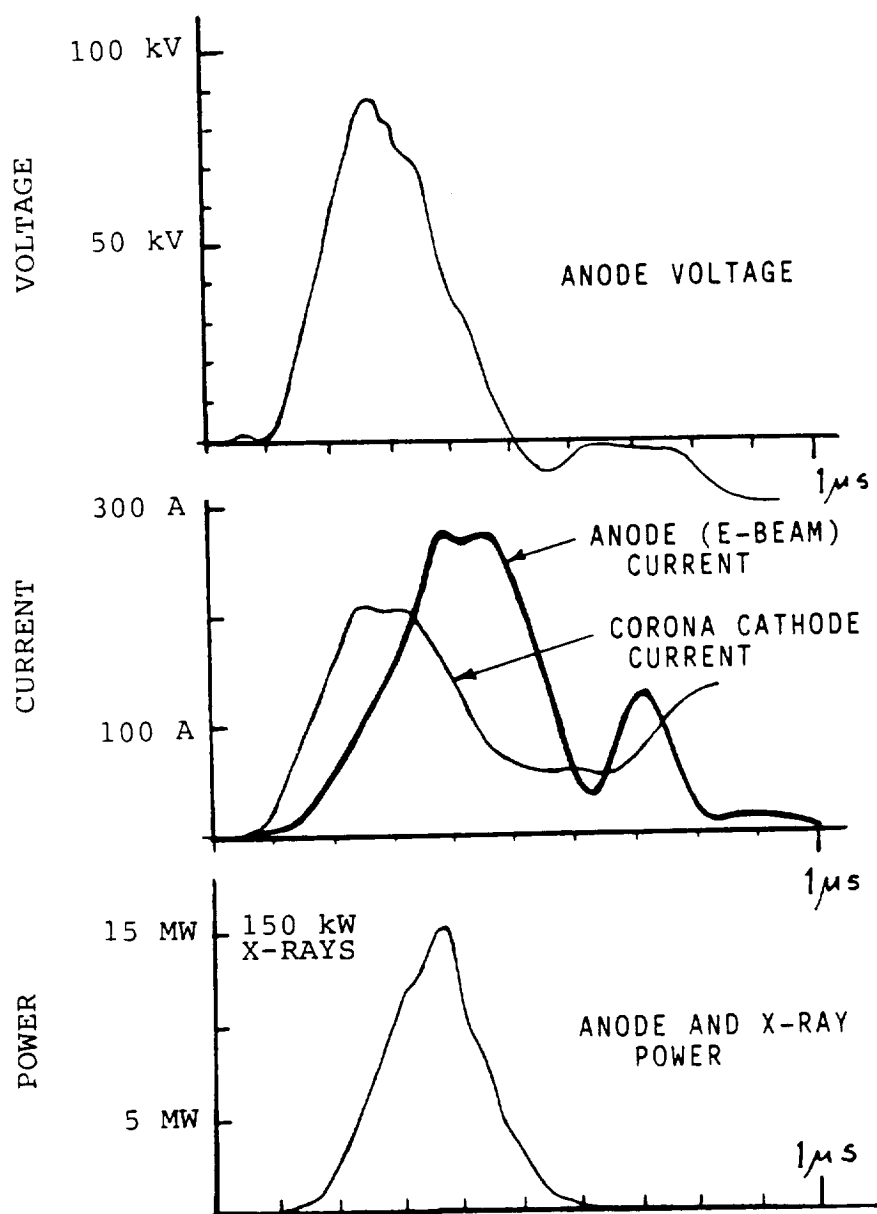


FIGURE 4-14. X-RAY GENERATOR PULSE CHARACTERISTICS

#### 4.7 TRIGGER AND DELAY CIRCUITS

The system contains two thyratrons which need to be triggered at specified times  $t_1$  and  $t_2$  relative to a reference time  $t_0$ . These pulses are supplied and controlled by a Stanford DG-532 digital delay generator with 4 output channels (Figure 4-1).

The A.L.E. switched charging supplies have been wired so as to normally inhibit charging. At time  $t_0$ , a pulse is sent to a bistable multivibrator circuit which generates a 25 V bias to override the inhibit signal, thereby activating the charging supplies until the bias is removed by signal  $t_1$ . The combined power of the A.L.E. 302L and 302S supplies (6 kW) permits charging the 160 nF storage capacitor in approximately 25 ms. At time  $t_1$ , generally set for  $t_0 + 40$  ms to allow operation at PRFs up to 25Hz, a trigger pulse is sent out to fire the thyatron in the pulse charging unit. After being amplified to 150 V, this trigger signal is stepped up to 1 kV in a 1:8 pulse transformer to trigger both grids of the thyatron (Figure 4-9). At the same time, the bias is removed from the inhibit circuit of the switched charging supply, preventing further charging.

After approximately another 1.5 microseconds, a second pulse,  $t_2$ , fires the thyatron in the X-ray pulser, after having been amplified to 500 V. Pulses  $t_1$  and  $t_2$  have to be timed with an accuracy of 50 ns, so that the X-ray pulse overlaps with the prepulse (Figure 2-1). The time interval between  $t_1$  and  $t_2$  is determined by the transfer time of charge from the charging unit to the PFL, the V.t-products of magnetic switches L1S, L2S, L3S, the degree of reset applied to the cores of these magnetic inductors, and the inherent turn-on delay times of the thyratrons. To position the X-ray pulse correctly in time to coincide with the prepulse, the voltage on the laser "screen" electrode is monitored with a GHz oscilloscope. The screen voltage and the e-beam current pulse are displayed alternately, and the timing of  $t_2$  is adjusted to bring the e-beam current into coincidence with the prepulse. The timing of pulse  $t_3$  (Figure 4-1), which is used to trigger the diagnostic oscilloscope, can be adjusted to permit viewing of the relevant portions of the screen electrode pulse with a 100 ns/cm sweep speed.

#### 4.8 GAS FLOW AND COOLING

Operation of the laser at PRFs exceeding 1 pulse per second requires the gas to be circulated within the cylindrical discharge chamber (Figures 4-1, 4-2, 4-3). The gas sweeps out the discharge volume in a transverse direction, then passes through a set of heat exchangers to remove the heat added to the gas by the electric discharge. The design of the components for handling and conditioning the laser gas are discussed in this section.

##### Tangential Blower

A stainless steel tangential blower, 7.6 cm in diameter and 80 cm long, has been designed and built to suit the requirements of this particular laser.

The impeller blades and support discs have been welded together to form a rigid structure capable of sustaining rotational speeds of 3000 RPM without excessive distortion. The impeller, which consists of two sections, has a 9.5 mm shaft and is supported by three ball bearings, one at each end and one in the center. The unit was bench tested with special silicon nitride ball bearings at speeds up to 3000 RPM, at which point one of the bearings cracked. The damage is believed to have been caused by excessive vibrational stresses.

Silicon nitride bearings were originally selected, because they can run at high speeds without lubrication. Also the material is chemically inert to HCl, although some concern exists about the compatibility of silicon nitride with fluorine. Even though the bearings failed during test, we believe that silicon nitride bearings can be made to work with the following precautions and modifications:

1. The present application requires more robust bearings (for 12.7 mm diameter shaft or larger), perhaps roller bearings instead of ball bearings.
2. With a three-bearing design, the bearing mounts have to be perfectly colinear to within 1/10,000 inch (2.5 micron).
3. The impeller sections and the magnetic drive have to be perfectly dynamically balanced.

To make the impeller in one section, supported by only two bearings, would help a great deal. Because of time and money constraints in the present program, a redesign of the blower and mounts was not feasible. Instead, the silicon nitride bearings were replaced with Krytox-lubricated stainless steel bearings, which have performed satisfactorily throughout this program. A view of the blower assembly installed in the discharge chamber is given in Figure 4-15.

### Magnetic Coupling

The magnetic coupling permits the blower to be driven with an external motor without the use of troublesome shaft seals. The torque necessary to drive the impeller is transmitted from a permanent-magnet driver to a permanent-magnet rotor through a hermetically sealed non-metallic partition cylinder (Figure 4-16).

Both the driven and the driver assemblies consist of 10 magnetic poles. The magnets are samarium cobalt magnets with an energy product of over 20 Megagauss-Oerstedt (Recoma Magnets). The coupling has been designed to transmit a torque of 20 N-m without slippage. At speeds between 2000 and 3000 RPM, the coupling is able to transmit several horsepower. Hence the coupling is much stronger than required for the present application. Future lasers can be equipped with a considerably smaller and cheaper coupling.

The magnetic coupling was originally designed with silicon nitride bearings and an alumina partition cylinder. For reasons outlined in the "gas blower" section above, the bearings have been replaced with Krytox-lubricated stainless steel bearings. Similarly, a Kevlar-reinforced Kynar partition cylinder has been substituted for the brazed alumina cylinder, which had fabrication problems. The thin Kynar cylinder has so far stood up very well, both under pressure loading (5 atm difference) and under full vacuum.



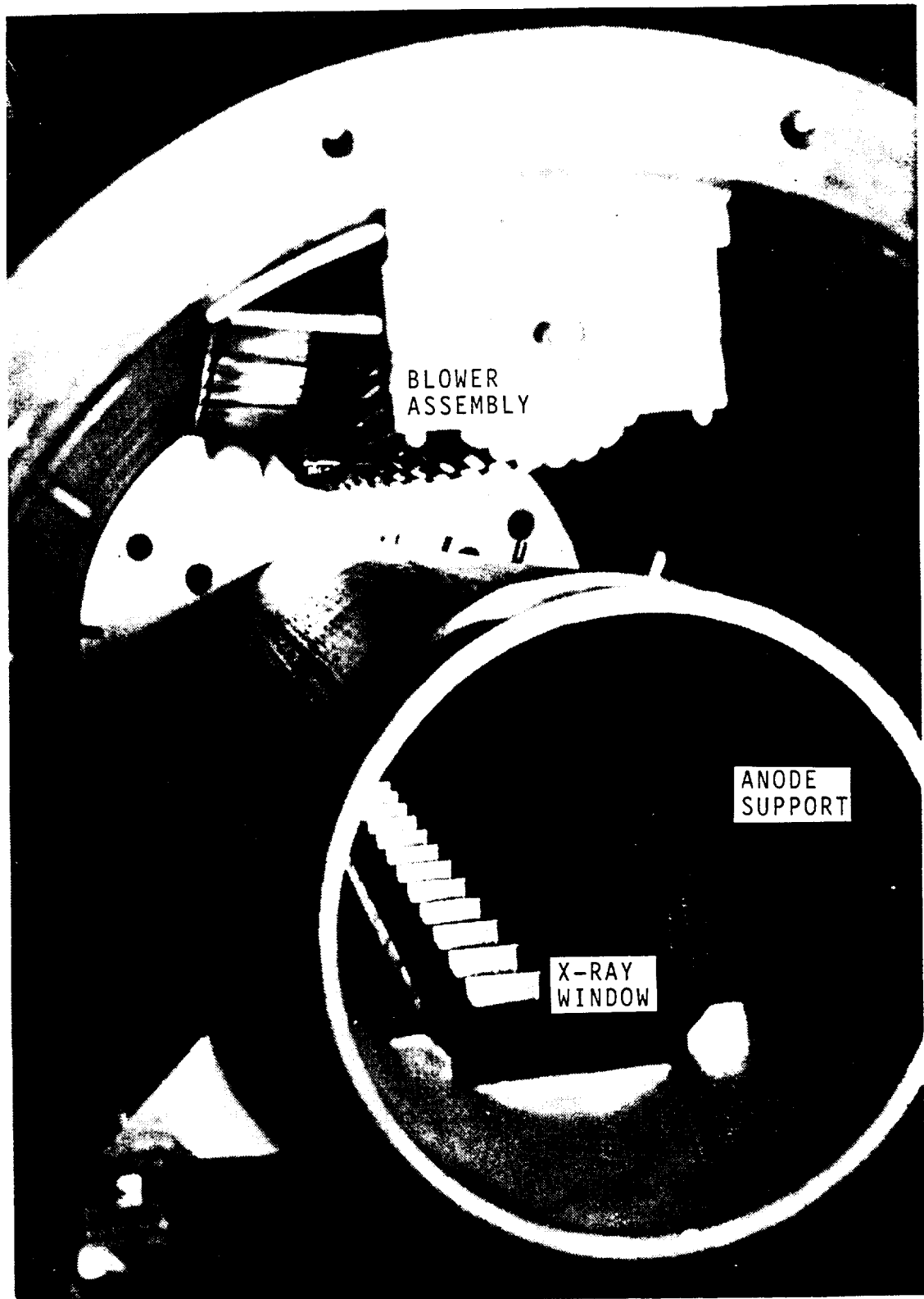


FIGURE 4-15. BLOWER INSTALLED IN DISCHARGE CHAMBER  
(NOTE SUPPORT STRUCTURE FOR X-RAY GENERATOR)

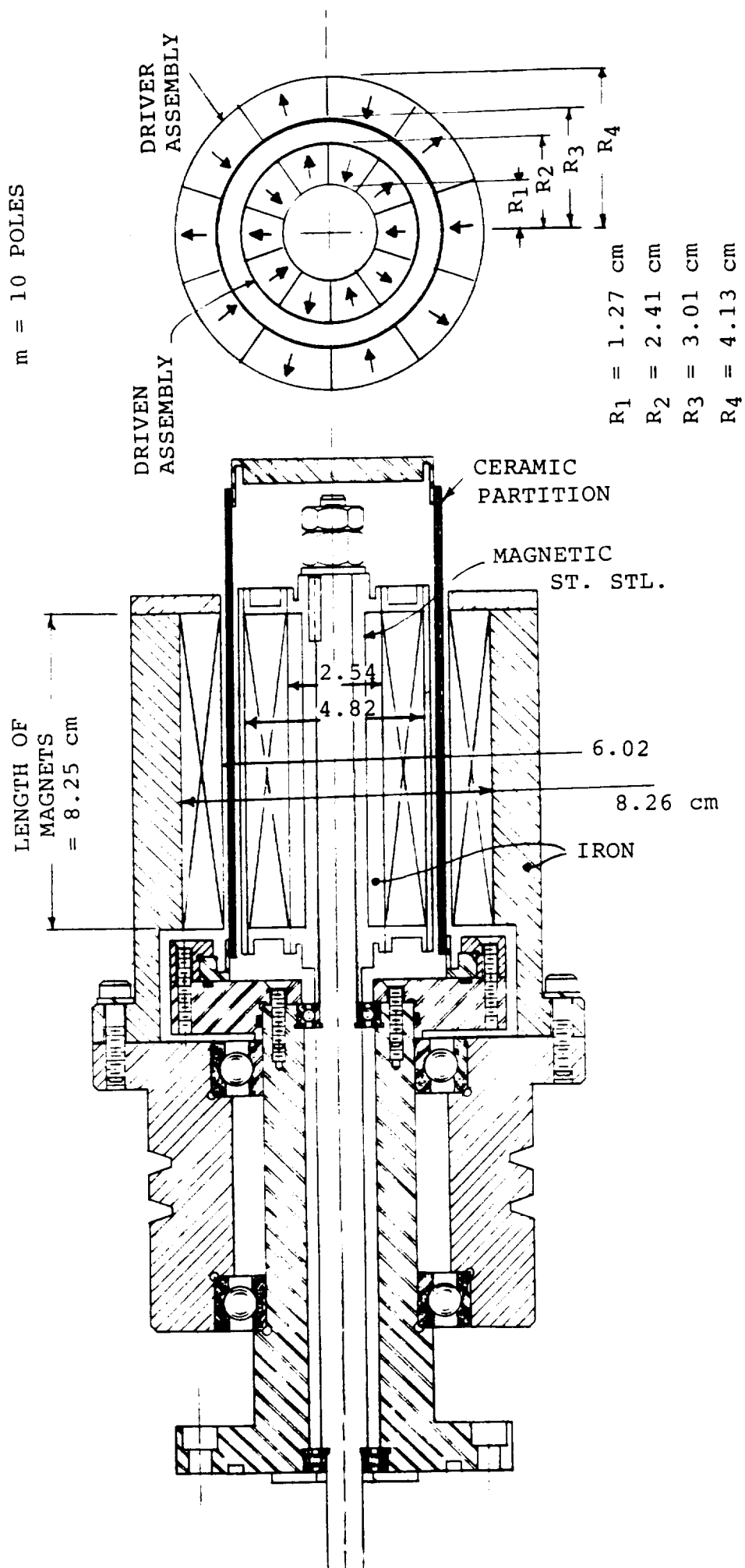


FIGURE 4-16. MAGNETIC COUPLING DESIGN

The magnetic coupling is driven by a variable-speed 1/4 HP DC electric motor via a single V-belt. The 1/4 HP motor is able to rotate the blower assembly in a 6 atm gas mixture up to 2000 RPM. A larger motor will be necessary to increase the blower speed to 3000 RPM.

The magnetic drive is connected to the blower assembly by a flexible coupling. Low-torque couplings (0.5 N-m) failed after several hours of operation. A new high-torque bellows-type coupling has stood up well for the duration of this program.

### Heat Exchangers

Two custom designed 8 kW heat exchangers have been built and installed into the laser discharge chamber (Figure 4-17). The units were constructed from 12.7 mm OD stainless steel tubing (10 per unit) and 25.4 mm diameter copper fins, which were silver brazed to the stainless tubes. After the heat exchangers were built and leak tested (by Voss Industries), the entire units were nickel coated by an electro-less nickel coating process.

Each heat exchanger unit has been built to the following specifications:

Heat exchange capacity:	8 kW
Total surface area:	9.7 m <sup>2</sup>
Nominal gas flow:	280 l/s (600 CFM)
Pressure drop at nominal gas flow:	90 P (0.32 inch H <sub>2</sub> O)
Gas inlet temperature:	39.5° C
Gas outlet temperature:	38.5° C
Water flow rate:	0.4 l/s (6 GPM)
Water inlet temperature:	15.5° C
Water outlet temperature:	20.6° C

### Gas Handling Equipment

During initial pump-out, outgassing and leak checking, the laser chamber was evacuated with a high-pump-rate cryopump, which was connected to the 7.6 cm valved pump port at the side of the discharge chamber (Figure 4-3).

Routine changing of the laser gas is performed with the aid of a pump and gas mixing station (Figure 4-18). Generally the laser gases are mixed in the discharge chamber. Partial pressures and total pressures are measured with a MKS baratron gauge and a 0 to 100 PSIG Bourdon gauge.

## 4.9 OPTICAL CAVITY

For most of the tests reported here the laser has been operated as a stable oscillator. Power has been extracted only from the main discharge cavity. The laser chamber has two 7.6 cm diameter, 1.3 cm thick quartz windows. The windows are tilted 1° off the normal to the optical axis to prevent window reflections from setting up parasitic modes. The substrates are UV-grade



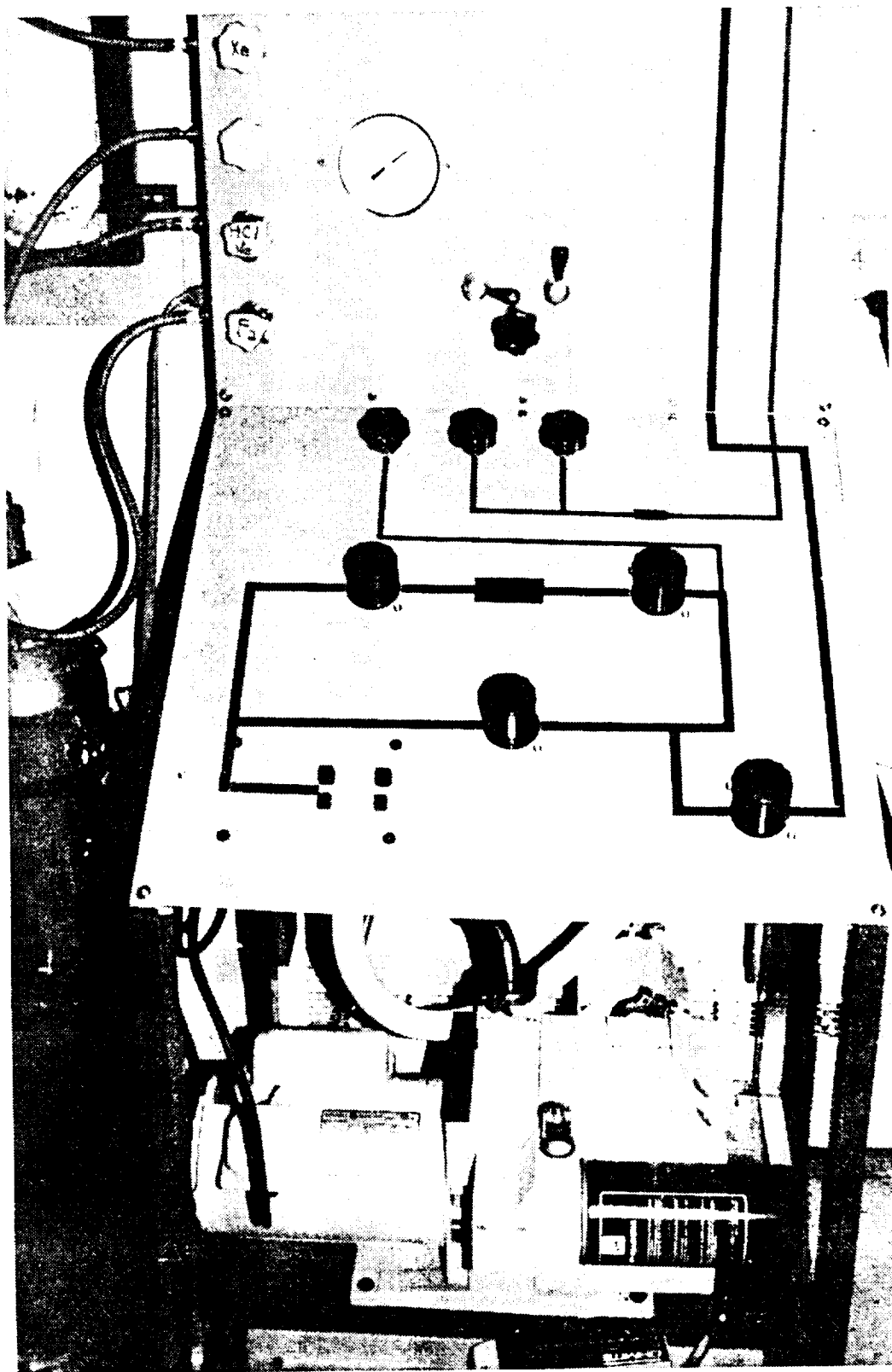


FIGURE 4-18. VACUUM PUMP AND GAS MIXING STATION

fused silica, and both faces are AR coated for 308 nm (i.e. for XeCl). Although the window mounts are equipped with annular gas flushing slits, no gas processing and laminar window flushing equipment has been installed.

Cavity reflectors and beam diagnosing equipment are supported from an optical table which has been built around the discharge chamber. The optical bench (Figure 4-3) has three adjustable legs and is supported from the concrete floor. A more "productized" version of this laser will have the optics supported from optical rails attached to the discharge chamber.

Only stable resonators with flat-flat and concave-flat configurations have been tested. Various output couplers have been used with reflectivities between 10% and 50%. A helium-neon laser has been used to align the optics.

## 5.0 PRELIMINARY EXPERIMENTS

A number of preliminary experiments were performed during the early part of the design phase to help in determining optimum design features for certain critical components. Theoretical and empirical input was required in three critical areas: the cathode insulator design, the discharge PFN configuration, and the magnetic switch design. A semi-empirical approach was used for the first task, a theoretical computer simulation for the second, and experimental testing of sample cores for the third.

### 5.1 ELECTRIC FIELD PLOTTING

A most critical issue in the design of high-energy excimer lasers (which has so far prevented scaling of discharge-excited RGH lasers to pulse energies exceeding 100 J) is concerned with surface tracking along the insulator which isolates the high-voltage electrode from ground. This insulator cannot be made arbitrarily large, because the head inductance of the discharge circuit must be kept as low as possible, so that the current risetime is substantially shorter than the stable duration of the discharge. In order to avoid high field concentrations on the insulator surfaces which may lead to tracking, a field mapping study was undertaken to determine the electric field distribution in the vicinity of the electric discharge. The study consisted of an experimental determination of the equipotential surfaces and field lines in a two-dimensional model of the electrode structure (see discharge section in Figure 4-2). The field plotting was performed in an electrolytic tray by measuring the voltage distribution caused by an AC current field.

In the simulation,  $\mathbf{E} = \nabla \phi = \mathbf{i}/\sigma$ , where  $\sigma$  is the electrical conductivity of the material. This corresponds to  $\mathbf{E} = \nabla \phi = \mathbf{D}/\epsilon$  in the electrostatic case. The technique, therefore, requires dielectric materials with permittivity  $\epsilon$  to be simulated by semiconducting materials with conductivity  $\sigma$ . The free-space permittivity  $\epsilon_0$  is represented by a copper sulfate solution of conductivity  $\sigma_0$ . Insulators, such as Kynar ( $\epsilon_r = 7$ ) are simulated by blocks of carbon filled polyester resin, mixed and cured to produce a conductivity of  $\sigma = \epsilon_r \sigma_0$  (e.g.  $7\sigma_0$  for Kynar).

To map out the equipotential lines, a 1 kHz AC signal of 20 V amplitude was applied to the aluminum blocks made in the shape of the anode and screen cathode. An AC signal was chosen to prevent electrochemical decomposition of the copper sulfate. Equipotential lines were determined by probing for points (with thin metal probes attached to a voltmeter) which have the same AC voltage (or amplitude). Electric field lines were then plotted by drawing lines which are everywhere perpendicular to the equipotential lines.

An electric field plot obtained in this fashion for the original insulator geometry is reproduced in Figure 5-1. Note the high field region (denoted by "H") at the tip of the Kynar barrier and the relatively large tangential field components along its surface (promoting breakdown by surface tracking). By curving the barrier (Figure 5-2), the field lines were made normal to the surface, and the high field at the tip was eliminated. Another high field region existed between the Kynar and the chamber wall. The field there was significantly reduced by removing some of the Kynar block and by rounding the top of the Kynar next to the wall. Eliminating these high-stress areas had the further advantage of simplifying the machining of the Kynar. For the final design, the head inductance was calculated to be 18 nH.

## 5.2 COMPUTER SIMULATION OF PULSE-FORMING NETWORKS

Extensive computer simulations of the performance of the proposed PFN resulted in circuit improvements and simplification in the design stage of the program. The calculations were performed with an Electronic Circuit Analysis program, called ECA-2.30 and purchased from Tatum Labs., Ann Arbor, Michigan. The original circuit described in the proposal was found to produce unacceptable oscillations during the charging phase. A modified version, producing good wave shapes, is shown schematically in Figure 5-3.

In the model, the gaseous electric discharge plasmas (thyatron and laser discharge) were simulated by a time-variable resistance (acting as a switch, simulating discharge development), in series with a nonlinear conductance  $G$ , which approximated the constant-voltage load characteristics of the discharge. For example, the conductance  $G_{2D}$  of the main discharge was described by an  $I, V$ -characteristic given by (see Computer Model Parts List - Table 5-1)

$$I = 2.7 \times 10^{-17} V^5.$$

Note that the circuit uses two saturable inductors,  $L_{1S}$  and  $L_{2S}$ .  $L_{1S}$  acts as a magnetic assist for the thyatron to promote long life. When it saturates, the pulse-forming line (PFL) is charged to the supply voltage in approximately 1 microsecond. The sequence of events leading to prepulse formation and discharge initiation are best followed by monitoring the voltage appearing on the secondary cathode  $K_2$  as a function of time (Figures 5-5 and 5-6).

During the pulse charging phase, after  $L_{1S}$  saturates, the voltage at  $K_2$  follows closely the sinusoidally rising negative voltage on  $K_1$  (Figure 5-5). During this same period, the current experienced by the thyatron reaches a peak value of 10 kA (Figure 5-4). At the end of the charging period,  $L_{1S}$  reverts to its high-impedance state (unsaturated core) and acts as a diode,

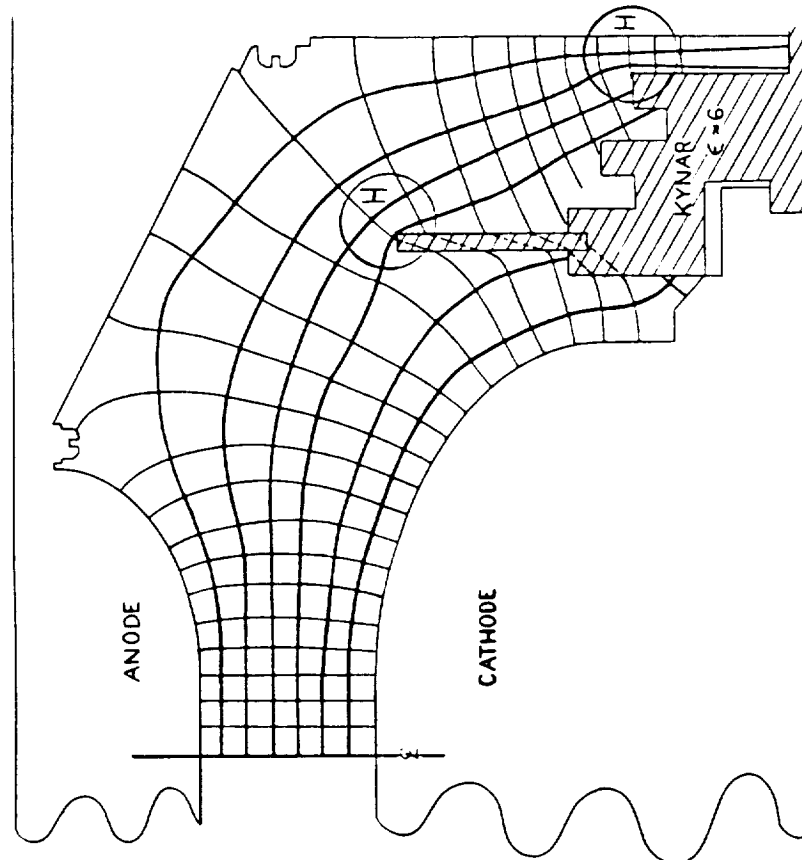


FIGURE 5-1. ELECTRIC FIELD PLOT IN DISCHARGE SECTION FOR ORIGINAL GEOMETRY. "H" DENOTES HIGH-STRESS REGIONS

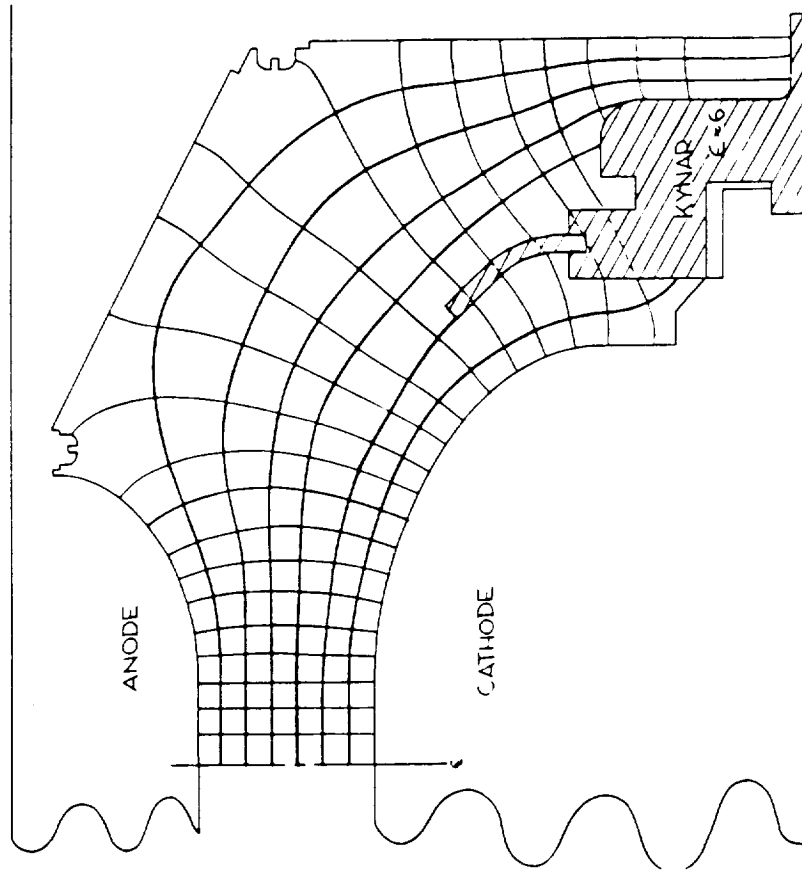


FIGURE 5-2. ELECTRIC FIELD PLOT IN DISCHARGE SECTION WITH MODIFIED KYNAR INSULATOR, REMOVING HIGH-STRESS POINTS



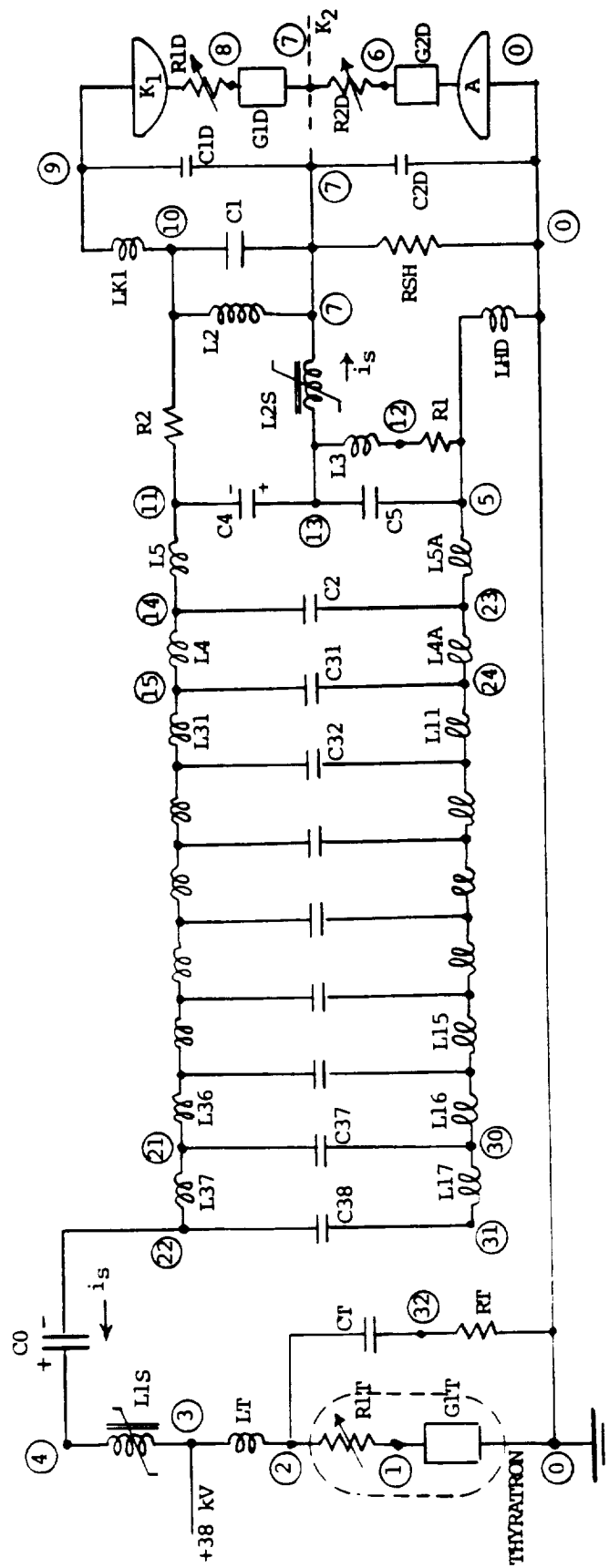


FIGURE 5-3. MODEL OF PFN, ORIGINAL VERSION WITH MAGNETICALLY SWITCHED POSITIVE PULSE

EXCIMER CIRCUIT 3C (EDC 8A)					
1	G1T	1	0	1.u	E 5.
2	+			0.002	
3	RG1	1	0	5.	
4	R1T	2	1	1.G	
5	+			0.002	.. S 0.
6	LT	3	2	50.n	
7	CO	4	22	170.n	V 38.K
8	L1S	4	3	250.u	I 0.
9	+			-200.u	B 30.
10	+			-35.u	B 50.
11	+			-10.u	B 100.
12	+			-3.5u	B 300.
13	+			-600.n	B 1.K
14	+			-200.u	Z-30.
15	+			-35.u	Z-50.
16	+			-10.u	Z-100.
17	+			-3.5u	Z-300.
18	+			-600.n	Z-1.K
19	LHD	5	0	18.n	
20	G2D	6	0	27.E-18	E 5.
21	+			0.005	
22	G22D	0	6	27.E-18	E 5.
23	+			0.005	
24	R2D	7	6	10.M	
25	+			10.	S 1.26u
26	+			0.5	S 1.268u
27	+			0.001	S 1.276u
28	G1D	8	7	40.E-15	E 5.
29	+			0.01	
30	G11D	7	8	40.E-15	E 5.
31	+			0.01	
32	R1D	9	8	10.M	
33	+			0.01	S 1.24u
34	C2D	7	0	100.p	V 0.
35	C1D	9	7	300.p	V 0.
36	RSH	7	0	5.K	
37	LK1	10	9	5.n	
38	L2	10	7	10.u	
39	C1	10	7	3.n	.. V 0.
40	R2	11	10	0.02	
41	C4	11	13	6.n	.. V 0.
42	C5	13	5	6.n	.. V 0.
43	L2S	13	7	125.u	.. I 0.
44	+			-100.u	B 80.
45	+			-20.u	B 170.
46	+			-3.u	B 400.
47	+			-1.u	B 600.
48	+			-500.n	B 1.K
49	+			-100.u	Z-80.
50	+			-20.u	Z-170.
51	+			-3.u	Z-400.
52	+			-1.u	Z-600.
53	+			-500.n	Z-1.K
54	L3	13	12	3.u	
55	R1	12	5	3.	
56	L5	14	11	1.5n	
57	L4	15	14	1.5n	
58	C2	14	23	6.n	.. V 0.
59	C31	15	24	15.n	.. V 0.
60	C32	16	25	15.n	.. V 0.
61	C33	17	26	15.n	.. V 0.
62	C34	18	27	15.n	.. V 0.
63	C35	19	28	15.n	.. V 0.
64	C36	20	29	15.n	.. V 0.
65	C37	21	30	15.n	.. V 0.
66	C38	22	31	15.n	.. V 0.
67	L31	16	15	1.6n	
68	L32	17	16	1.6n	
69	L33	18	17	1.6n	
70	L34	19	18	1.6n	
71	L35	20	19	1.6n	
72	L36	21	20	1.6n	
73	L37	22	21	1.6n	
74	L5A	5	23	1.5n	
75	L4A	23	24	1.5n	
76	L11	24	25	1.6n	
77	L12	25	26	1.6n	
78	L13	26	27	1.6n	
79	L14	27	28	1.6n	
80	L15	28	29	1.6n	
81	L16	29	30	1.6n	
82	L17	30	31	1.6n	
83	CT	2	32	2.5n	.. V 38.K
84	RT	32	0	160.	

TABLE 5-1. COMPUTER MODEL PARTS LIST FOR LASER DISCHARGE PFN

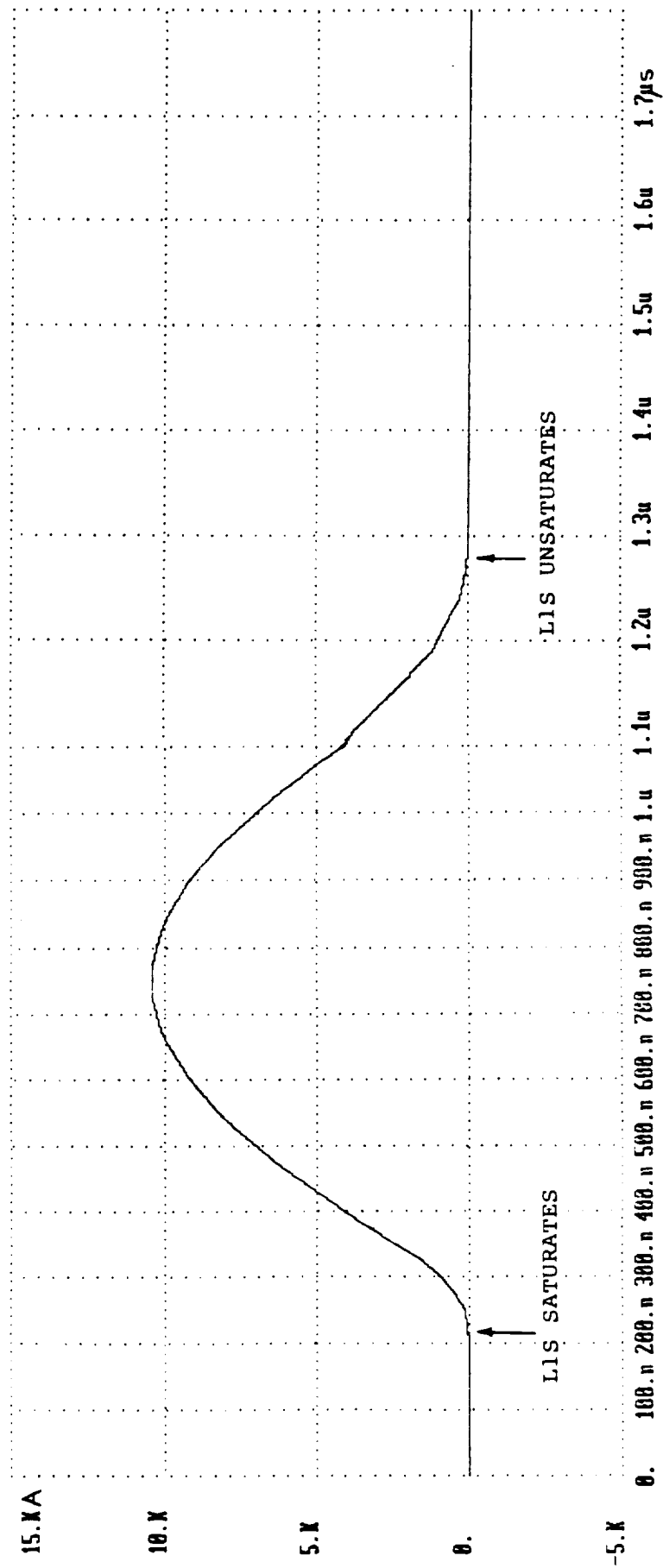


FIGURE 5-4. CHARGING CURRENT THROUGH THYRATRON (COMPUTER MODELING)

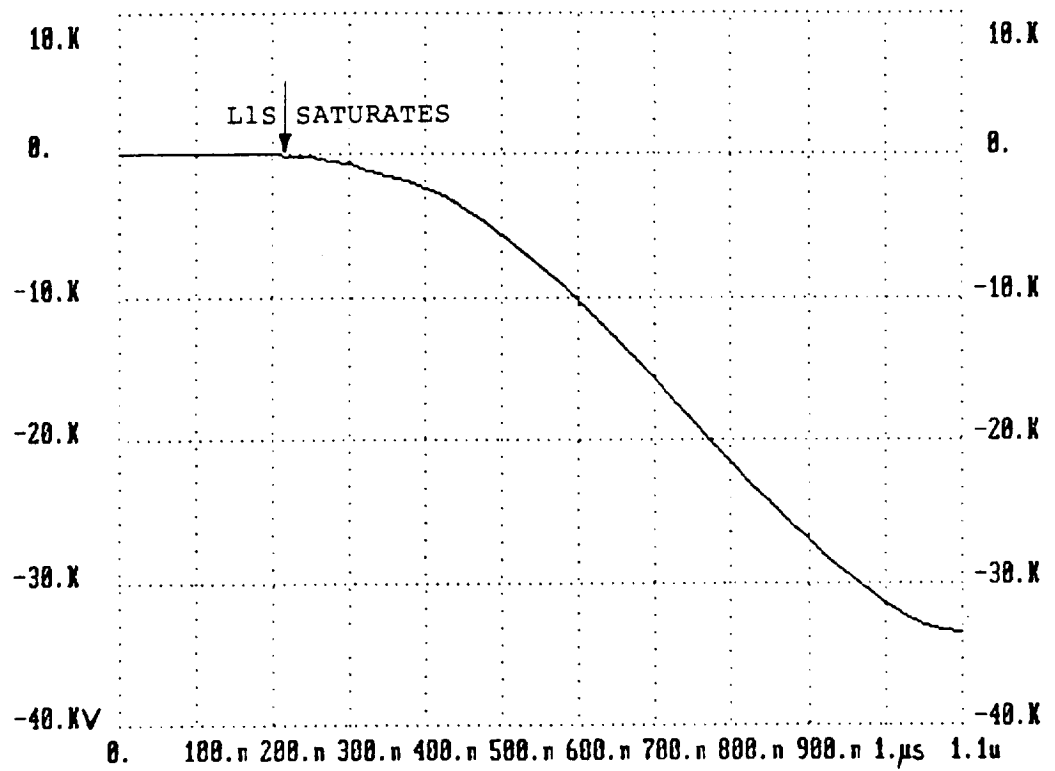


FIGURE 5-5. VOLTAGE AT SCREEN (NODE 7) DURING CHARGING PULSE (COMPUTER MODELING)

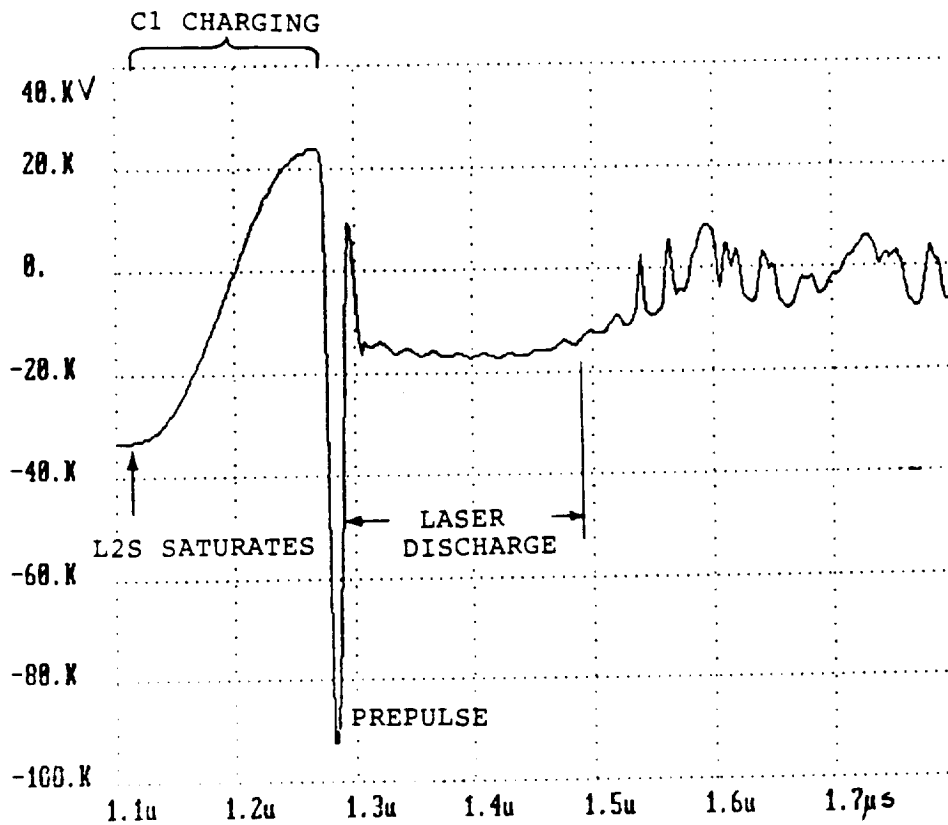


FIGURE 5-6  
PREPULSE AND DISCHARGE  
VOLTAGE AT SCREEN  
(COMPUTER MODELING)

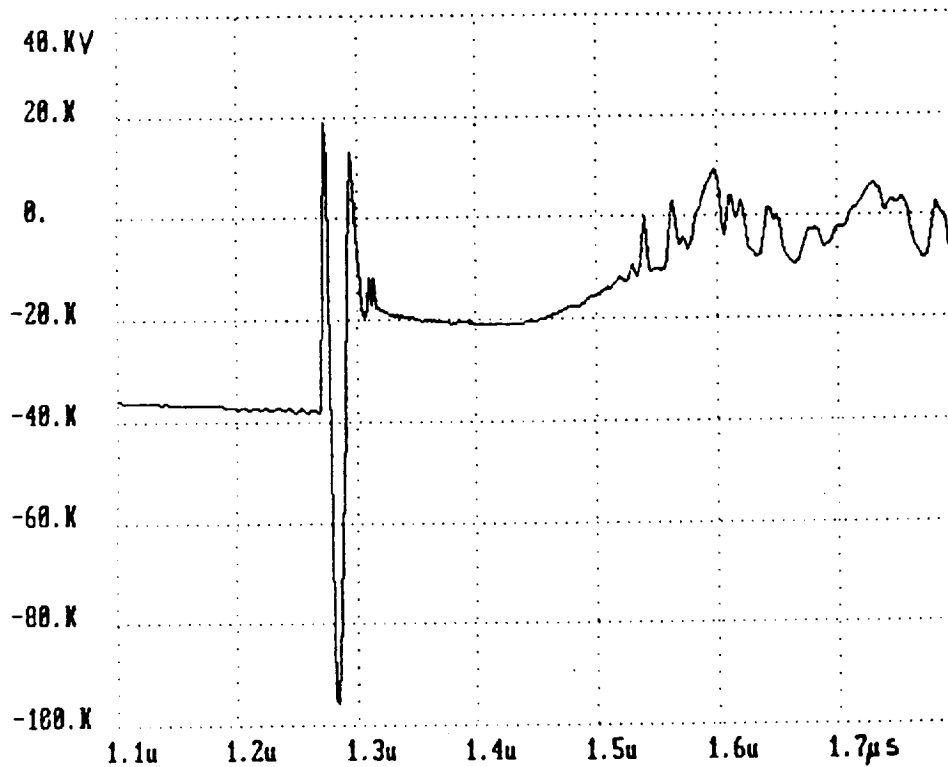


FIGURE 5-7  
PREPULSE AND DISCHARGE  
VOLTAGE AT CATHODE  
(COMPUTER MODELING)

preventing the thyatron current from going negative. When L2S saturates, capacitor C1 is rapidly charged from C4, producing a high voltage between K1 and K2 (predischage gap), rapidly initiating the predischage. The closely coupled capacitors C1, in combination with the underdamped resistance of the highly overvolted predischage, then results in C1 ringing through the predischage gap, producing a negative prepulse of nearly 100 kV across the main discharge gap (between screen and grounded anode). This prepulse initiates the laser discharge. A steady-state discharge voltage of approximately 18 kV is then maintained for 150 ns. The voltage appearing on the cathode, K1 (Figure 5-7), is very similar to the voltage pulse on the screen, except for the L2S-induced positive voltage excursion, which is only seen on the screen.

It should be noted that in the computer simulation the main discharge is artificially induced by letting the discharge resistance R2D rapidly go to a low value. In practice, the prepulse amplitude was much less than predicted, and the prepulse was not wide enough for the main discharge to ignite completely. These difficulties, experienced with the actual circuit, are discussed in more detail in Section 6.1.

The calculated power dissipated in the main discharge (Figure 5-8) reaches 600 MW, close to the design value. The oscillations seen in the power curve (and also in the discharge current) were at first believed to be due to the fact that the PFL was constructed from discrete capacitors. However, further investigation showed this to be untrue. The oscillations are caused by ringing in the LC-circuit dominated by the head inductance and the stray electrode capacitance.

Whereas only the results of computer modeling of the first PFN are presented in this section, the ECA program has proven invaluable for modeling the later, more successful, versions of the PFN. The B-H characteristics of the saturable core reactors were approximated by a simple S-curve going through the origin (i.e. saturation effects were accounted for, but hysteresis losses were ignored). The non-linearities in the B-H curves were modeled by letting the inductance decrease in a stepwise fashion as the current increased. This stepwise change in L has occasionally caused non-convergences in the integration of the set of differential and integral equations used to describe the circuit. The ECA program has a built-in recovery program which in most cases can successfully sidestep these non-convergences, however.

The ECA program has also been successfully applied to model the X-ray pulser (see also Section 4.6). Figure 5-9 shows the equivalent circuit used for calculation purposes. Table 5-2 lists the component values and initial conditions. The e-gun diode (anode-cathode) impedance and stray capacitance have been represented here by  $R_D$  and  $C_S$ , the cathode capacitance and contact resistance (corona plasma impedance) by  $C_C$  and  $R_C$ . The thyatron has been modeled by the non-linear resistance and conductance,  $R_T$  and  $G_T$ , in series with the tube inductance  $L_T$ . The component values of the PFN, made up of capacitors  $C_1$  to  $C_6$  and inductors  $L_1$  to  $L_5$ , have been tailored to give the most rectangular anode pulse of 250 ns duration. The pulse transformer has been represented by an ideal transformer with a gain of 4:1. The non-ideal characteristics of the transformer have been taken care of by equivalent

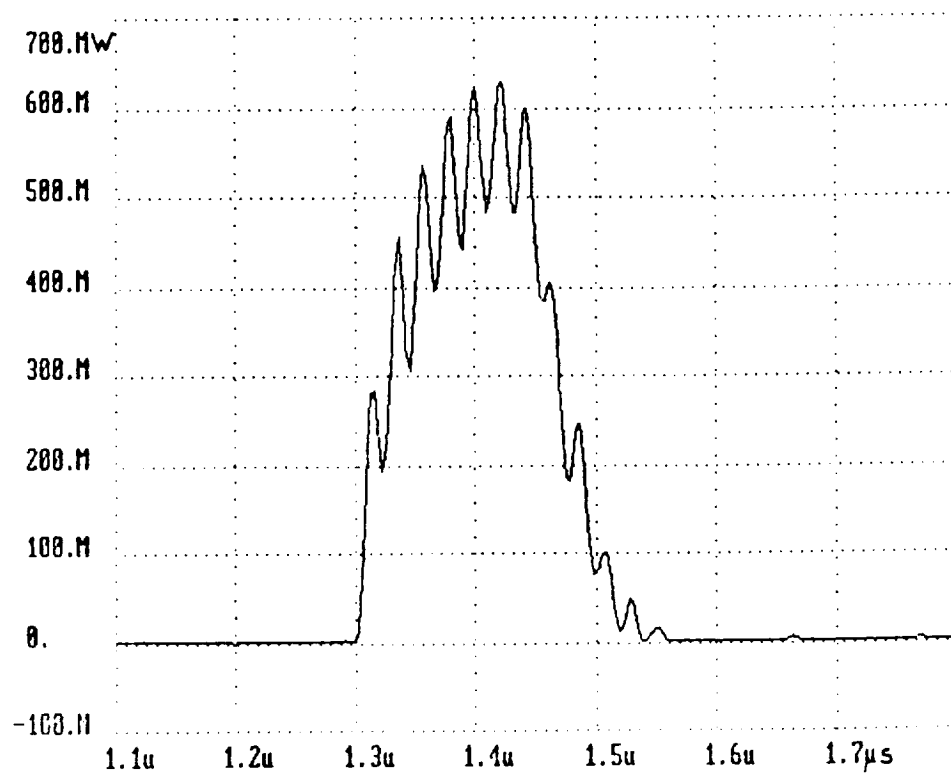


FIGURE 5-8. POWER DISSIPATED IN MAIN DISCHARGE GAP (COMPUTER MODELING)

circuit components, such as the leakage inductance  $L_L$ , the primary magnetizing inductance  $L_p$ , the winding resistance  $R_W$ , the eddy current core losses  $R_p$ , and the interwinding capacitance  $C_{EQ}$ . Values used for  $L_L$ ,  $L_p$  and  $R_W$  were obtained experimentally by analysing the completed pulse transformer with an impedance bridge. The equivalent capacitance  $C_{EQ}$  has been calculated from the measured primary-secondary capacitance  $C_{PS}$ , using the expression

$$C_{EQ} = (n^2 - n + 1) C_{PS}/3, \quad \text{where } n = 4 \text{ (step-up ratio).}$$

Figure 5-10 gives the anode voltage pulse calculated for two different diode impedances,  $R_D = 750$  ohms and  $R_D = 375$  ohms. Modeling results have shown a significant degradation of the anode pulse if the diode impedance becomes less than 200 ohms. Calculated diode impedance, based on the Child-Langmuir law and the electrode geometry, is 650 ohms.

The Child-Langmuir law states that the e-beam current density is given by

$$j_b = K V_b^{3/2} / s^2,$$

where  $V_b$  is the e-beam current density,  $s$  is the anode-cathode spacing, and the constant  $K$  is approximately  $10^{-6}$  ampere-volt $^{-3/2}$  for typical e-gun geometries. In practice,  $s$  is a function of time as the cathode plasma (acting as a virtual cathode) rapidly expands toward the anode with velocities,  $u_p$ , exceeding  $10^6$  cm/s. Hence, to a first approximation, the anode-cathode spacing varies with time as

$$s(t) = s_0 - u_p t.$$

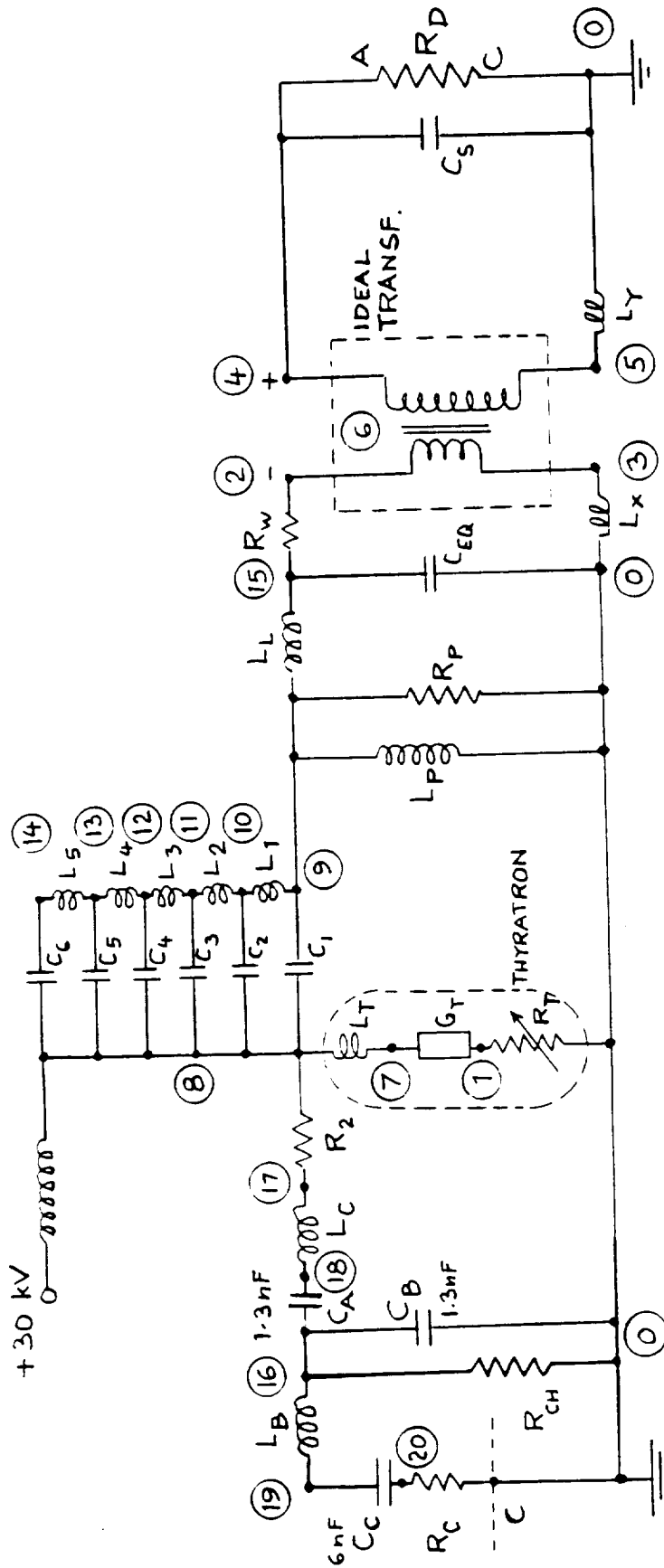
The time varying diode impedance is then given by

$$R_D = (s_0 - u_p t)^2 / AK V_b^{1/2}(t),$$

where  $A$  is the area of the advancing plasma front.  $V_b$  is a function of time, because the circuit responds to the decreasing diode impedance with a decreased output voltage (Figure 5-10). Taking this time-dependent behavior of the e-gun characteristics into account, the actual measured anode pulse (Figure 4-14) is in good agreement with the pulse predicted by the model.

The cathode pulse is generated simultaneously with the anode pulse by transferring the voltage on capacitor  $C_A$  to the cathode capacitance  $C_C$  when the thyatron fires. The values of  $L_C$ ,  $R_2$  and  $C_B$  have been adjusted, so as to give a high value of  $dV/dt$  at the cathode at the same time the anode voltage is at a maximum. This assures good synchronicity between the time of most efficient corona formation and the time at which the accelerating field is at a maximum.





$$C_{EQ} = (n^2 - n + 1) C_{PS} / 3$$

$$n = 4$$

$$C_{PS} = 370 \text{ pF}$$

FIGURE 5-9. COMPUTER MODEL OF X-RAY PULSER

TABLE 5-2

## PARTS LIST FOR X-RAY PULSER MODEL

XRAY PULSER					
1	RT	1	0	10.K	
2	+			0.01	
3	G1T	7	1	1.u	..
4	+			0.002	E 5.
5	G11T	1	7	0.05	
6	LT	8	7	100.n	
7	C1	8	9	2.n	..
8	C2	8	10	1.3n	..
9	C3	8	11	1.3n	..
10	C4	8	12	2.n	..
11	C5	8	13	3.3n	..
12	C6	8	14	4.n	..
13	L1	9	10	500.n	
14	L2	10	11	300.n	
15	L3	11	12	500.n	
16	L4	12	13	300.n	
17	L5	13	14	300.n	
18	LL	15	9	2.45u	
19	RW	2	15	0.03	
20	CEQ	15	0	1.62n	..
21	RP	9	0	5.3K	
22	LP	9	0	400.u	
23	LX	3	0	100.n	
24	LY	5	0	100.n	
25	RD	4	0	750.	
26	CS	4	0	50.p	..
27	GT1	2	0	1.	
28	GT2	2	6	-1.	
29	GT3	3	0	-1.	
30	GT4	3	6	1.	
31	GT5	4	0	0.25	
32	GT6	4	6	-0.25	
33	GT7	5	0	-0.25	
34	GT8	5	6	0.25	
35	R2	8	17	60.	
36	LC	17	18	30.u	
37	CA	18	16	1.3n	..
38	CB	16	0	1.3n	..
39	LB	16	19	10.u	
41	RCH	16	0	100.	
42	CC	19	20	6.n	..
43	RC	20	0	25.	

S 0.

V 30.K

V 30.K

V 30.K

V 30.K

V 30.K

V 30.K

V 0.

V 0.

V 30.K

V 0.

V 0.

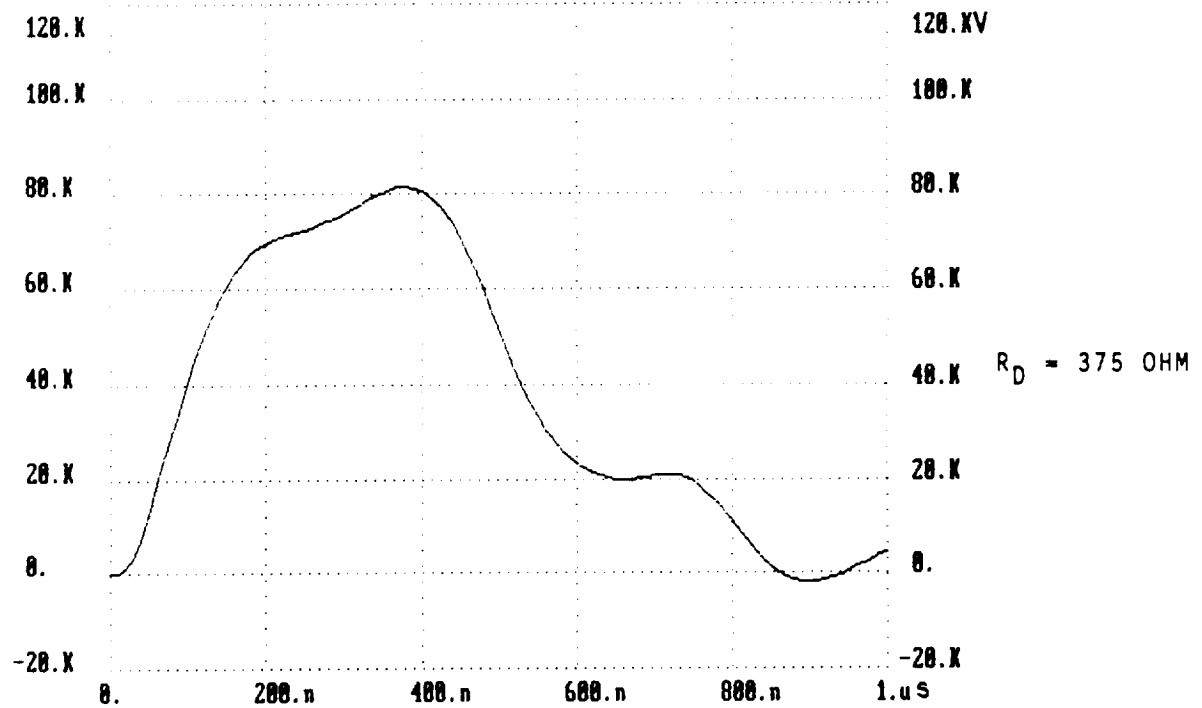
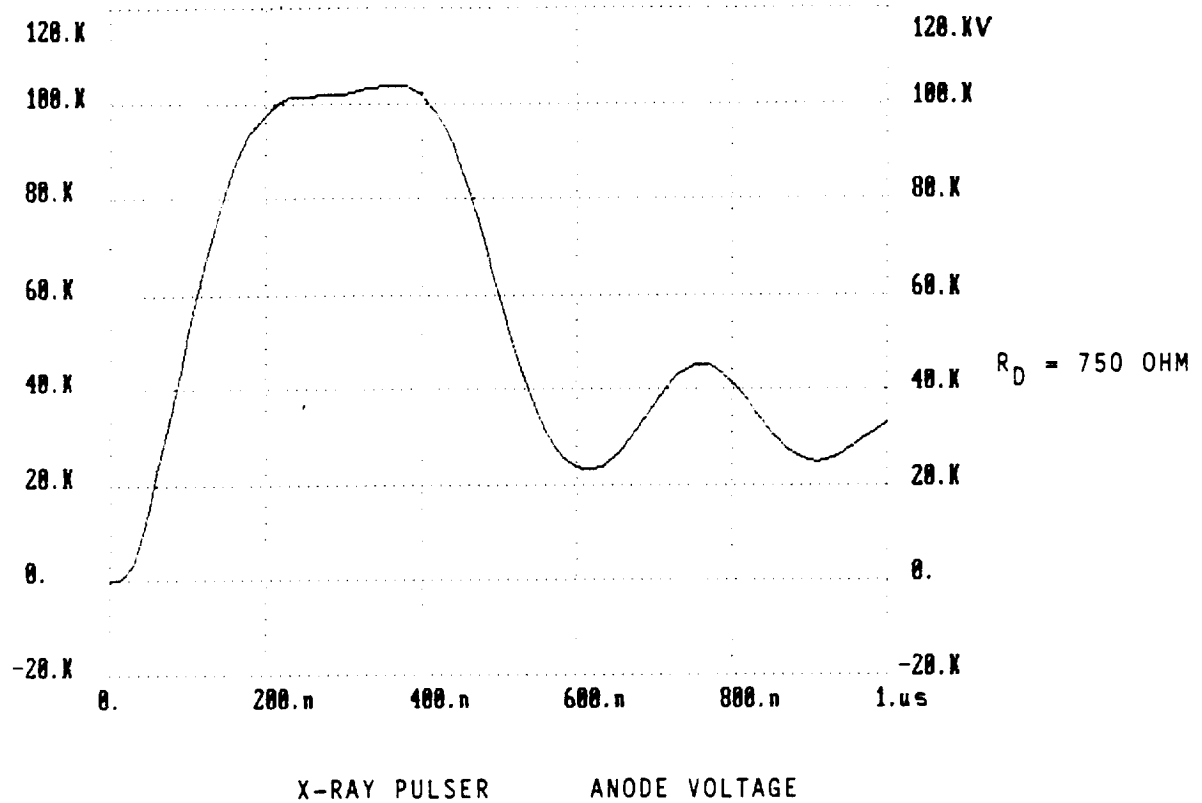


FIGURE 5-10. CALCULATED E-BEAM ANODE VOLTAGE PULSES  
FOR TWO DIFFERENT DIODE IMPEDANCES ( $R_D$ )

### 5.3 TESTING OF SAMPLE METGLAS CORES

Requirements for the magnetic switches L1S and L2S (see Figures 4-1 and 5-3) are that their  $V \cdot t$ -products are on the order of  $10^{-2}$  V-s. Only cores wound from thin Metglas (TM Allied Signal) ribbon, less than 25 micrometers thick, have both the high frequency response and, simultaneously, the high values of the saturated magnetic flux density ( $B_m$ ), necessary for the present application. Whereas high-frequency (microwave) ferrites may have equal or better high-frequency response, their saturated magnetic induction is generally more than an order of magnitude below that of Metglas. Hence, a saturable inductor made from ferritic material would require a core volume ten times as large as an equivalent Metglas inductor.

Early in the program, two sample Metglas cores, made by Allied Signal Corporation's Metglas Division, were tested to verify their magnetic properties. Tests were performed to establish the " $V \cdot t$ -product to saturation" and the effective permeability of these cores when excited by a microsecond high-voltage pulse. The cores had been wound into a racetrack geometry, with an oval window measuring approximately 4 cm by 14 cm, using pre-annealed 5 cm wide Metglas ribbon. Thin Mylar tape (6 microns thick) was wound onto the Plexiglass mandrel together with the Metglas ribbon, to isolate and separate the Metglas layers from each other. This was necessary to allow the magnetic field to diffuse into the Metglas more rapidly, giving the core the necessary high-frequency characteristics.

One core was made from 15  $\mu$ m thick 2605-CO material, the other from 25  $\mu$ m thick 2705-MN ribbon. The cross-sectional areas of these cores consisted of approximately 6 cm<sup>2</sup> of metal. Measured B-H curves for these cores are reproduced in Figures 5-11 and 5-12. These curves were obtained with low-frequency, quasi-DC excitation signals and are not necessarily representative of the dynamic response under high-frequency service. Core responses to fast excitation pulses (i.e. for high values of dB/dt), have been studied extensively by Smith<sup>26</sup>, (Allied Signal scientist) and have been published in the "pulsed power technology" literature.

When designing a saturable core magnetic switch, the first consideration is the hold-off period required before the current is allowed to increase. The time to saturation is expressed by the voltage integral of the voltage pulse applied to the winding on the saturable core, i.e. by  $\int V dt$ . The core cross-sectional area which is consistent with the required  $V \cdot t$  hold-off integral is given by

$$A = \int V dt / N \Delta B,$$

where  $N$  is the number of electrical turns wound on the core and  $\Delta B$  is the available excursion of the magnetic flux density,

$$\Delta B = B_r + B_m,$$

where  $B_r$  is the magnetic flux density at the remanence point (see B-H loops).

The unsaturated inductance of the magnetic reactor can be calculated by the usual equation

$$L_u = \mu_{sw} N^2 A / l_m,$$

where  $l_m$  is the magnetic path length, and  $\mu_{sw}$ , as given by the magnetic saturation wave theory<sup>26</sup> is

$$\mu_{sw} = 8 \rho B_m d^{-2} (dB/dt)^{-1}.$$

Here,  $\rho$  is the electrical resistivity of the core material and  $d$  is the thickness of the Metglas ribbon. The time rate of change of the magnetic flux can be estimated from

$$dB/dt = V_{peak} \Delta B / \int V dt.$$

The saturated inductance of the magnetic reactor is calculated from the normal air coil formulae.

Referring now back to Figures 5-11 and 5-12, note that the MN material has a very rectangular, low loss hysteresis loop, but has a lower saturated magnetic induction of 1.1 Tesla, as compared with 1.6 T for the CO material. The transition from high permeability to low permeability at the remanence points (knees of the B-H loop) is normally more "square" for the CO material. The degradation at the "knees" has been caused by mechanical stresses introduced when the Metglas ribbon was rewound onto an oval mandrel after having been annealed in a toroidal configuration.

To test these cores under representative conditions, ten electrical turns were wound around each core, and the completed saturable inductor was then connected into a test circuit shown schematically in Figure 5-13. A 133 nF capacitor, charged to voltages between 0.4 and 20 kV from a switched charging supply, was then discharged through the magnetic inductor by means of a triggered thyatron switch. The voltage across the inductor and the current through the inductor were monitored by suitable probes. The circuit inductance, other than the magnetic reactor inductance, was kept to less than a microhenry, and the load resistance was kept to 0.3 ohm to keep the test circuit well underdamped. The measured "air inductance" of the ten-turn coil was 7  $\mu$ H.

Figures 5-14 to 5-17 show the voltage and current traces obtained when the capacitor was charged to 1.5 kV. The MN core saturated after 8  $\mu$ s, the CO core after 12  $\mu$ s (Figures 5-14 and 5-16), indicating that the cores were fully reset to the  $-B_r$  condition by the capacitor charging current. Because the permeability at remanence ( $H = 0$ ,  $B = B_r$ ) is very small (near-horizontal slope of the B-H curve), there resulted a current leakage pulse at  $t = 0$  (Figures 5-15 and 5-17), which was more pronounced for the MN core than for the CO core. Similar and self-consistent results were obtained at other charging voltages. The saturated inductance of the inductor was calculated from the width,  $T_i$ , of the current pulse and

$$(C L_{SAT})^{1/2} = T_i.$$

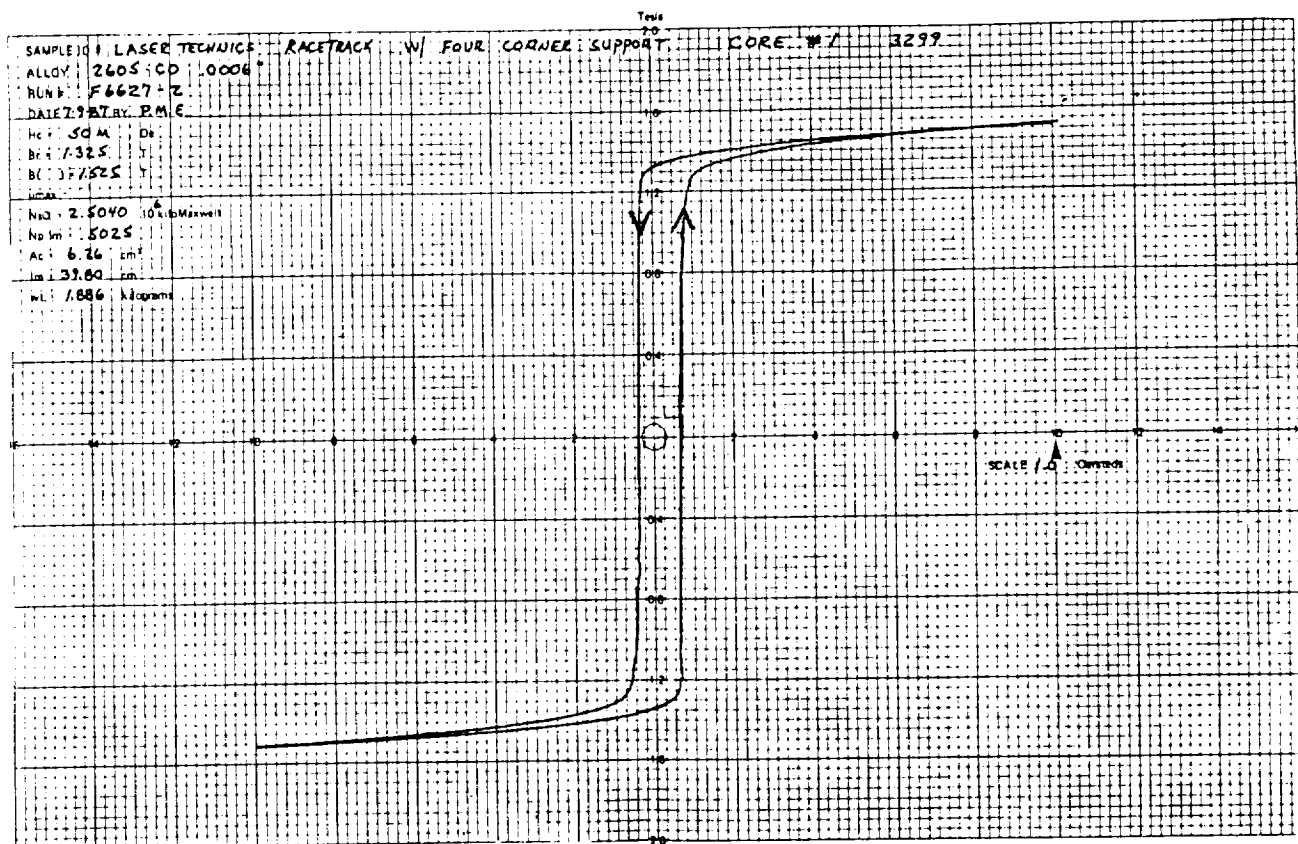


FIGURE 5-11. B-H CURVE FOR RACETRACK CORE WOUND FROM 15  $\mu$ m THICK BY 5 cm WIDE 2605-CO METGLAS RIBBON

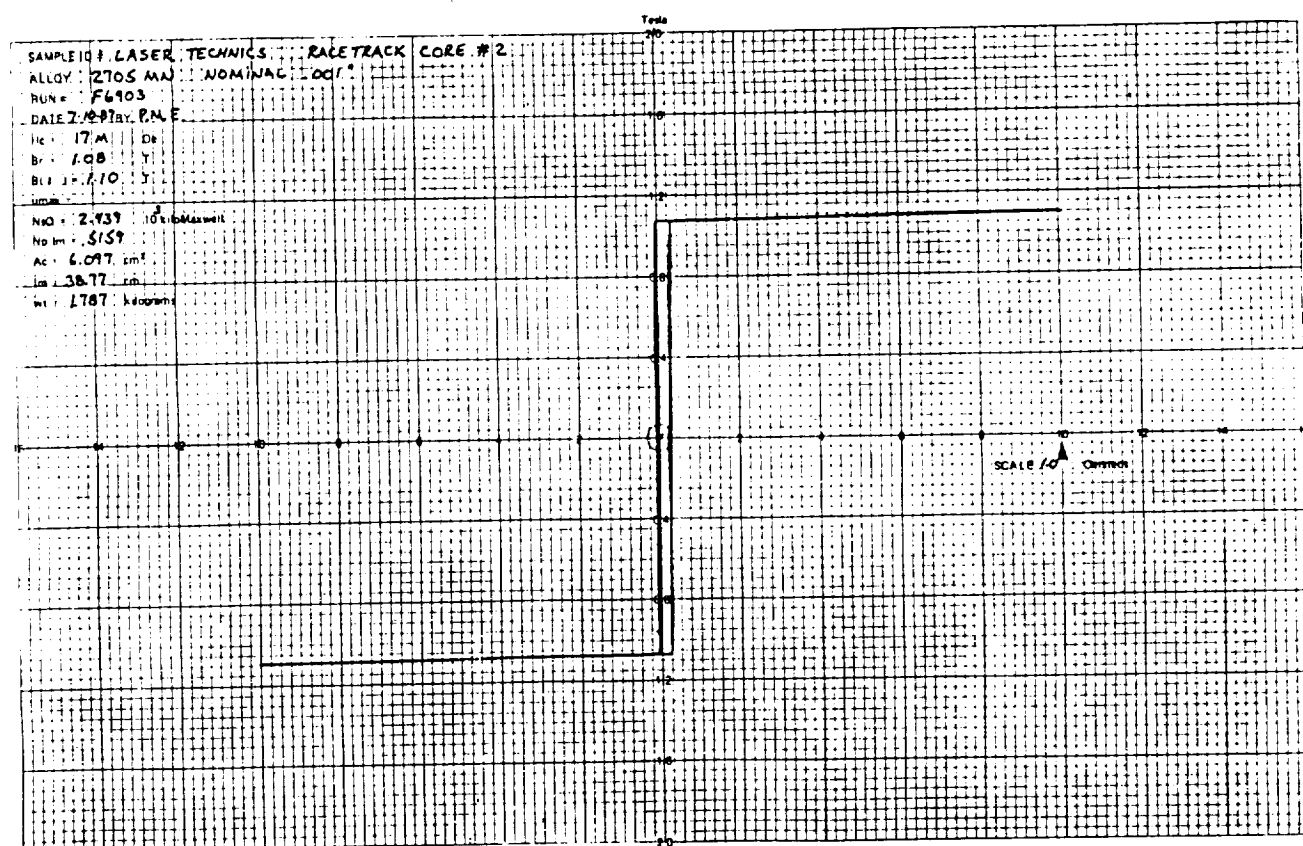


FIGURE 5-12. B-H CURVE FOR RACETRACK CORE WOUND FROM 25  $\mu$ m THICK BY 5 cm WIDE 2705-MN METGLAS RIBBON

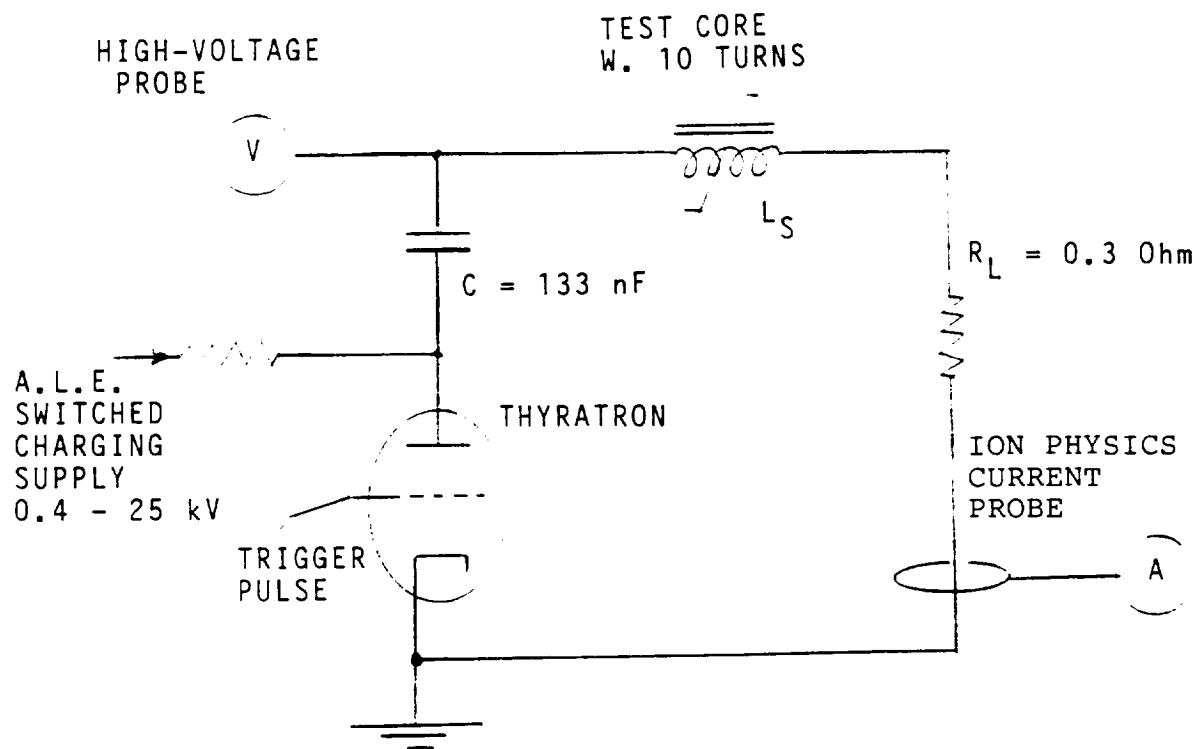


FIGURE 5-13. EXPERIMENTAL SETUP FOR TESTING METGLAS CORES

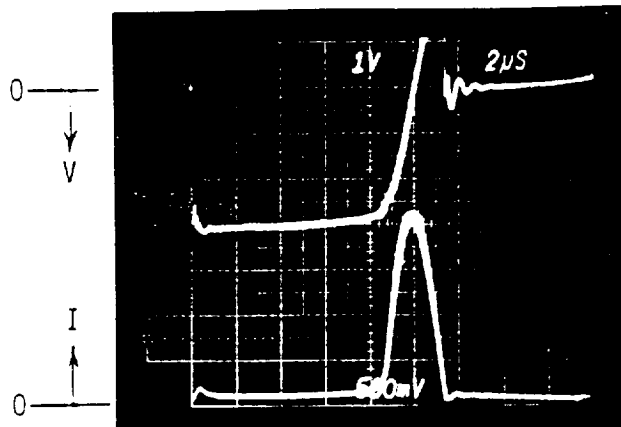


FIGURE 5-14.

VOLTAGE (500V/DIV) AND  
CURRENT (50 A/DIV) FOR  
2705-MN CORE.  $V.t = 12 \text{ mV s}$

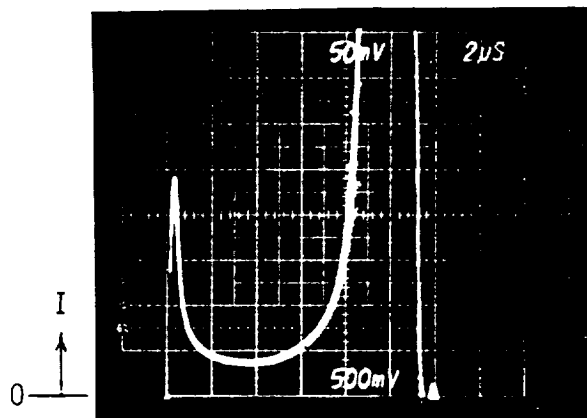


FIGURE 5-15.

MAGNIFIED CURRENT (2.5 A/DIV)  
PULSE FOR 2705-MN CORE. NOTE  
INITIAL LEAKAGE CURRENT.

CHARGING VOLTAGE FOR FIGURES 5-14 TO 5-17 WAS 1.5 kV.  
TIME SCALE IS 2 MICROSECONDS PER DIVISION.

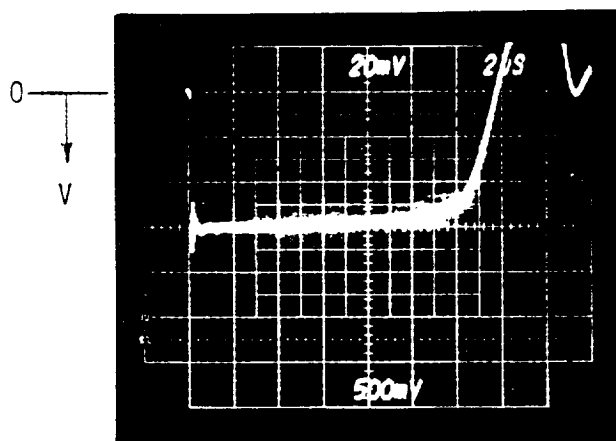


FIGURE 5-16.

VOLTAGE (500 V/DIV) PULSE  
FOR 2605-CO CORE  
 $V.t = 18 \text{ mV s}$

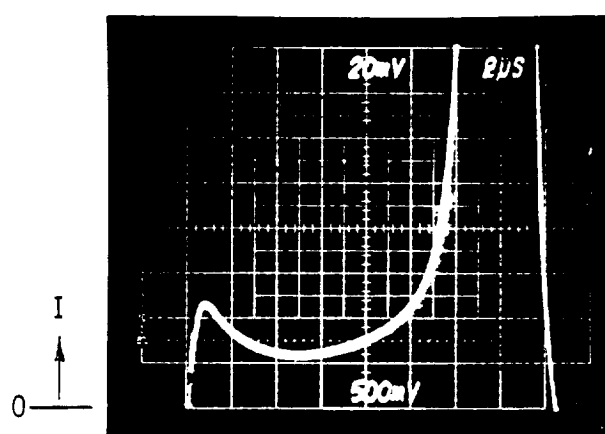


FIGURE 5-17.

MAGNIFIED CURRENT (2.0 A/DIV)  
PULSE FOR 2605-CO CORE. NOTE  
LOWER LEAKAGE CURRENT



The unsaturated inductance,  $L_{US}$ , was estimated from the rate of current rise before saturation, after the effects of the decaying leakage pulse were subtracted out. The current in a highly underdamped circuit ( $L/C \gg R^2$ ) is

$$I = V_0 (C/L)^{1/2} e^{-tR/2L} \sin(t L^{-1/2} C^{-1/2}),$$

which for small times ( $t \ll (LC)^{1/2} \ll L/R$ ) reduces to

$$I = V_0 (C/L)^{1/2} \sin( ) = V_{CH} t / L_{US}.$$

The results from these tests were as follows:

1. The cores appeared to be fully reset to the opposite remanence condition during charging of the capacitor from the pulsed charging supply (approximately 10 A-turns peak) for all charging voltages above 350 V.
2. The measured  $V \cdot t$  integrals were  $18 \times 10^{-3}$  V-s (or 1.8 mV-s/turn) for the 2605-CO core and  $12 \times 10^{-3}$  V-s (or 1.2 mV-s/turn) for the 2705-MN core. This corresponds to a delta B swing of 3.0 T for the CO material and of 2.0 T for the MN material.
3. The current leakage at  $t_0$  was approximately 5% of the peak current for the MN core and approximately 1.5% for the CO core.
4. The unsaturated inductance of the 2605-CO core was estimated to be 3.0 mH and that of the 2705-MN core as 2.6 mH. These numbers correspond to relative permeabilities of 16,000 and 13,000, respectively.
5. Current pulse widths indicated that the saturated relative permeabilities were close to unity, certainly less than 2.
6. Tests also showed that after saturation, any opposite voltage swings did not produce any appreciable currents in the opposite direction (diode behavior).

Whereas either core material would have proven satisfactory for the intended application, we chose to go with the thin 2605-CO material for the following reasons:

1. Because of its higher available delta B, the number of electrical turns could be reduced, resulting in a lower saturated inductance. Alternatively, the mass of the core could be reduced for the same number of turns.
2. The initial leakage current was less for the CO material.
3. The 15 micron thin ribbon blocks high frequency ( $> 2$  MHz) signals more effectively than the 25 micron ribbon, when the device is used as a blocking diode.

## 6.0 DEVELOPMENT OF INTEGRATED PREPULSE GENERATING SCHEMES

The original PFN, which had been proposed in the Phase I Report<sup>21</sup> and which had been thoroughly analysed with the ECA program (Section 5.2), proved to contain several practical weaknesses. It served, however, as a useful test bed for investigating a number of prepulse generating schemes. During this process, important information was gained about the practical requirements for initiating a fully developed electric discharge in an excimer laser gas mixture. It should be kept in mind, however, that failure to make the proposed circuit work as predicted, does not mean that the scheme is unworkable. The modifications needed to successfully implement the proposed excitation network were too extensive, too costly, and were realized too late in the present program to be seriously considered. Instead, a more direct way of generating a strong prepulse was chosen. It proved to be the most straightforward approach to meeting the most important goals of the program, pulse energy and laser efficiency.

The strong points and weaknesses inherent in the various prepulse techniques investigated are discussed in this section.

### 6.1 PREPULSE CIRCUITS

With the original prepulse circuit described in Figure 5-3, a magnetically switched positive pulse was generated which initiated the predischage. A negative backswing, caused by ringing in the predischage circuit, then served as the prepulse to overvolt the main discharge gap. The magnetic switches tested with this network were constructed as follows: The magnetic thyatron assist and inverse voltage block (L1S) was one of the Metglas cores (2605-C0) tested in the preliminary experiments (Section 5.3). Five electrical turns were wound on this core. Its unsaturated inductance was predicted to be close to 1 mH and its saturated inductance approximately 2 microhenries. The magnetic switch L2S, which was used to initiate the predischage, consisted of four identical 2605-C0 cores, as described in Section 5.3. Three of the cores were trimmed until all four cores had identical  $V \cdot t$ -products to well within 1%. Each core had an electrical winding of 7 turns of 7.6 cm wide copper strap, wound one turn over top of the other to reduce the saturated inductance. With the four inductors connected in parallel, the unsaturated inductance of L2S was determined to be 125 microhenries and its saturated inductance less than 500 nanohenries.

Early experiments showed that the saturated inductance of the magnetic assist inductor, L1S, was closer to 5 microhenries (including the stray inductance of the charging circuit), than to the 2 microhenries assumed in the design. As a result, it took almost 2  $\mu$ s to charge the PFL instead of the expected 1.1 microseconds. Consequently, the four magnetic Metglas reactors, L2S, saturated before the PFL was fully charged.

Taking electrical turns off inductor L1S to speed up the charging would have compromised the inverse voltage protection for the thyatron. Alternatively, adding more turns onto inductors L2S would have slowed down the positive voltage excursion. To bring the prepulse into coincidence with the peak of

the charging voltage appearing on the PFL, a set of second-stage saturable reactors, L3S, was added as shown in Figure 6-1. This second set of saturable inductors was wound on a set of ferrite cores and served to delay the voltage seen by the Metglas prepulse switches L2S. These high-inductance (50 turns) ferrite switches did not compromise the risetime of the prepulse generated, yet permitted charging times in excess of 2 microseconds.

Preliminary tests with  $N_2/He$ , with  $CO_2/N_2/He$ , with  $F_2/Kr/Ne$ , and with  $HCl/Xe/Ne$  mixtures in the discharge chamber showed that the predischage between cathode and screen could be initiated with the magnetically switched positive pulse as predicted. However, the large negative voltage spike (produced by voltage inversion in the predischage circuit) predicted by the theoretical model (see Figure 5-6) could not be produced in practice. Hence, difficulties were encountered in properly initiating the main discharge.

This discrepancy between theory and observation was traced to the model assuming that the inductance  $L_K$  (Figures 5-3 and 6-1) in the predischage circuit was concentrated at the cathode, whereas in reality the inductance was distributed over the entire circuit. When the model was modified to reflect a 5 nH inductance distributed over the predischage circuit, it generated only very short (8 ns) and erratic negative voltage spikes, only 30% over the charging voltage (Figure 6-2). These skinny voltage backswings were consistent with observed behavior. Needless to say, the short voltage spikes were insufficient to drive the avalanche discharge in the main gap through its formation stage. Increasing the charging voltage resulted in self-breakdown of the main discharge gap, causing the discharge to arc.

It was believed that the problem could be corrected by adding a physical inductor (coil) between the cathode and the center plate of the PFL. With a lumped inductance of 20 nH between cathode and PFL, the model predicted a much stronger negative voltage prepulse, 25 ns wide and with a peak of twice the charging voltage (Figure 6-3). Such a voltage spike should have been sufficient to fire the main discharge.

The idea was put into practice by building a new cathode which was insulated from the PFL, so that a physical inductor could be inserted between cathode and PFL. A set of thin stainless steel wire connections served to make up the 20 nH inductance. When the new configuration was tested, a 25 ns wide negative prepulse could indeed be generated (Figures 6-4 and 6-5), but its amplitude was still only 35% over the charging voltage. As before, the main discharge could not be initiated. At higher charging voltages, the arcs were brighter than before, which was attributed to the increased head inductance, estimated to be 40 nH. It was concluded from these tests, that the only way the prepulsed double-discharge scheme could be made to work, was to place the prepulse-generating saturable inductor between the cathode and the PFL. This would have required rebuilding the entire electrode and feedthrough structure, as well as the PFL.

At this point, it was decided to re-install the non-inductive cathode and to apply a magnetically switched negative prepulse to the screen directly. To accomplish this, the PFN was modified with the magnetic switches reconnected in the configuration shown in Figure 6-6. The capacitors C1 between cathode and screen were removed.

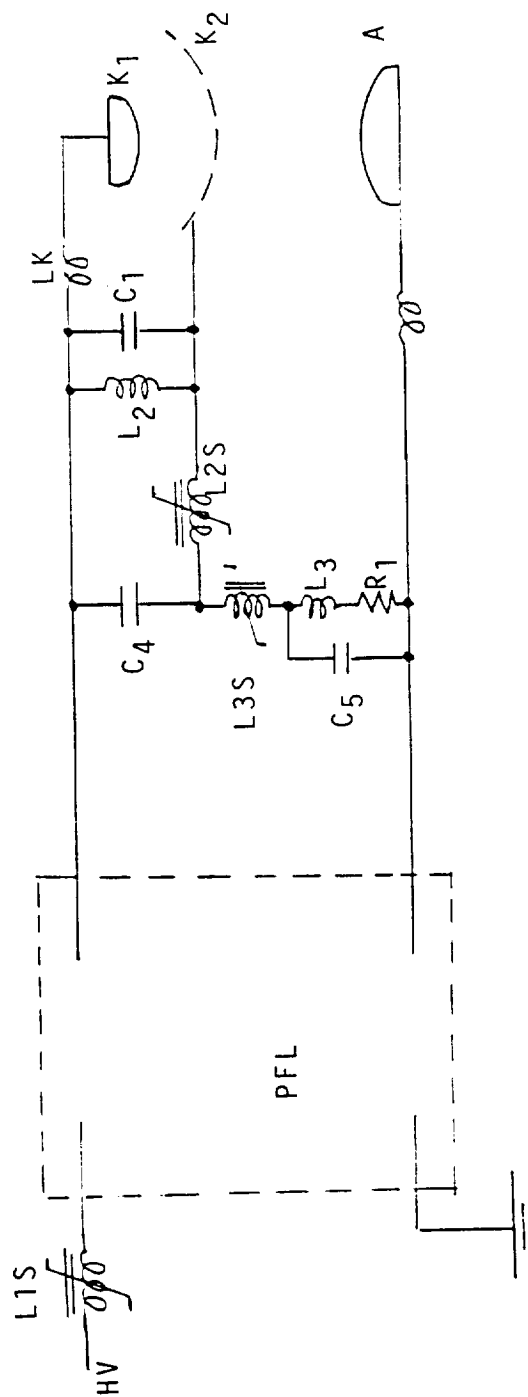


FIGURE 6-1. ORIGINAL PREPULSE CIRCUIT; MAGNETICALLY SWITCHED POSITIVE PULSE FOLLOWED BY PREDISCHARGE SWITCHED NEGATIVE PULSE

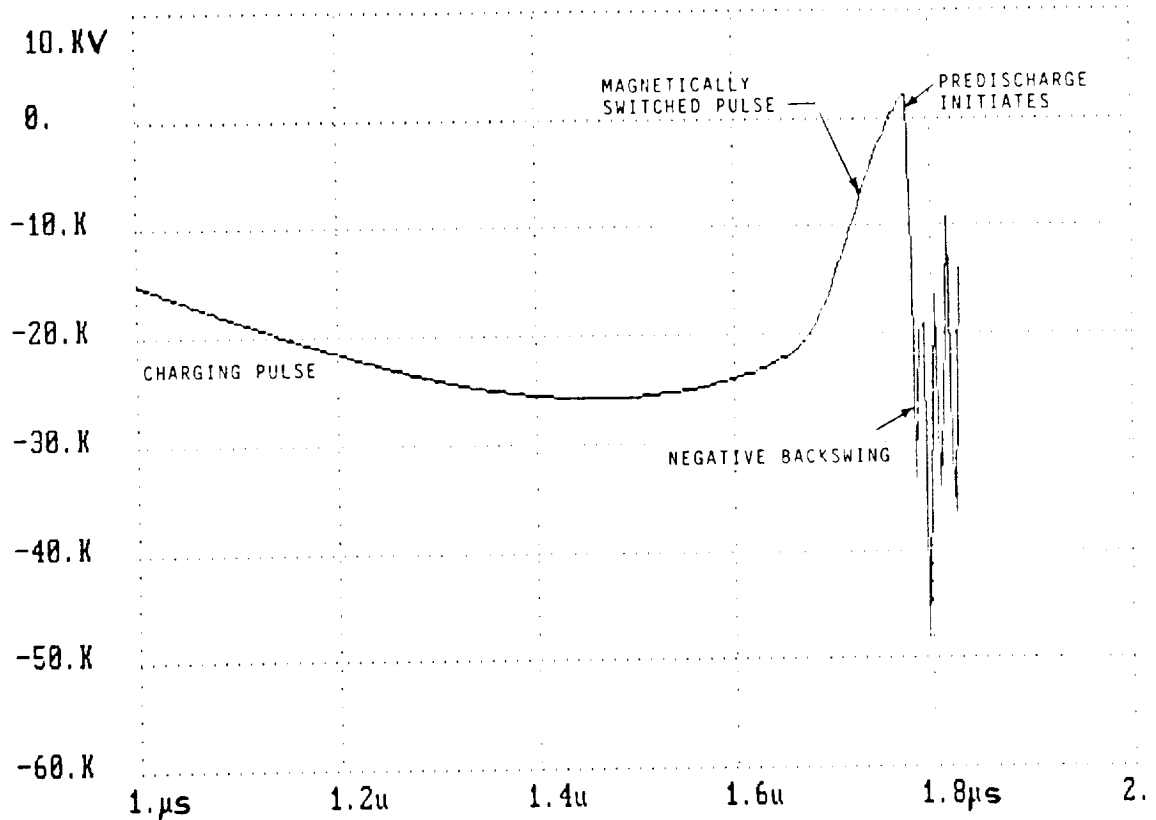


FIGURE 6-2. CALCULATED VOLTAGE ACROSS MAIN GAP FOR  $L_k = 5 \text{ nH}$  DISTRIBUTED OVER PREDISCHARGE CIRCUIT

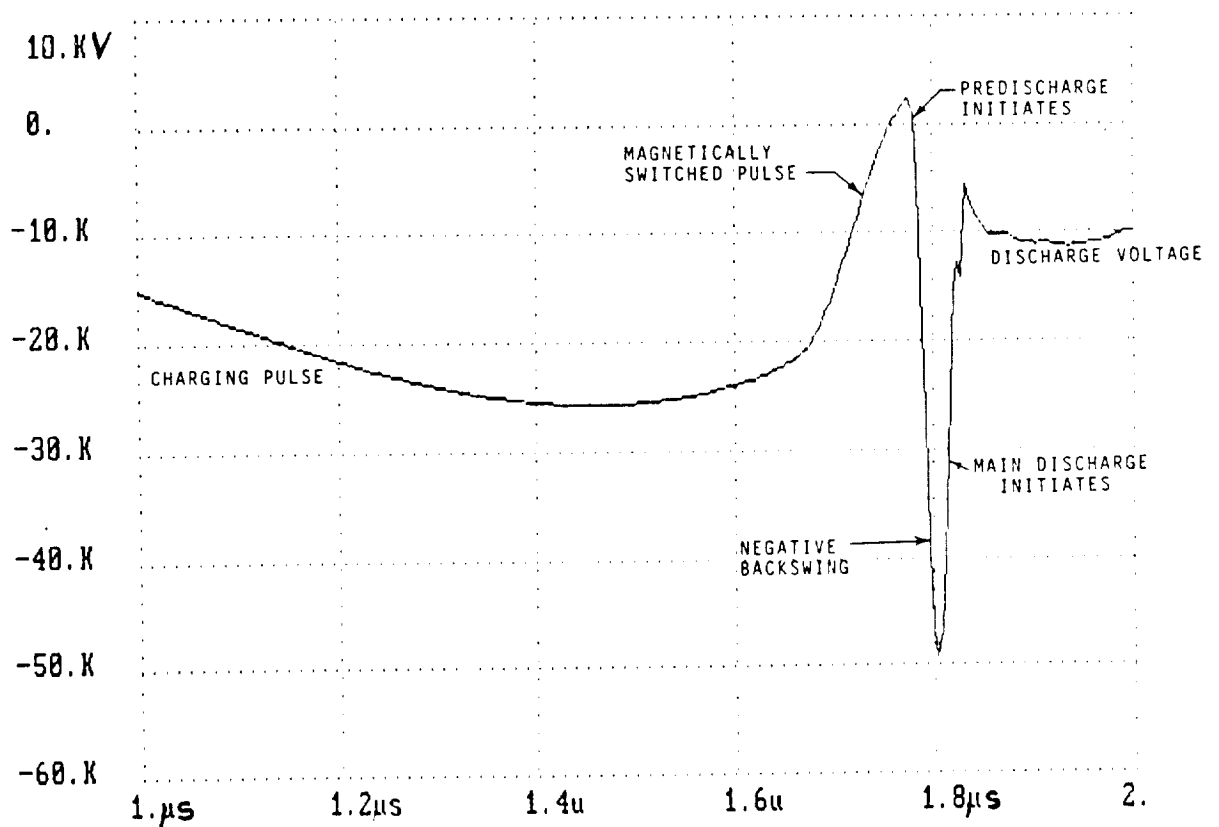


FIGURE 6-3. CALCULATED VOLTAGE ACROSS MAIN GAP FOR LUMPED 20 nH CATHODE INDUCTANCE

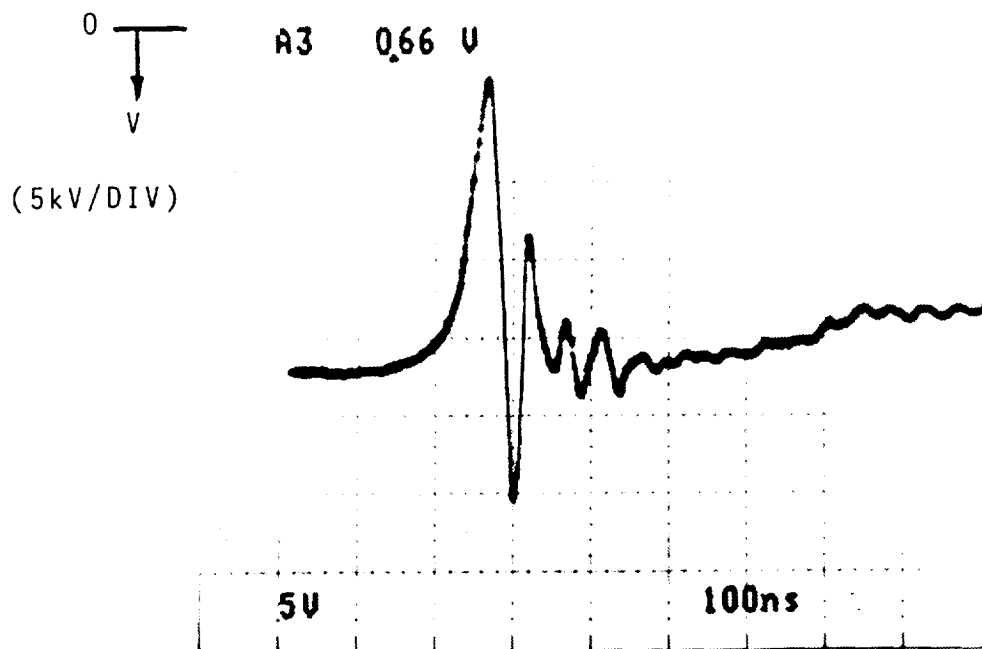


FIGURE 6-4. MEASURED SCREEN VOLTAGE SHOWING PREPULSE GENERATED BY CIRCUIT IN FIGURE 6-1 (100ns/DIV)

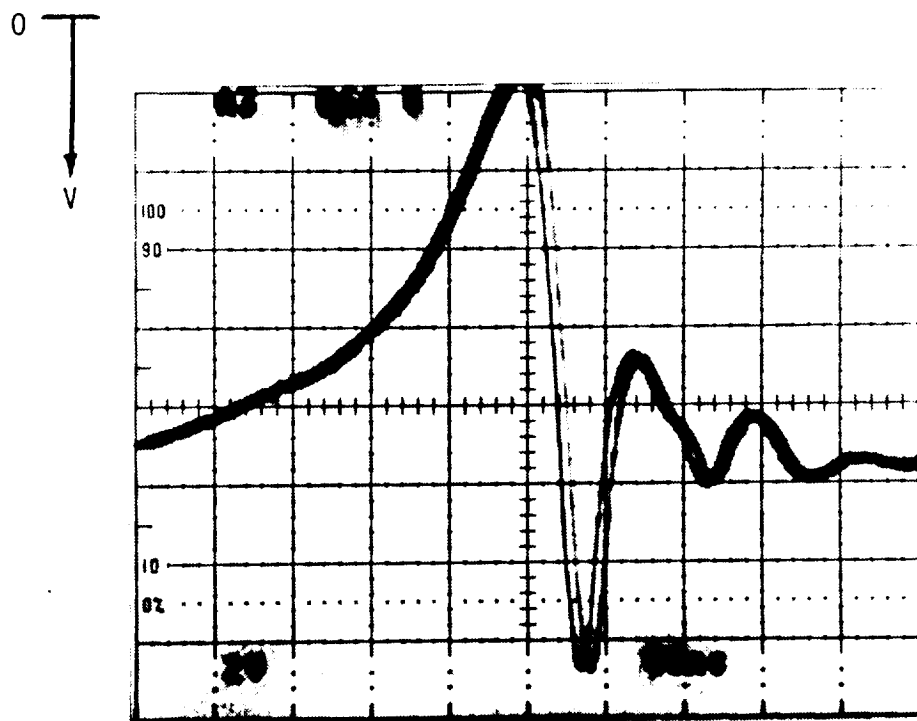


FIGURE 6-5. EXPANDED TRACE OF PREPULSE AT 50 ns/DIV SHOWING PREPULSE TO BE 25 ns WIDE

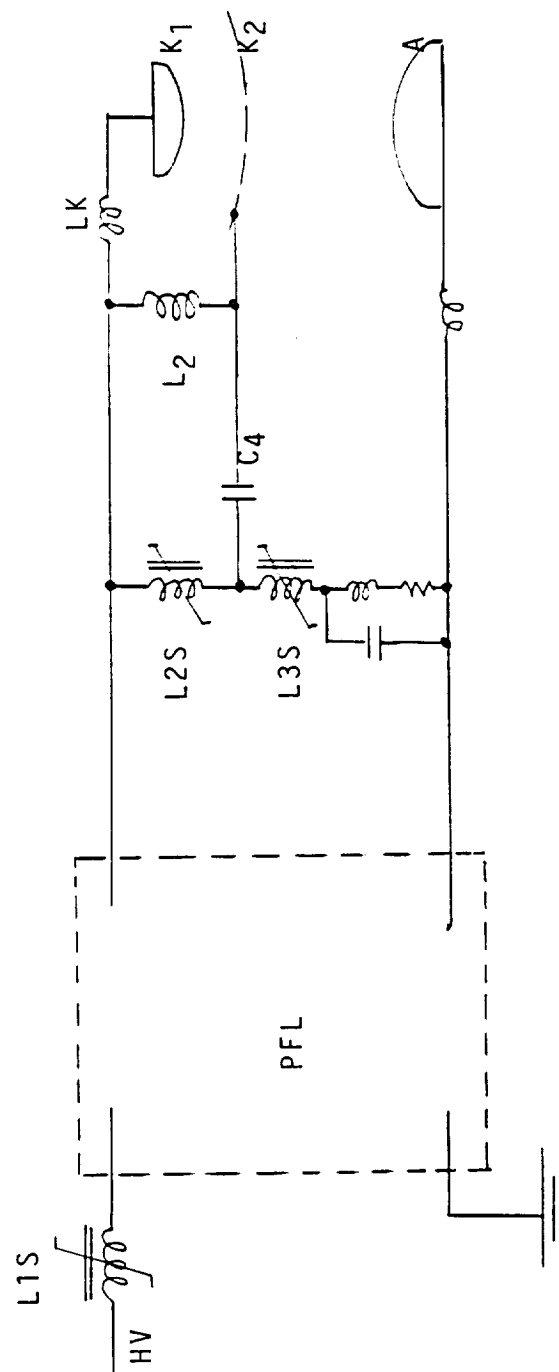


FIGURE 6-6. MODIFIED PREPULSE CIRCUIT; MAGNETICALLY SWITCHED NEGATIVE PULSE

With this arrangement of PFN components, capacitor C4 remained essentially uncharged during the slow charging pulse. When L3S saturated, C4 started to charge, adding voltage across L2S. When L2S saturated (after its  $V \cdot t$ -integral was exhausted), the negative voltage on C4 was added to the PFL voltage and applied to the screen. Typical prepulse spikes generated by this scheme are shown in Figures 6-7 and 6-8.

With the magnetically switched negative prepulse circuit of Figure 6-6, only weak glow discharges could be initiated under ideal conditions in XeCl and KrF mixtures. Glow discharges were observed over a very limited voltage range. Generally, one or more of the following conditions would be observed, depending on charging voltage and gas pressure:

1. Voltage oscillations introduced by the saturation of L3S (see Figure 6-7) caused the predischage gap to break down prematurely during the slow charging of the PFL. This invariably resulted in arc formation.
2. For conditions under which an avalanche discharge was initiated in the main gap, the prepulse circuit lacked sufficient speed (i.e. had too high an output impedance) to provide the necessary  $dI/dt$  for driving the discharge impedance down to the self-sustaining 1 ohm level.

The latter observation and deduction provided the clue for identifying the primary problem. For the weak discharges observed, the experimentally determined values of the discharge impedance and the associated pump power density were 20 ohm and 25 kW/cm<sup>3</sup>, respectively. The discharge was hardly self-sustaining and was well below lasing threshold of an RGH laser.

It has generally been assumed (see published literature) that an impedance-matched discharge can be initiated by a fast high-voltage spike. With the emphasis being on voltage, the fast current capability required for a successful prepulser has not been given enough importance. The present investigation has shown that the prepulser has to supply a fast current pulse as well as a fast voltage pulse. The output impedance of the prepulse circuit should thus be well below 10 ohm, preferably near 1 ohm. It became clear at this point that the prepulse generating switch had to have a lower impedance when in the conducting mode. For a magnetic switch, its saturated inductance should be less than 50 nH instead of 800 nH (the inductance of the four 7-turn Metglas switches, L2S, in parallel).

A new low-impedance prepulser (Figure 6-9) was designed which applied a fast negative pulse directly to the main discharge gap, as before, but which had the following important improvements:

1. The saturated inductance of the prepulse generating magnetic switch was 50 nH or less.
2. To increase the prepulse amplitude, a voltage-doubling network was "piggy-backed" onto the PFL. This circuit could in principle generate a peak prepulse voltage which was three times the charging voltage. This voltage doubler had the further advantage, that the switch inductance was not part of its output impedance.
3. A resistive/inductive voltage divider ( $R_k$  and  $L_A$ ) had been added to the electrodes, which made the electric fields in the "predischarge" gap and in the main discharge gap approximately equal during charging.



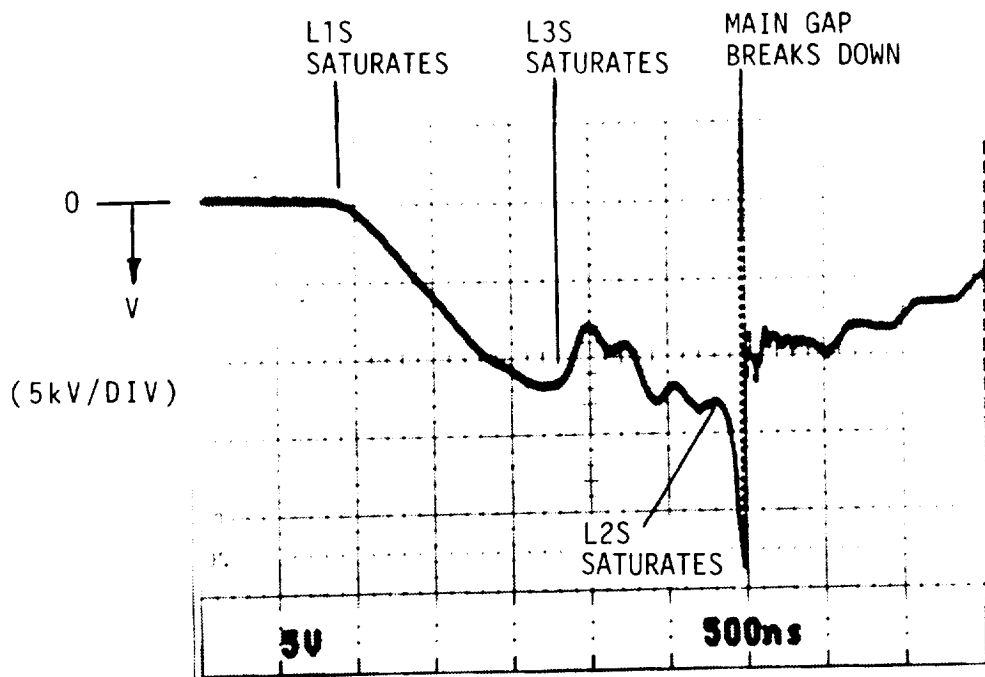


FIGURE 6-7. SCREEN VOLTAGE FOR CIRCUIT IN FIGURE 6-6.  
(FAINT GLOW IN MAIN GAP)

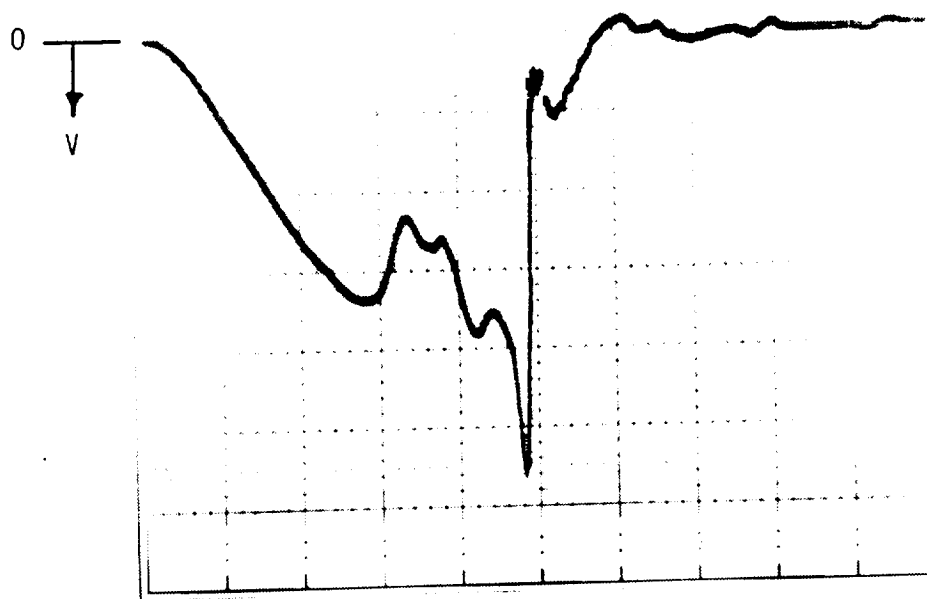


FIGURE 6-8. SCREEN PULSE AT HIGHER CHARGING VOLTAGE  
(ARC IN MAIN GAP) 5kV/DIV, 500ns/DIV

ECA modeling of this new prepulse circuit proved that much wider and stronger prepulses were possible (Figure 6-10). In the calculation, the inductance of switch  $L_2$  was taken as 50 nH,  $C_A$  was 4 nF,  $C_B$  was 8 nF,  $R_3$  was 0,  $L_3$  was 4  $\mu$ H,  $R_K$  was 5 ohm, and  $L_A$  was 50  $\mu$ H. Note that the screen voltage ( $K_2$ ) tracked the cathode voltage ( $K_1$ ) very nicely during charging of the PFL, with the cathode/screen voltage and the screen/anode voltage being roughly in the same ratio as the physical electrode gaps. When  $L_2$  switched to a low impedance, the charge on  $C_A$  was inverted and a strong negative prepulse was applied to the screen. During the rise of the prepulse, the field in the cathode/screen gap first diminished to zero before inverting, while the main discharge field increased monotonically to three times its original value, or to twice the charging voltage. This made it possible for the main discharge to initiate before (or at least simultaneously with) the discharge in the cathode/screen region. Even though  $L_2$  was not part of the prepulse current path, its inductance determined the width of the voltage prepulse; i.e. it controlled the  $dV/dt$ . A fast rising prepulse therefore still required a switch with a very low inductance.

To prove the viability of this circuit (Figure 6-9), a low-inductance voltage doubler (Blumlein) was built and was integrated into the laser PFL. Until a new, fast magnetic switch could be designed and built, a low-profile (Maxwell) triggered spark gap was substituted for  $L_2$ . The inductance of the spark gap and connections was estimated to be 40 nH. Output impedance of this prepulser was in the 2 to 3 ohm range.

With this arrangement, lasing discharges could be produced over a wide range of charging voltages and gas pressures. With a typical XeCl mixture of 5 atm Ne, with 0.4% Xe and 0.08% HCl, and 28 kV charging voltage, approximately 1 J/pulse of optical laser energy was extracted. Efficiencies, based on measured voltages were in the 2.5% range. The PRF was limited to 1 Hz by the operating characteristics of the spark gap.

Cathode and screen voltages, showing the spark gap switched prepulse, are shown in the oscilloscope record reproduced in Figure 6-11. Note that the prepulse is between 40 and 50 ns wide. Near the peak of the prepulse, both gaps appear to break down simultaneously, leading to a 150 ns wide discharge pulse. The measured optical pulse was 100 ns wide.

A stable, multimode resonator with 70% output coupling was employed. The total rear reflector was concave with a 10 m radius of curvature and the output coupler was flat. Laser beam burn marks indicated a 2.8 cm x 3.3 cm beam cross-section (Figure 6-13). The near-field intensity profile, obtained by scanning a 1 mm wide slit and energy detector across the beam (side to side) as the laser was repetitively pulsed, showed a profile halfway between Gaussian and top-hat (Figure 6-14). With higher pump power density and with an unstable resonator, the beam profile was expected to become more rectangular. In the vertical direction (anode to screen) the beam intensity profile was by necessity already much more rectangular.

Having successfully demonstrated that the fast prepulse circuit in Figure 6-9 was able to produce good lasing output, a new fast magnetic switch was

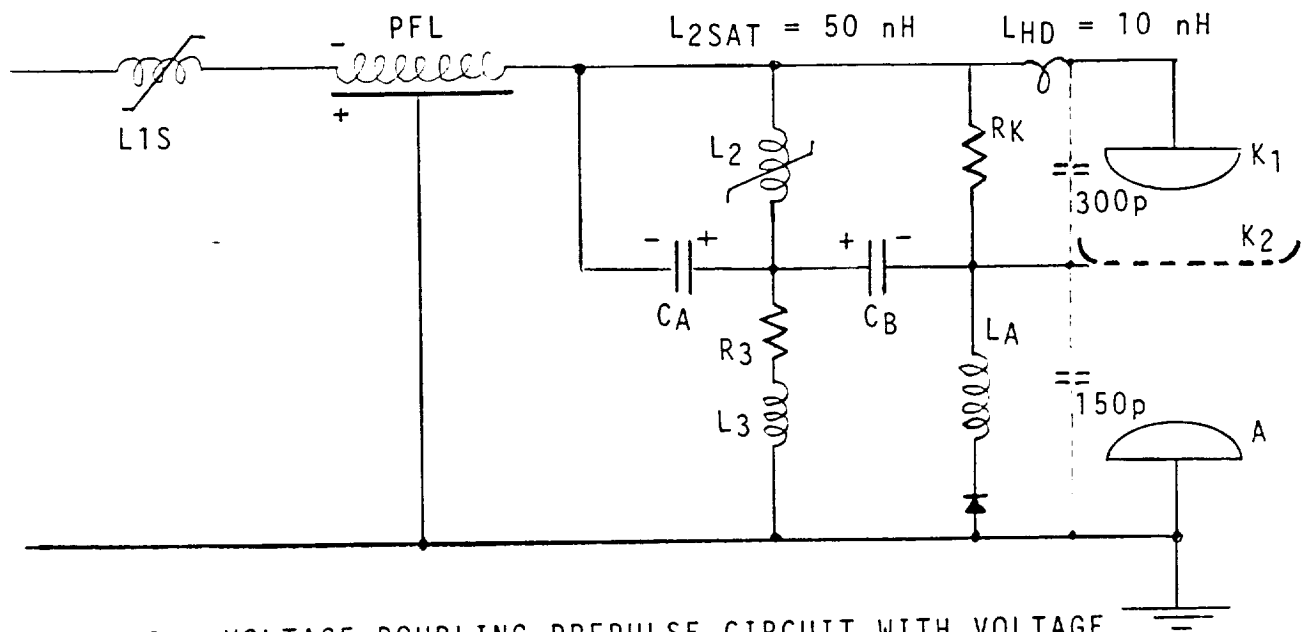


FIGURE 6-9. VOLTAGE-DOUBLING PREPULSE CIRCUIT WITH VOLTAGE DIVIDER AND FAST SWITCH ( $L_2$ )

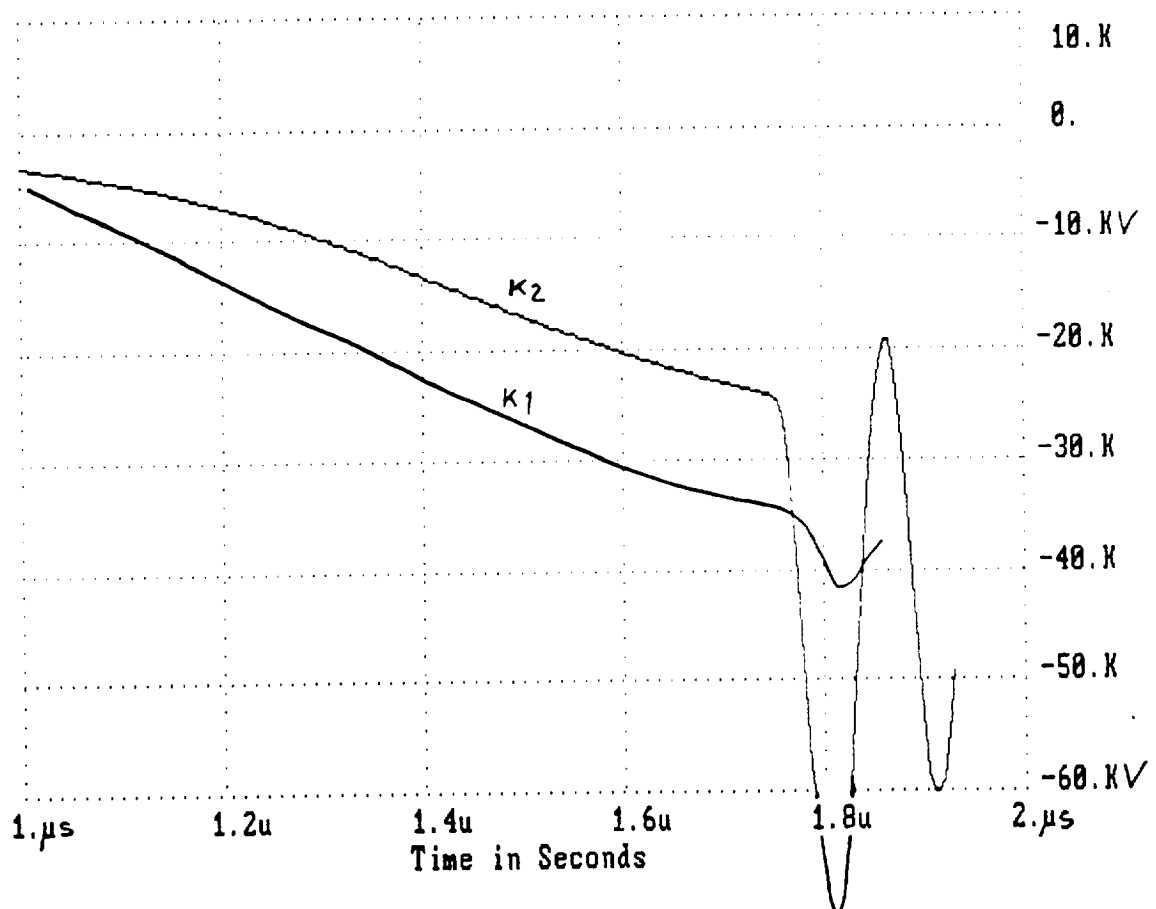


FIGURE 6-10. CALCULATED CATHODE ( $K_1$ ) AND SCREEN ( $K_2$ ) VOLTAGES FOR  $L_{2SAT} = 50 \text{ nH}$

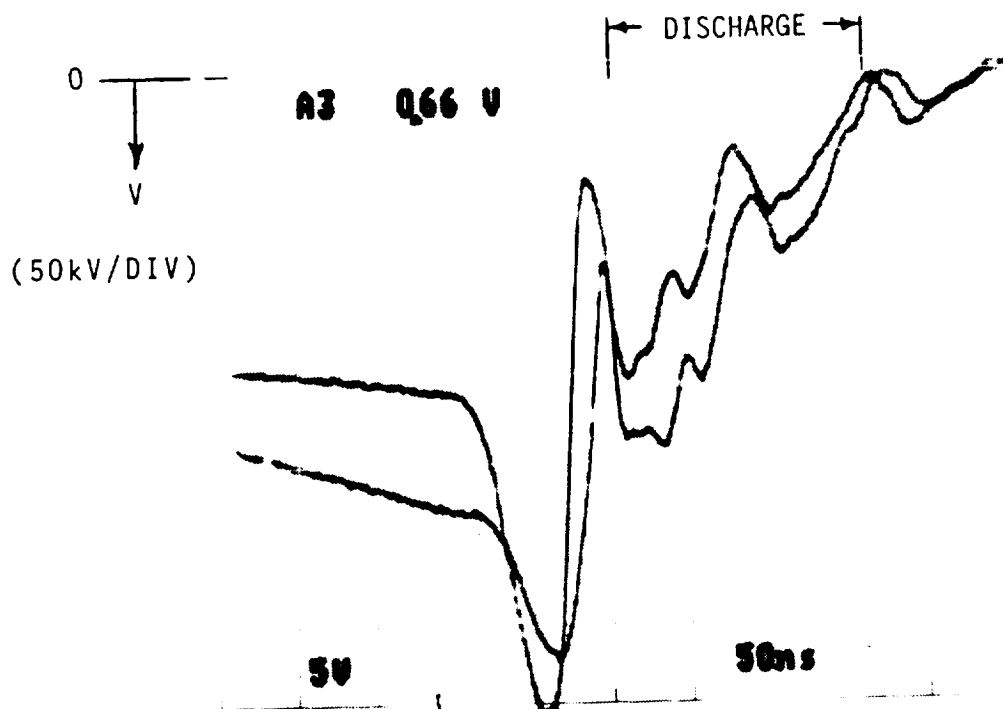


FIGURE 6-11. CATHODE AND SCREEN VOLTAGES FOR SPARK-GAP SWITCHED PREPULSE (50ns/DIV)

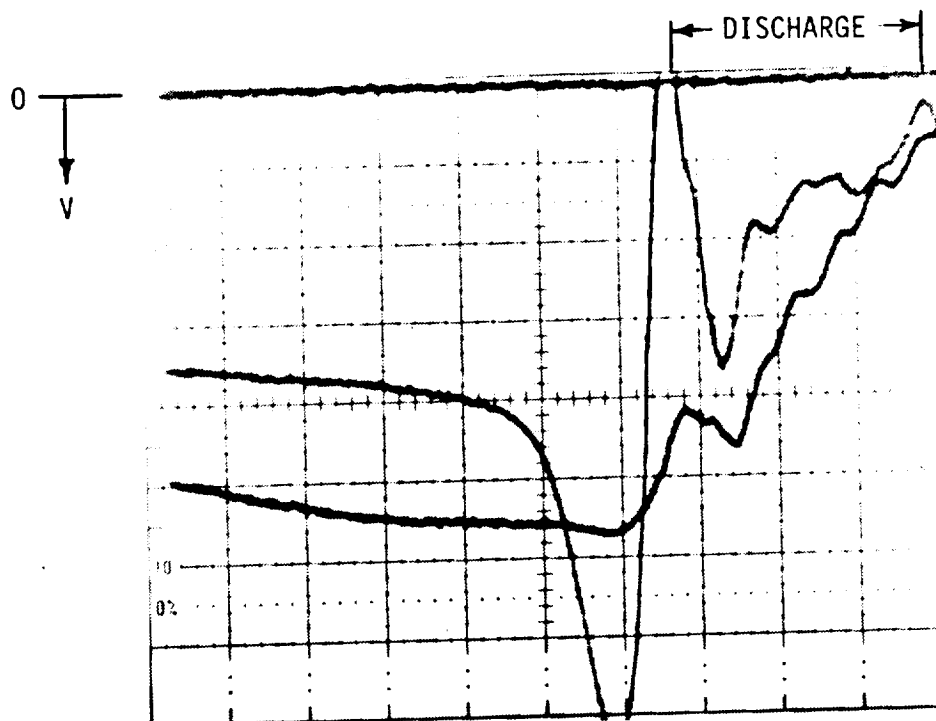


FIGURE 6-12. CATHODE AND SCREEN VOLTAGES FOR MAGNETICALLY SWITCHED PREPULSE (50ns/DIV)

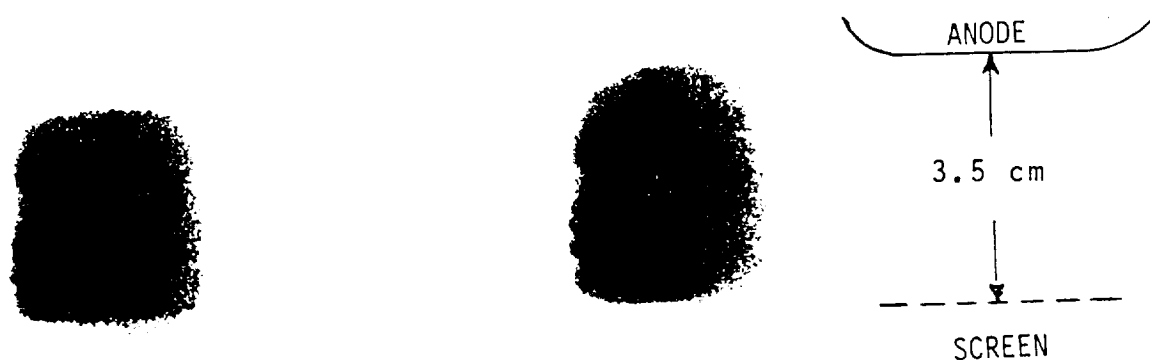


FIGURE 6-13. LASER BURN MARKS (ON THERMAL PAPER) FOR TWO DIFFERENT MIRROR ALIGNMENTS (1 JOULE OUTPUT)

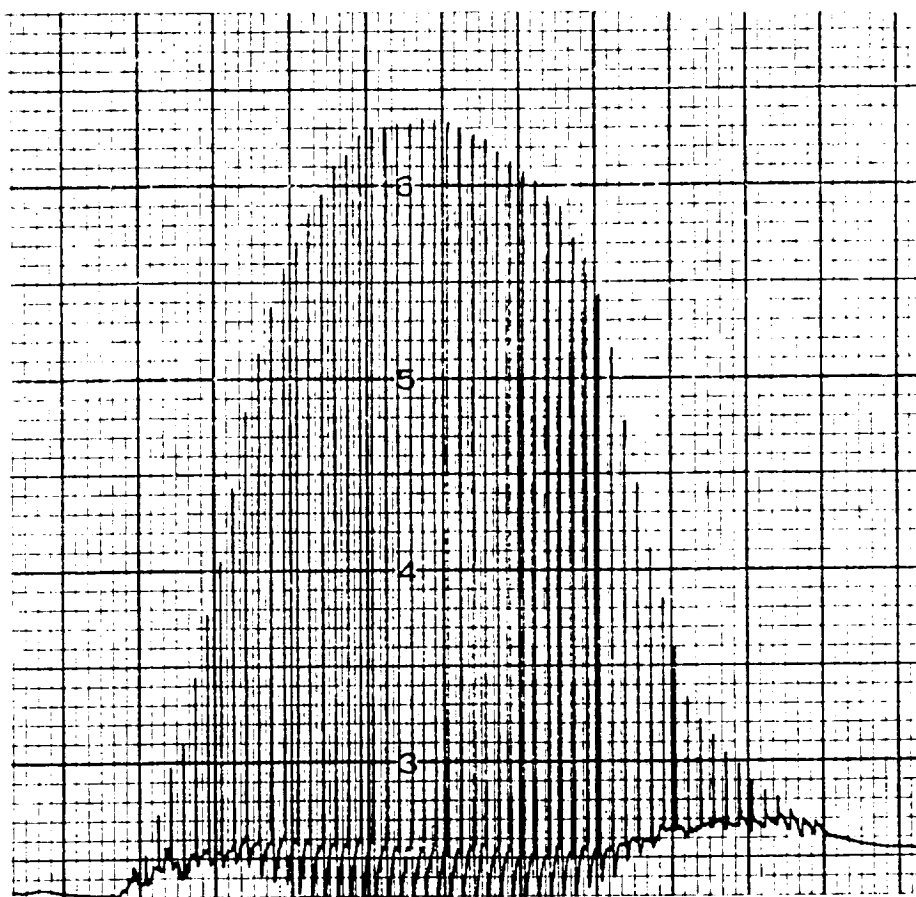


FIGURE 6-14. SIDE-TO-SIDE INTENSITY PROFILE OF LASER BEAM (VERTICAL SLIT AND DETECTOR WERE SCANNED ACROSS BEAM), REAR REFL. = 10 m RC TOTAL OUTPUT COUPLER = 30% REFL. FLAT

designed for directly replacing the spark gap. The spark gap needed to be replaced for increased system reliability and life, and for making it possible to operate at higher PRF. The design of this magnetic switch is described in the next section.

## 6.2 MAGNETIC SWITCH DESIGN

The original 7-turn magnetic Metglas switches, one of which is shown in Figure 6-15, were too slow and did not even come close to the spark gap performance. Consequently, a new single-turn magnetic switch was designed with an estimated saturated inductance of 50 nH. The choice of material and shape was dictated by the required switch characteristics. The core was wound into an 11 cm ID by 25 cm OD toroid with 15 micron thick 2605-CO Metglas ribbon and 6 micron thick Mylar tape. Because there was only one electrical turn, the core had to be relatively large and heavy to hold off 35 kV for even 300 ns. This was so in spite of the fact that the 2605-CO material provides the highest known  $\Delta B$  swing of 3.3 T (i.e. 33,000 gauss). The toroidal shape was chosen to minimize the degradation in the squareness of the hysteresis loop caused by rewinding of the preannealed Metglas ribbon (see discussion in Section 5.3). The measured B-H curve for this core is significantly more narrow and rectangular (Figure 6-17) than the corresponding B-H loop for the previously constructed oval cores (Figure 5-11). This demonstrates that the geometry, as well as the annealing and winding techniques are extremely important for the production of a fast Metglas switch.

A pictorial drawing, showing the magnetic switch installed in the low-inductance prepulser, is given in Figure 6-16. The single electrical turn consisted of an 8 cm diameter brass pipe going through the center of the core. Fast switching action, comparable to the spark gap performance, was achieved because of the low impedance construction of the core and prepulser and because of the squareness of the hysteresis loop.

A direct comparison between the voltage prepulses produced by the spark gap and by the fast Metglas switch can be made by comparing Figures 6-11 and 6-12. Apart from a somewhat more rounded knee, observed with the magnetically switched pulse, the prepulse shapes are virtually the same. The saturated inductance of the magnetic switch is, therefore, also close to 40 nH.

Since the  $V \cdot t$ -product of the new switch was only  $1.1 \times 10^{-2}$  V-s, it was not capable of holding off the full charging pulse lasting close to two microseconds. Consequently, other changes had to be made to the PFN and the prepulser shown in Figure 6-9. These were:

1. The number of electrical turns on the magnetic assist inductor L1S was reduced from five to two. This shortened the energy transfer time from the storage capacitor (in the pulse charging tank) to the PFL to 1.1 microseconds.

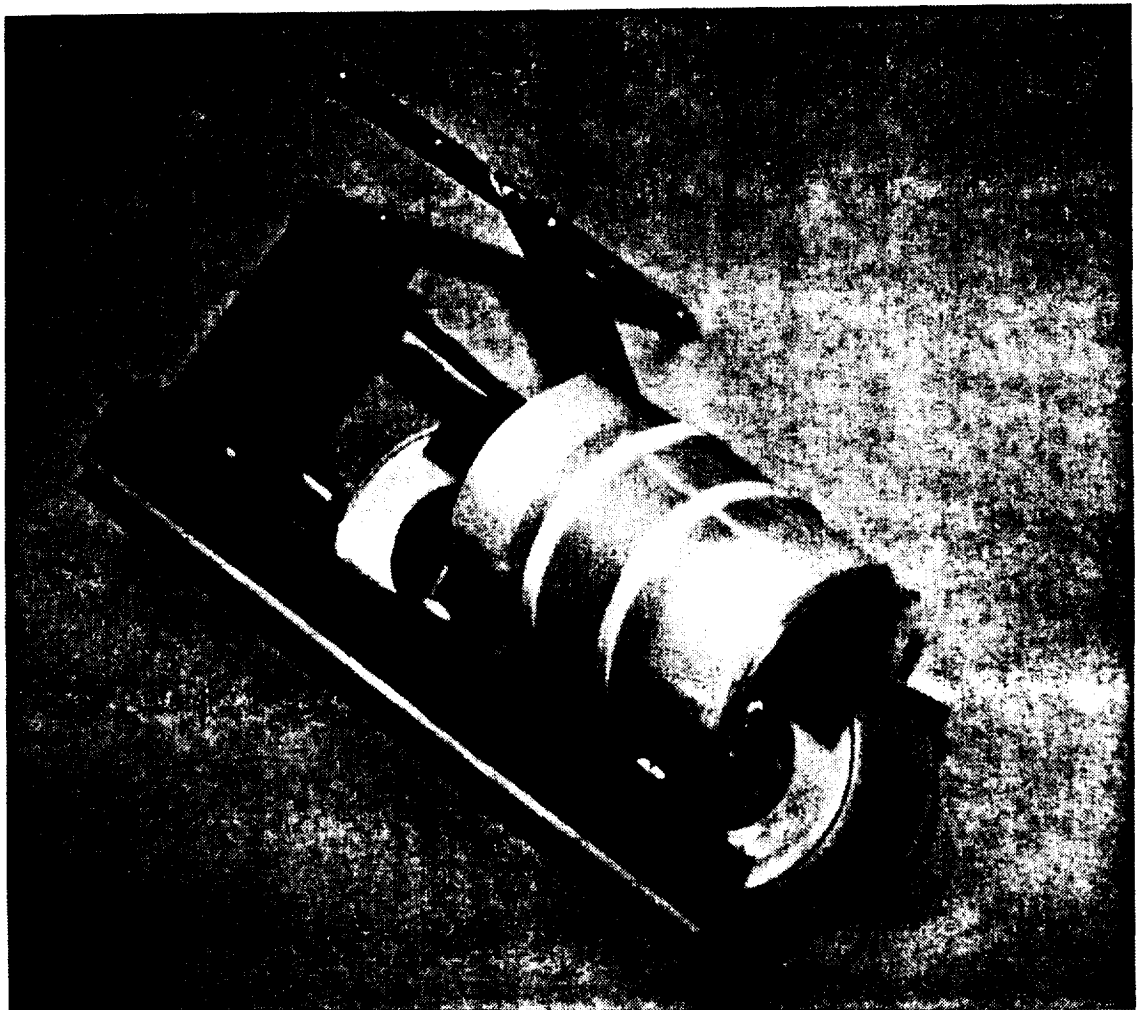


FIGURE 6-15. ONE OF THE 7-TURN MAGNETIC SWITCHES  
ORIGINALLY USED FOR L2S

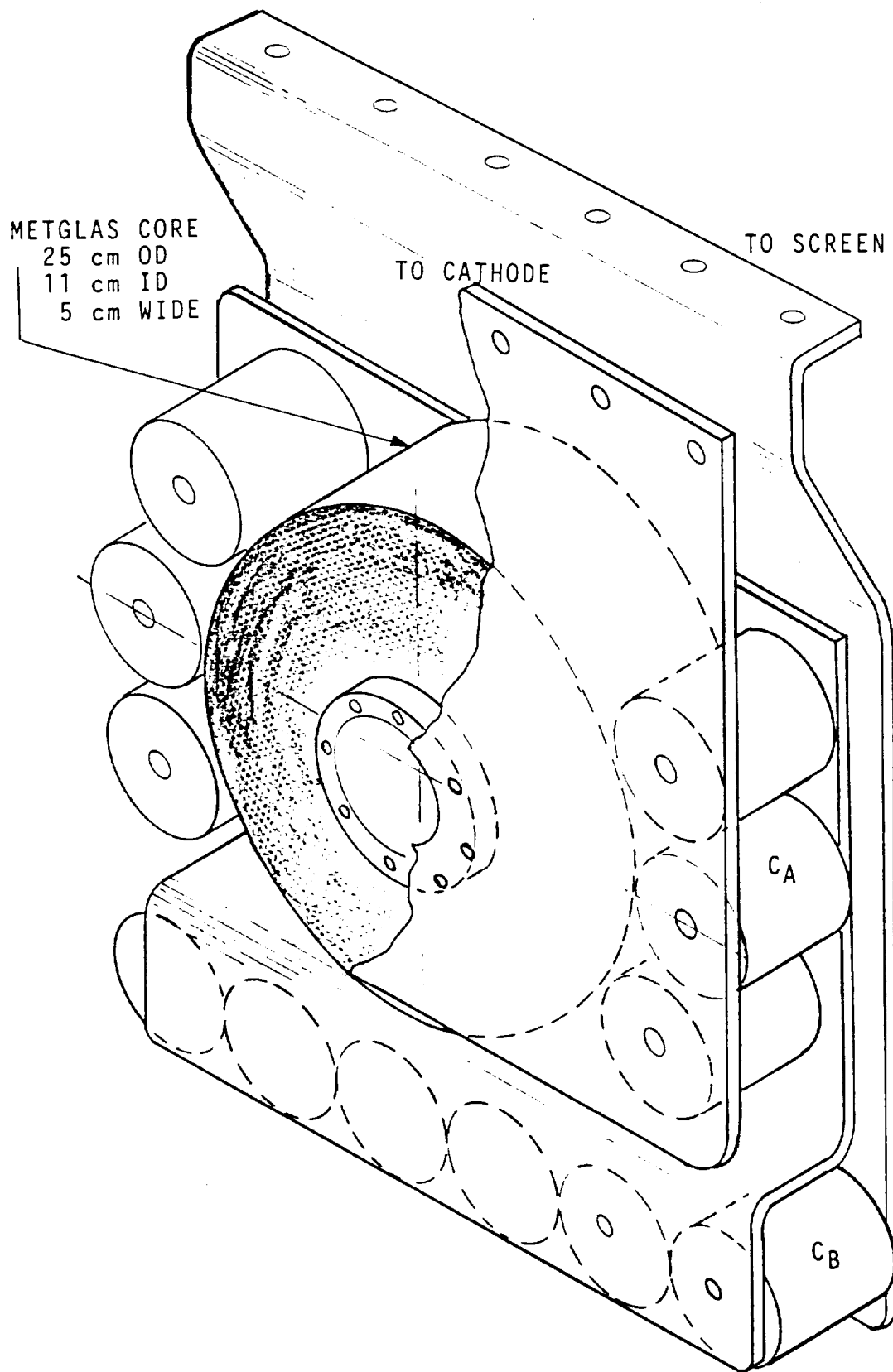


FIGURE 6-16. FAST MAGNETIC PREPULSER





2. The fixed inductor  $L_3$  was replaced by a saturable core inductor, so that the fast magnetic switch,  $L_2$ , did not experience the full charging voltage for the entire charging pulse. One of the original L2S inductors (see Figure 6-15) was modified by reducing its electrical turns from 7 to 3. It was then installed into the prepulser circuit in place of  $L_3$ .
3. A non-inductive 11 ohm (100 W) damping resistor,  $R_3$ , was installed to provide critical damping of the voltage perturbation caused by  $L_3$  saturating and the subsequent charging of capacitors  $C_A$  and  $C_B$  (Figure 6-9).
4. New values of the other components in the prepulse circuit were:  
 $C_A = 10 \text{ nF}$ ,  $C_B = 10 \text{ nF}$ ,  $R_K = 16 \text{ ohm}$ ,  $L_A = 35 \text{ } \mu\text{H}$ . The diode in the voltage divider (Figure 6-9) was added to aid in the resetting of saturable-core reactors  $L_2$  and  $L_3$ .

With the original multi-turn magnetic reactors, the cores were reset automatically when the Maxwell storage capacitor was charged from the A.L.E. switched supply. Since this supply could generate charging pulses with only 1 A amplitude, the cores were reset with a magnetic field intensity of less than 15 ampere-turns/meter, which proved to be very marginal. With the new single-turn saturable inductors, this method of resetting the cores was no longer satisfactory, and it became necessary to actively reset the cores with a separate reset circuit. Active reset circuits are the subject of the next section.

### 6.3 CORE RESET TECHNIQUES

Full resetting of the Metglas cores can be achieved with magnetizing fields between 50 and 100 A-turn/m. Incomplete core reset can result in significant time jitter in the time to saturation. This problem is illustrated in the example given in Figure 6-18, which shows the time jitter in the prepulse as a result of insufficient reset current for switch  $L_2$ .

At first glance, resetting the magnetic cores to their opposite remanence state appears to be a straightforward procedure. This is in fact not so, and several months of effort were devoted during this program to perfect the pulse resetting networks. The first thought generally is to wind an auxiliary reset winding with many turns on each core, so that only milliamperes of current are required to provide the necessary reset field. It must be kept in mind, however, that any additional winding will convert the magnetic inductors into transformers. During reset, the laser PFN acts as a secondary circuit coupled to the primary circuit, modifying the reset pulse. Conversely, during excitation of the laser PFN, the reset windings act as secondaries. Since the laser PFN switches voltages in the tens of kilovolt, many megavolts would be induced in the multi-turn reset windings. Even if these windings are effectively open-circuited during pulsing of the laser, the induced voltages would be impossible to handle without electric breakdown.

It becomes apparent, therefore, that any auxiliary reset winding should have no more turns than the primary number of turns on the saturable inductor. Alternatively, the reset current pulse should be applied directly to the laser

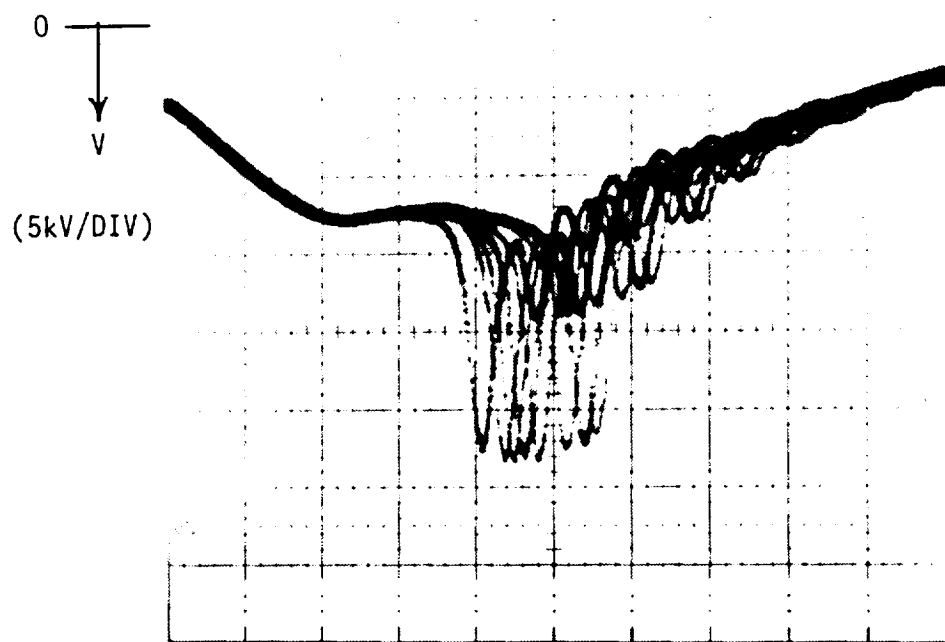


FIGURE 6-18. PREPULSE TIME JITTER WITH INSUFFICIENT RESET  
(200ns/DIV)

PFN without the use of auxiliary windings. Since our fast magnetic switches have only one or two turns, the reset current has to reach several tens of amperes to be effective. This leaves three alternative reset schemes:

1. The cores can be reset with a steady DC current of approximately 50 A from a low-voltage DC source (e.g. a 12 V car battery). The DC source can be protected from the high PFN voltage pulses with high-impedance chokes. This appears to be the simplest way to reset the cores. At low PRFs, the scheme would be uneconomical, however, since 600 W is an appreciable power loss when compared with a laser input power of only a few kW. At PRFs above 100 Hz, where DC resetting would become efficient, there may not be enough interpulse time to overcome the high  $V \cdot t$ -products of the magnetic inductors with only the 12 V signal, especially when more than one core needs to be reset in a sequential manner.
2. The cores can be reset with millisecond long pulses at the 200 V level. A circuit to accomplish this is shown in Figure 6-19. Here, the 200 V quasi-DC signal is switched onto a set of secondary windings, added onto the saturable cores (in approximately a 1:1 ratio), by a high-current transistor (e.g. a HEXFET). The high-impedance chokes,  $L_F$ , serve to protect the HEXFET transistor from high-voltage transients induced into the reset circuit when the PFL is pulsed. These chokes have been wound on ferrite cores which have a very slanted B-H loop, so that these cores have a remanence induction close to zero and do not require resetting. They do have to be driven into saturation by the reset pulse, however, for the reset current to reach 50 A. A 1.6 ohm damping resistor has been inserted into the reset circuit to prevent current reversal. The reset pulses are produced by switching the HEXFET on and off with an optically isolated gate driver. The pulse length can be adjusted from 1 ms to 5 ms by an RC-timing network, controlling a monostable multivibrator. The reset circuit is triggered at the same time as the laser, so that the cores are reset right after the laser pulse. This reset circuit has worked very effectively for resetting switches L2S and L3S. In practice, this circuit could not be used to reset L1S, because it was difficult to add a secondary winding on this core, since it was located in a separate tank.
3. A third way of resetting the cores is schematically shown in Figure 6-20. This circuit has been used in most of the recent laser tests. Here, a +6 kV pulse of approximately 10 microsecond duration is directly applied to the laser PFN at the thyatron anode to simultaneously reset all three cores, L1S, L2S and L3S. A 50 kV diode blocks the normal 35 kV PFN charging voltage from getting into the reset circuit. The pulses are produced by switching the charge on a 3  $\mu$ F capacitor, charged to 1.2 kV, through the primary of a 1:5 step-up pulse transformer with a high-voltage, high-current thyristor (such as the AEG G600-R1600K GTO thyristor shown in the diagram). The thyristor is protected from negative transients (fed back from the laser PFN) by a number of inductors, shorting diodes and metal-oxide varistors (MOVs). In practice, it was found advantageous to apply the reset pulse at two points of the laser PFN simultaneously, at the thyatron anode and at the laser cathode. This resulted in more consistent resetting of all three cores and in jitter free operation.





## 7.0 TEST RESULTS

With the fast magnetic voltage-doubling prepulser and the directly applied pulsed core reset circuit, described above, best laser performance has been obtained with XeCl mixtures containing Xe and HCl in the ratio of 10:1 and at total pressures of 5.6 atm absolute. Typical gas mixtures would contain 2 torr HCl and 20 torr Xe in a diluent of neon. Most efficient laser operation has been observed at 30 kV charging voltage, although the laser has operated well over the range from 20 kV to 35 kV.

The diagnostic equipment for monitoring the laser output and the laser operation consisted of the following instruments:

1. A 100 kV high-voltage probe (Gentec, 1000:1 voltage divider) for monitoring the voltage at the cathode and at the screen.
2. Pulsed current probes (Ion Physics, 0.1 V/A) for monitoring the e-beam current and the reset current pulses.
3. Pyro-electric pulse energy meter (Gentec) for measuring optical pulse energy.
4. Laser thermopile power meter (Scientec) for measuring average optical output power.
5. Vacuum photodiode (ITT, 1 ns response) with S-5 cathode for measuring optical pulse shape.
6. Various MHz, 100 MHz (storage), and 500 MHz (with electron multiplier) oscilloscopes (Tektronix) were employed to monitor the voltage signals.

Typical voltage pulses observed on the cathode and the screen are superimposed (two successive shots) in Figure 7-1. Sweep speed was 200 ns/cm. The screen voltage can be seen tracking the cathode voltage for the most part of the charging pulse, which here takes about 1100 ns to complete charge transfer. Three hundred nanoseconds before the cathode voltage (and the PFL voltage) reaches the peak, the screen voltage separates from the charging curve as L3S saturates and allows the prepulse capacitors to charge up. Five hundred nanoseconds later L2S saturates and generates the prepulse appearing on the screen. Near the peak of the prepulse, the main discharge gap breaks down, pulling the screen voltage to ground. At this time, a large voltage is developed across the cathode-screen gap, the small gap breaks down and brings the screen voltage back up close to the cathode (and PFL) voltage. With both gaps ignited, the discharge current can pass from the PFL into the discharge plasma. For the next 150 ns (i.e. during the pump pulse), the cathode and screen voltages again track each other. The separation between the cathode and discharge voltages during the pump pulse reflects the physical separation between the electrodes. This indicates that the sustaining E/p field is approximately the same in both discharge gaps. The experimental E/p field here works out to approximately 600 V/cm-atm, which is close to the expected value for a lean XeCl mixture. The details of the discharge initiation can be followed more clearly at the faster sweep speeds. Figure 7-2 shows the cathode and screen voltages at 100 ns/cm, Figure 6-12 at 50 ns/cm. Note that at the relatively low charge voltages of 25 kV, the prepulse occurs a few hundred nanoseconds after the peak of the charging pulse. At higher voltages (30 to 32 kV), the prepulse coincides with the peak of the charging curve.

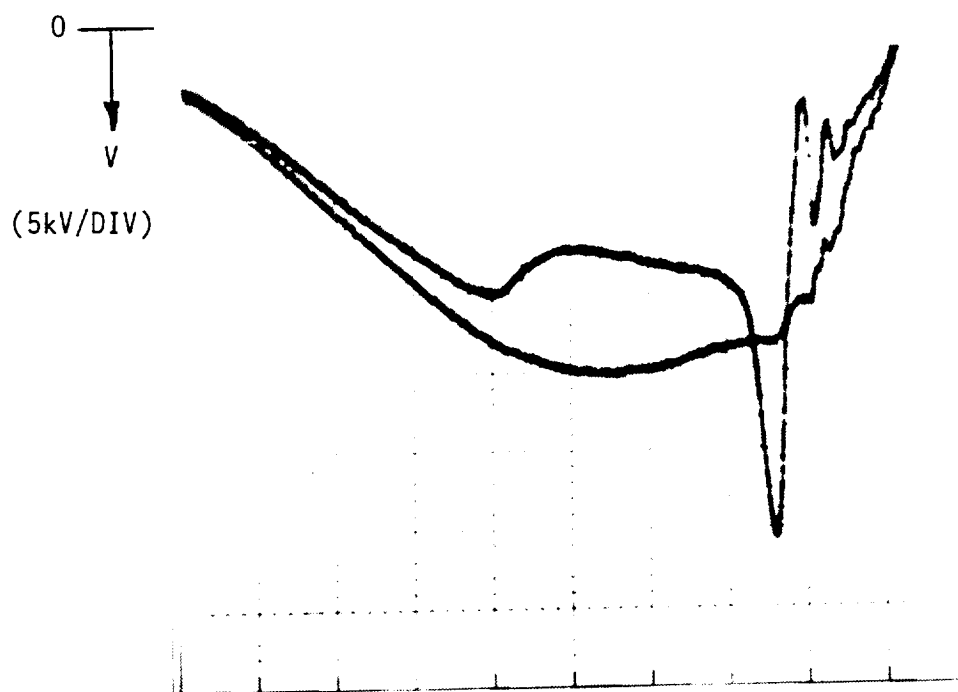


FIGURE 7-1. CATHODE AND SCREEN PULSE  
(200ns/DIV, 22kV CHARGE)

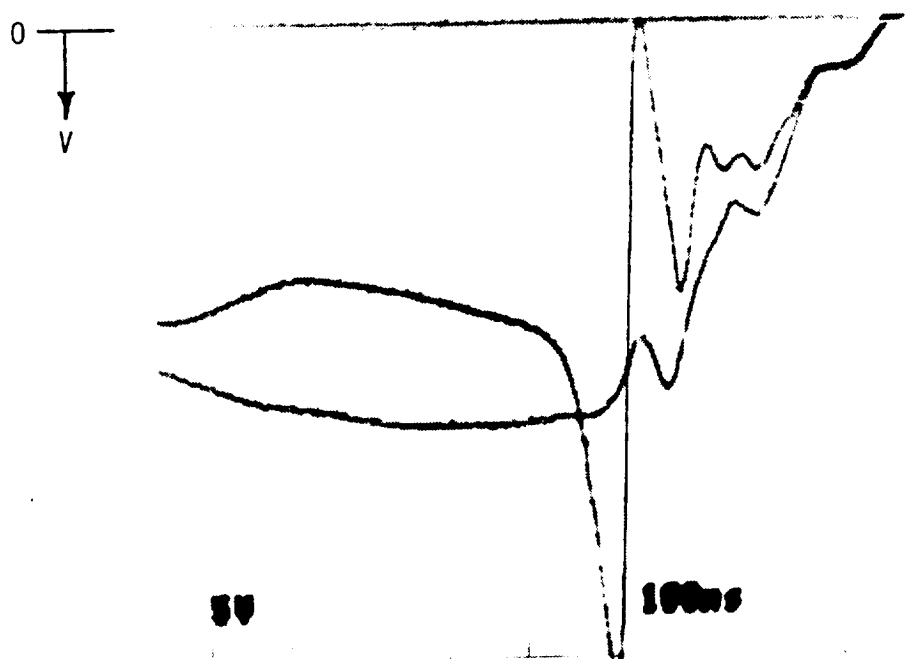


FIGURE 7-2. CATHODE AND SCREEN PULSE  
(100ns/DIV, 25kV CHARGE)



With a new gas fill and clean optical chamber windows, optical laser pulse energies as high as 2.1 J have been measured at a charging voltage of 30 kV. At this voltage, 64 J were stored in the PFL, 8 J in the prepulser and 4 J in the X-ray pulser. The electrical efficiency of the laser works out to be 3.2% based on the energy stored in the PFL, 2.7% based on the overall energy stored in the PFL, the prepulser and the X-ray pulser. When the "predischage losses" are subtracted out, then the lasing efficiency of the main discharge is 4.4%.

The measured optical pulse duration is almost exactly 100 ns FWHM (Figures 7-3 and 7-4). The laser pulse starts approximately 50 ns after both discharge gaps have broken down. Note that there is a difference in the smoothness of the screen voltage during the pump pulse, depending on whether the gas mixture is fresh (Figure 7-3) or whether it has been in the laser for more than a week (Figure 7-4). Apparently, when the gas mixture becomes contaminated with discharge products (remember there is no gas cleanup system installed) after  $10^5$  pulses or so, the discharge becomes less stable and is subject to more severe voltage oscillations. By that time the laser pulse energy has generally deteriorated to approximately 1.2 J.

Only stable resonators with a concave/flat and flat/flat configuration have so far been tested. Typical burn marks on thermally sensitive paper are shown full scale in Figure 7-5. At the two-joule output level, the beam uniformity appears to be considerably better and the intensity profile closer to a top-hat, than at the one-joule level (compare with burn marks in Figure 6-13). Approximately the same energy has been extracted with a 90% transmissive output coupler as with a 70% transmissive output coupler. Optimum output coupling is evidently around 80%. In all these tests, no attempt has yet been made to extract energy from the predischage. The 5 cm diameter reflectors have always been lined up with the main discharge cavity.

Note the regular filamentary structure caused by the sreen in the burn mark of Figure 7-5 (C). This burn mark has been obtained when the laser gas mixture was "old". It appears that a rough electrode surface promotes the formation of cathode streamers, the first indication of discharge instability. This observation makes a good case for smooth solid electrodes.

Without water cooling and with only a slow gas flow, the maximum PRF is 1 Hz. At that repetition rate, the pulse energy stability is excellent (Figure 7-6). Pulse energy variation is approximately  $\pm 1\%$ .

With water cooling and with the tangential blower rotating at 2000 RPM, the maximum PRF appears to be 25 Hz. Beyond this pulse frequency, the pulse energy starts to drop off substantially. At 25 Hz, pulse energy is decreased by approximately 10%. Maximum average power measured with the Scientec power meter has been 30 W (not a fresh gas fill). Chances are excellent that the PRF can be increased to 50 Hz, if the blower is rotated at 3000 RPM with a new 1/3 HP or 1/2 HP motor to replace the 1/4 HP motor driving the magnetic coupling now.

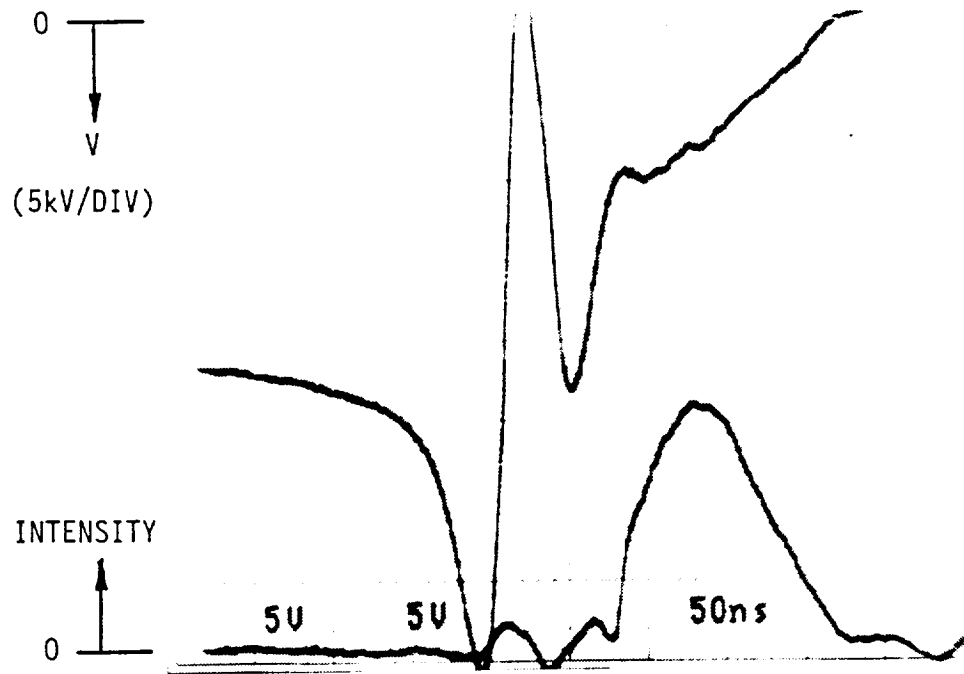


FIGURE 7-3. SCREEN VOLTAGE AND OPTICAL PULSE  
(NEW GAS MIX)

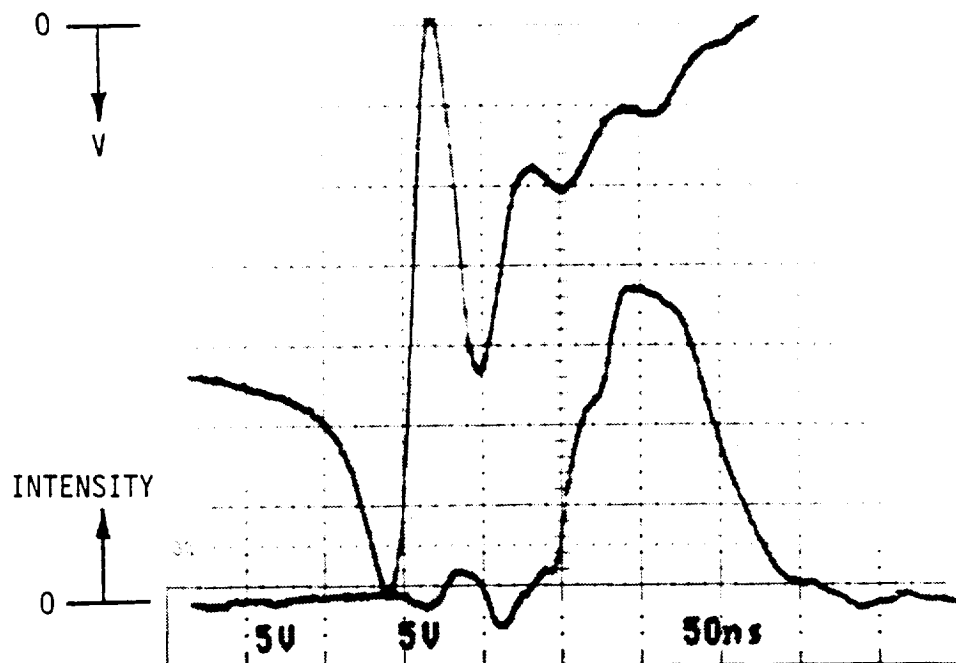
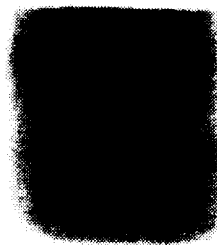
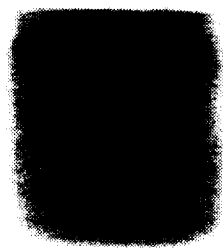
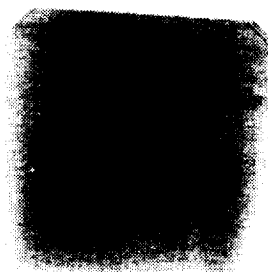
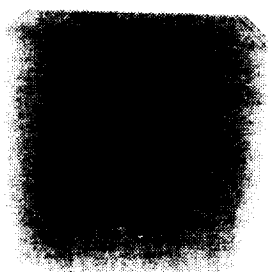


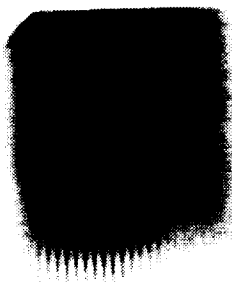
FIGURE 7-4. SCREEN VOLTAGE AND OPTICAL PULSE  
(OLD GAS MIX)



(A) CONCAVE (10m RC) TOTAL  
AND 10% FLAT OUTPUT  
COUPLER (O.C.)

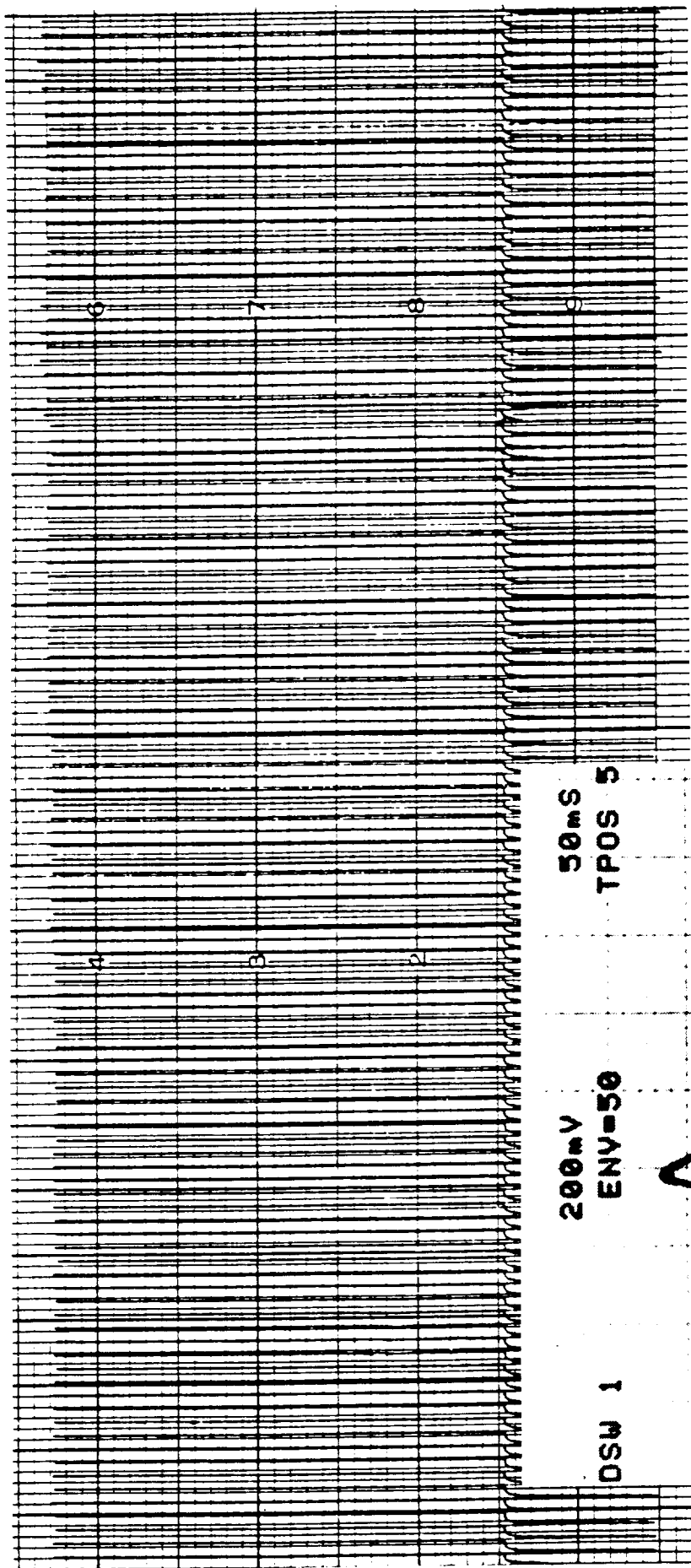


(B) FLAT TOTAL AND  
30% O.C.



(C) FLAT TOTAL AND  
30% O.C.

FIGURE 7-5. BEAM IMPRINTS AT 2 J OUTPUT LEVEL FOR  
DIFFERENT RESONATORS AND ALIGNMENTS



(A) CHART RECORD OF 110 PULSES

(B) OSCILLOSCOPE RECORD OF 50  
SUPERIMPOSED PULSES

FIGURE 7-6. PULSE ENERGY STABILITY AT 1 Hz  
MEASURED WITH PYROELECTRIC  
ENERGY METER (GENTEC)

## 8.0 CONCLUSIONS

The present R&D program has significantly advanced the state-of-the-art of high-pressure pulsed gas lasers. High laser efficiency has been achieved by implementing novel prepulse technology with highly reliable magnetic switches. As part of the program, high-performance Metglas switches with large  $V \cdot t$ -products ( $10^{-2}$  V-s) and with high  $dV/dt$  capabilities ( $10^{12}$  V/s) have been constructed and tested, core reset circuits have been perfected for good repeatability, and an efficient long-life X-ray generator has been developed.

When operated as an RGH laser with XeCl, the laser has produced output pulses of more than 2 joules at 308 nm with laser efficiencies of 3 per cent. Operation of the laser at PRFs of 25 Hz has been demonstrated. These performance figures meet the program goals for XeCl as originally outlined in the proposal. Performance tests for other gases (KrF, XeF and CO<sub>2</sub>) remain to be done.

It is only natural that new insights gained during this program have already made the present configuration obsolete. We feel confident that with our new knowledge we can build a commercial follow-on version of this laser, which is simpler, more powerful, less costly, more reliable and more compact.

## 9.0 PROPOSED FUTURE WORK

During the next 12 months we propose to use the present laser as a test bed for checking out new electrode geometries and new magnetically switched, integrated prepulse generators and PFN configurations. Testing of the laser with KrF and CO<sub>2</sub> is also contemplated.

### 9.1 PROPOSED CHANGES

Based on our previous experience, we propose the following design modifications for an improved version of the present system.

1. The disadvantages associated with the present double-pulsed three-electrode structure appear to outweigh its advantages. Consequently, we propose to employ a two-electrode design with a smooth solid nickel cathode and an anode (X-ray window) covered with a solid 0.125 mm nickel cover. The new high-performance Metglas switches will make it possible to prepulse such a two-electrode gap. The two-electrode geometry will improve the ruggedness of the electrodes, it will result in more effective gas flushing of the discharge gap, and it will result in a more uniform discharge (on account of the elimination of the screen cathode, which provides many starting points for streamers).
2. An integrated prepulse circuit, as shown in Figure 9-1 is proposed, with the magnetic switch located between the cathode and the PFL. In this circuit, the magnetic inductor  $L_2$  acts more as a prepulse generating switch

than as an isolation switch. Consequently, the prepulse does not have to be of opposite polarity to the discharge voltage, as is usually the case with prepulsed two-electrode designs.<sup>10,20</sup> Furthermore, the voltage appearing on the electrodes prior to the prepulse can be kept well below the charging voltage. The 3  $\mu$ H inductor shown in the schematic can preferably also be a saturable inductor.

3. It will be more cost effective to use high-quality TDK ceramic capacitors tested at 60 kV, than to modify bare ceramic discs as was done in the present program. The TDK capacitors have acceptable solid, low-inductance terminals. Alternatively, mica capacitors could be employed.
4. The pulse charging unit should be placed in the same tank as the PFL. The benefits would be more system compactness and faster PFL charging capability.
5. We propose to use a single impeller (possibly nickel plated titanium) for the tangential blower, with only two bearings. The use of silicon nitride bearings should be re-evaluated.
6. The blower baffle and flow guide should be redesigned for more efficient vortex formation at lower RPM.
7. We propose the use of a smaller, shorter and lower-cost magnetic coupling constructed with readily available Nd-Co magnets. A further improvement would be to drive the permanent magnet rotor directly with electric coils located around the outside of the Kynar partition cylinder (i.e. no motor and belt).
8. Redesign the X-ray generator: Locate the HV pulse transformer in an oil filled compartment (or Fluorinert filled) attached to the X-ray tube. This would simplify the anode feedthrough, allow for better X-ray shielding, and eliminate the 100 kV cable between pulser and X-ray tube. Eliminate all plastics from the X-ray tube, use hard metal seals and bakeable ceramics. Eliminate the vacuum pump by use of molecular sieve material in a semi-permanently sealed tube.
9. Make the delay between PFL charging (trigger  $t_1$ ) and X-ray generation (trigger  $t_2$ ) automatic by letting the discharge PFN generate a pulse, that can be amplified into the anode voltage pulse for the e-gun.

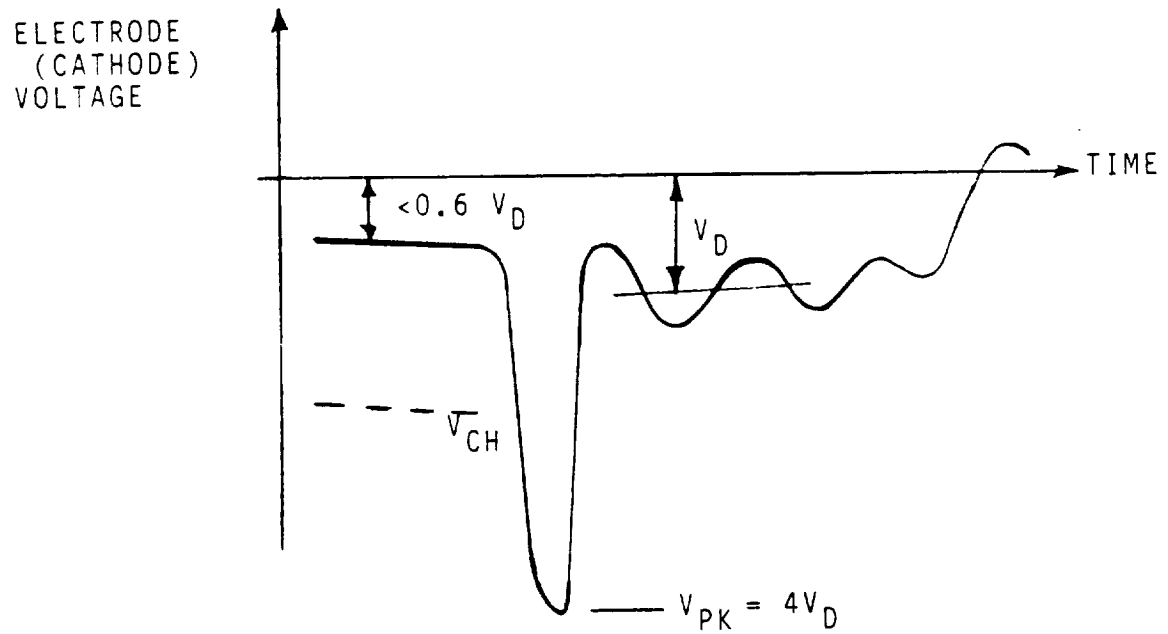
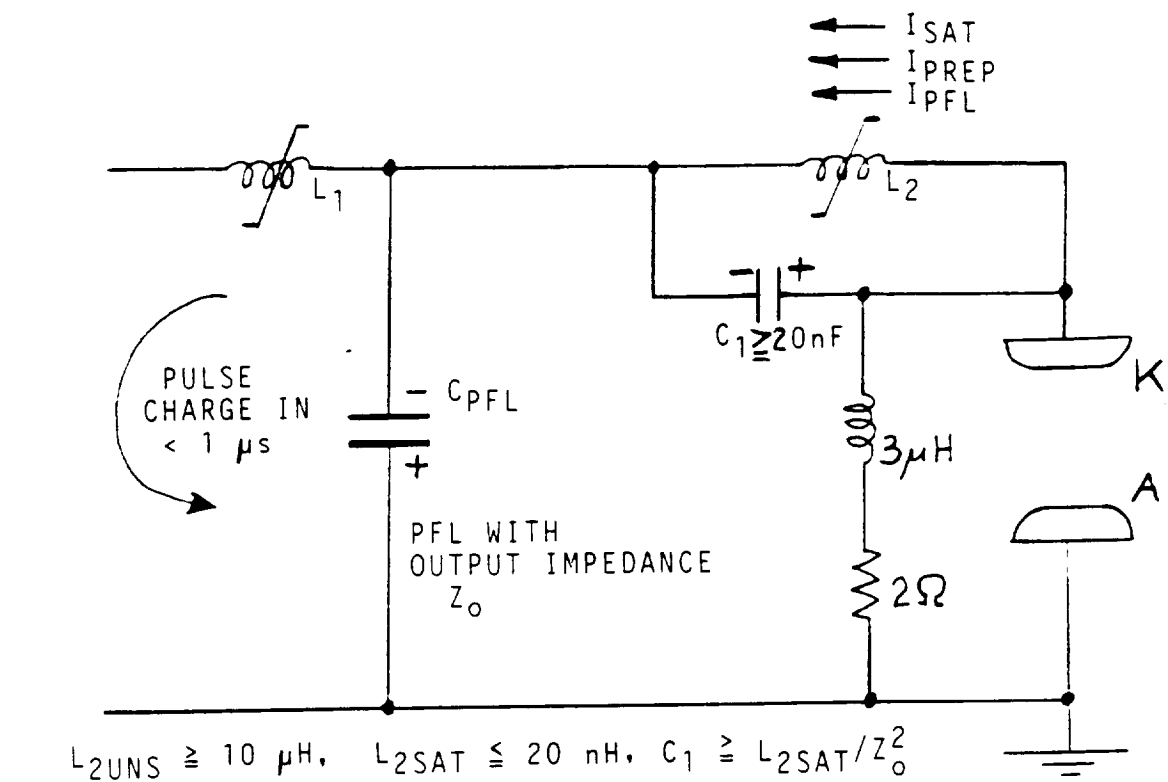


FIGURE 9-1. PROPOSED TWO-ELECTRODE PFN AND PREPULSE CIRCUIT

## 9.2 COMMERCIAL SPIN-OFFS AND APPLICATIONS

The scientific insights gained and the technological advances made under this program will be applied, in the form of new engineering designs, to develop superior laser systems and sub-assemblies for the commercial market, as well as for research and defense. Lasertechnics plans to take the design of the present prototype as the basis for two possible excimer laser products, which would incorporate the modifications outlined in Section 9.1 above. A high-energy RGH laser (KrF and XeCl) with 2 to 4 joules of optical output and modest PRF (25 to 50 Hz) will address commercial markets in the areas of semiconductor processing, product marking and micromachining. It would also find applications in research and defense. A smaller version with 200 mJ output energy, but with a high PRF of 200 Hz, will address the possible markets in UV lithography and in the medical field. A compact, self-contained, long-life X-ray preionizer and a small, powerful magnetic coupling are expected to become marketable products as well.

Business opportunities and applications for RGH excimer lasers are multifold, as can be appreciated from the following partial list of potential applications:

1. REMOTE SENSING
  - A. Remote Sensing of Atmospheric Species (e.g. Ozone and SO<sub>2</sub>)
  - B. Mineral Exploration by Laser-Induced Fluorescence
2. UV PHOTOLITHOGRAPHY
3. SEMICONDUCTOR PROCESSING
  - A. Annealing of Silicon
  - B. Planarization of Metal Films
  - C. Selective Etching of Films
  - D. Selective Photochemical Deposition of Films
4. PRODUCT MARKING AND CODING (Semiconductors and Metals)
5. MICROMACHINING (Metals and Plastics)
6. MEDICAL (Precision Removal of Biological Tissue)
  - A. Laser Angioplasty
  - B. Corneal Machining to Correct Vision
7. PHOTOCHEMISTRY
  - A. Laser Isotope Separation
  - B. Laser Catalysis (Excited State Chemistry)
8. DEFENSE
  - A. Submarine Communications (NAVY)
  - B. Detection of Toxic Agents in Atmosphere (ARMY)
  - C. Distant Target Illumination (SDI)



## 10.0 REFERENCES

1. R. A. Tennant, "Control of Contamination in XeCl Lasers", Laser Focus (Oct. 1981) 65
2. M. A. Akerman, R. A. Tennant, "Discharge Pumped RGH Laser Materials and Gas Clean-Up Studies", paper WB3-1, Topical Meeting on Excimer Lasers, Charleston, SC (Sept. 1979)
3. M. S. Sorem, A. Faulkner, "Catalytic Converter for Closed-Cycle Operation of Isotopic CO<sub>2</sub> TEA Lasers", Rev. Sci. Instrum. 52 (1981) 1193
4. D. S. Stark, A. Crocker, G. J. Steward, "Sealed 100 Hz CO<sub>2</sub> TEA Laser Using High CO<sub>2</sub> Concentrations and Ambient Temperature Catalysts", J. Phys. E: Sci. Instrum. 16 (1983)
5. R. S. Rogowski, I. M. Miller, G. M. Wood et al., "Evaluation of Catalyst for Closed-Cycle Operation of High Energy Pulsed Lasers", SPIE Proc. 415 (1983) 112
6. D. E. Rothe, Work performed in the development of first commercial CO<sub>2</sub> and HF/DF TE-lasers as staff scientist with Lumonics Research, Ltd., Ottawa, Canada (1971-76)
7. J. I. Levatter, S. C. Lin, "Necessary Conditions for the Homogeneous Formation of Pulsed Avalanche Discharges at High Pressures", J. Appl. Phys. 51 (1980) 210
8. D. C. Hogan, A. J. Kearsley, C. E. Webb, R. Bruzzese, "Pulse Length Limitations in Self-Sustained Discharge XeCl Lasers", AIP Conf. Proc. (Ed. H. C. Wolfe) No. 100, Opt. Sci. and Engin. 3, Excimer Lasers 1983, Am. Inst. Phys. (NY 1983) 1
9. R. S. Taylor, "Preionization and Discharge Stability Study of Long Optical Pulse Duration UV-Preionized XeCl Lasers", Appl. Phys. B (Springer) 41 (1986) 1
10. D. E. Rothe et al., "Efficiency Optimization of a Discharge Excited XeCl Laser", Final Tech. Report, ONR Contract N00014-82C-0087, Office of Naval Research, Arlington, VA (Dec. 1982)
11. W. H. Long, M. J. Plummer, E. A. Stappaerts, "Efficient Discharge Pumping of an XeCl Laser Using a High-Voltage Prepulse", Appl. Phys. Lett. 43 (1983) 735
12. W. H. Long, M. J. Plummer, "Tandem Discharge Pumped Excimer Lasers", paper Th-ZZ8, Conf. on Lasers and Electro-Optics (CLEO), Baltimore, MD (May 1985)
13. L. J. Denes, J. J. Lowke, "V-I Characteristics of Pulsed Laser Discharges", Appl. Phys. Lett. 23 (1973) 130
14. D. E. Rothe, C. Wallace, T. Petach, "Efficiency Optimization for Discharge-Excited High-Energy Excimer Laser", AIP Conf. Proc. No. 100, Opt. Sci. and Engin. 3, Excimer Lasers 1983, Am. Inst. Phys. (NY 1983) 33
15. B. Lacour, C. Vannier, "X-Ray Photoswitching of a 1 J Excimer Laser", paper Th-Q2, Conf. on Lasers and Electro-Optics (CLEO), Baltimore, MD (May 1985)
16. T. Shimada, M. Obara, A. Noguchi, "An All Solid-State Magnetic Switching Exciter for Pumping Excimer Lasers", Rev. Sci. Instrum. (Nov. 1985)

17. NASA, Earth Observing System, Vol. I Tech. Memorandum 86129, NASA/Goddard Space Flight Center, Greenbelt, MD (Aug. 1984)
18. V. S. Abreu, "Wind Measurements from an Orbital Platform Using a LIDAR System with Incoherent Detection", Appl. Opt. 18 (1979) 2992
19. G. Megie, R. T. Menzies, "Complementarity of UV and IR Differential Absorption LIDAR for Global Measurement of Atmospheric Species", Appl. Opt. 19 (1980) 1173
20. J. B. Laudenslager, "Excimer Lasers Adapt to Angioplasty", Laser Focus/Electro-Optics (May 1988) 57
21. D. E. Rothe, "Widely Tunable Gas Laser for Remote Sensing of Stratospheric Constituents", Final Tech. Report, NASA/SBIR Contract No. NAS7-935 Phase I, Rothe Technical Research Rep. No.1, Carlsbad, CA (June 1985)
22. T. Y. Chang, "Improved Uniform Field Electrode Profiles for TEA Lasers", Rev. Sci. Instrum. 44 (1973) 405
23. C. Birnbach, J. Tanner, "X-Ray Source Employing Cold Cathode Gas Discharge Tube with Collimated Beam", U.S. Patent No. 4,670,894 (2 June 1987)
24. S. J. Scott, "Experimental Investigations on an X-Ray Preionizer Test Bed", J. Appl. Phys. 64 (1988) 537
25. J. I. Levatter, R. L. Sandstrom, J. H. Morris, "The Corona Plasma Cathode: A New Long-Life E-Beam Cathode for X-Ray Preionization", Proc. IEEE, 4th Pulsed Power Conf. 1983, ed. T. K. Martin, M. F. Rose (N.Y. 1983)
26. C. H. Smith, L. Barberi, "Dynamic Magnetization of Metallic Glasses", Proc. 5th IEEE International Pulsed Power Conf., Crystal City, VA (June 10 -12, 1985)